A Geological and Geophysical Investigation into the Evolution and Potential Exploitation of a Geothermal Resource at the Dixie Valley Training Range, Naval Air Station Fallon.

BY

Steve Allen Alm Jr.

Submitted to the graduate degree program in Geology and the Graduate Faculty of the University of Kansas in partial fulfillment of the requirements for the degree of Master of Arts

Advisory Committee

_____

J. Douglas Walker, Chair

_____

Michael H. Taylor

_____

George Tsoflias

Date Defended: May 12, 2016

The Thesis Committee for Steve Allen Alm Jr

certifies that this is the approved version of the following thesis:

A Geological and Geophysical Investigation into the Evolution and Potential Exploitation of a Geothermal Resource at the Dixie Valley Training Range, Naval Air Station Fallon.

_____

J. Douglas Walker, Chair

Date Approved: May 12, 2016

Abstract

This study examines the geological and geophysical controls on geothermal fluid migration in two discrete geothermal systems in the highly-extended region of the central Great Basin. Active right-lateral oblique slip of the Fairview Peak-Louderback Mountain fault zone is transferred to similarly active normal dip-slip movement in the Dixie Valley-La Plata-Sand Springs fault zone across a buried accommodation structure in southern Dixie Valley and northern Fairview Valley, central Nevada. This accommodation zone coincides with the potentially exploitable geothermal systems known as Pirouette Mountain and Elevenmile Canyon. Similar to many other Great Basin geothermal systems the translation of geothermal fluids near to the surface is related to a structural configuration that promotes fluid flow through fracture permeability. An interpretation of this relationship as it applies to these geothermal systems was completed through a combination of detailed geologic mapping, Ar-geochronology, interpretation of geophysical data (aeromagnetics, gravity, and 2D-seismic), and structural analysis. The geophysical data was critical in understanding the geometry of structures not expressed at the surface. The structural analysis included an examination of available fault kinematic data that was resolved into paleostress orientations applied to an analysis of slip and dilation tendency for all mapped structures in the study area, including 3D planes generated from the 2D-sesimic interpretation. The results indicate that the Pirouette Mountain geothermal system is associated with a concealed oblique anticlinal accommodation zone that is bound by structures that are poorly oriented for slip and dilation and act as fluid barrier to southward fluid migration in basement stratigraphy. Fault intersections with the

steeply dipping, dilation prone, northern continuation of the Louderback Mountains fault appear to be critical to geothermal fluid migration in the system. The results also characterize the Elevenmile Canyon geothermal system as a discrete upwelling of geothermal fluids along faults well oriented for slip and dilation that terminate into the Elevenmile Canyon caldera margin within a broader structural setting that can be characterized as a major stepover from the Sand Springs Range frontal fault system to the Stillwater Range frontal fault system. The results of this study are meant to inspire renewed interest in further exploration and delineation of geothermal systems in Southern Dixie Valley in addition to generating new discussion on the application of these methods and others in the best practice of identifying, exploring, and exploiting additional geothermal systems in the Great Basin and beyond

Acknowledgements

This work was financially supported by the US Navy Geothermal Program Office located at the Naval Air Weapons Station in China Lake, CA, a Graduate Research Fellowship from Chevron, and a Teaching assistantship from the University of Kansas. A special thanks to Dr. J. Douglas Walker, Dr. George Tsoflias, and Dr. Michael Taylor for sponsoring this work and always being available for discussion and inspiration. Thanks to Dr. Joseph Andrew for letting me sit next to you and ask questions to no end. Thanks to Satish Pullammanappallil at Optim llc for the acquisition and processing of the 2D-seismic data. Thanks to Andrew Tiedeman for helping me collect rock samples in the hot Nevada sun. Thanks to Jerry Whistler for providing GIS support. Thanks to Alan Morris at the Southwest Research Institute for developing and supporting 3D-Stress. And so much appreciation to all the people who contributed their expertise along the way: Dr. Andrew Sabin, Dr. Ross Black, Dr. Chris Henry, Dr. John Bell, Dr. John Caskey, Nick Hinz, Josh Feldman, Michael Lazaro, Kelly Blake, Jeff Shoffner, and Dr. Drew Siler. Thanks to all my friends and family for their endearing support and constant inspiration.

Dedication

This work is dedicated to my family, without whom this project would not have been possible. Monica, my wife and partner in life, who has stood with me through this and all other challenges, who never questions our ability to achieve great things, and to whom I am forever grateful. To my daughter Victoria and my son Axel I hope that someday you find the great happiness I have found in you, you mean the world to me.

Contents

LIST OF FIGURES

LIST OF TABLES

LIST OF PLATES

1. Introduction

1.1 Background

The physical and thermal evolution of plate tectonic boundaries is largely controlled by mantle convection and dynamic instabilities between the asthenosphere and lithosphere. These boundaries define the common setting of major plate formation and motion (i.e. active volcanism and tectonism) and regulation of solid earth heat loss that generates localized storage of extractable thermal energy, referred to herein as geothermal systems. Tectonic settings commonly associated with geothermal systems include magmatic arcs above subduction zones, divergent and transform margins in an intracontinental or oceanic setting, and intraplate hot spots. Commonly associated with major fault systems and active/young volcanism, these settings provide the elevated heat flow and fluid pathways needed for typical convective heat transfer by percolation of meteoric waters to depths of elevated geothermal gradient.

Since the inception of the Mendocino Triple Junction (MTJ) at ~30 Ma (Atwater and Stock, 1998) tectonic conditions at the western North America Plate margin have generated favorable conditions for an abundance of geothermal systems in the western US. The US geothermal power industry's power production is the highest in the world and grew to 3,442 megawatts (MW) (e.g. Geysers, Salton Sea, Coso) in 2013 and had a 50% growth outlook for the following year (Matek, 2013). However, growth is anticipated to be largely restricted to expansion and

retrofit of existing fields. Not included in those numbers are the current direct use projects that rely on the high efficiency of direct heat transfer that include district heating, aquaculture, and greenhouse food production (Center, 2005). These projects represent a largely unrecognized and profitable growth market in the renewable energy sector. The negligible emission of greenhouse gas, reliability as an uninterrupted source of renewable base load energy, potential role in CO_2 sequestration, and wide spread direct use application make geothermal resources a critical component in nurturing U.S. economic prosperity while reducing carbon emissions.

With over 400 inventoried geothermal systems in the Great Basin of the western USA and with only 27 producing electricity (Figure 1.1), there is a vast resource of untapped energy potential in the region. That potential does not include undiscovered geothermal systems lacking typical surface manifestations, referred to as "blind" geothermal systems (Sass et al., 1971). Blind systems represent ~35% of known Great Basin geothermal systems (Coolbaugh et al., 2007). Undeveloped geothermal systems in the Great Basin have the potential for distributed generation on a smaller scale (10's of megawatts) with high capacity. Smaller systems are inherently harder to develop and have longer pay back periods. For this reason, it is important to have low cost exploration, low risk drilling, and accurate estimation of energy production to reach full production more rapidly.

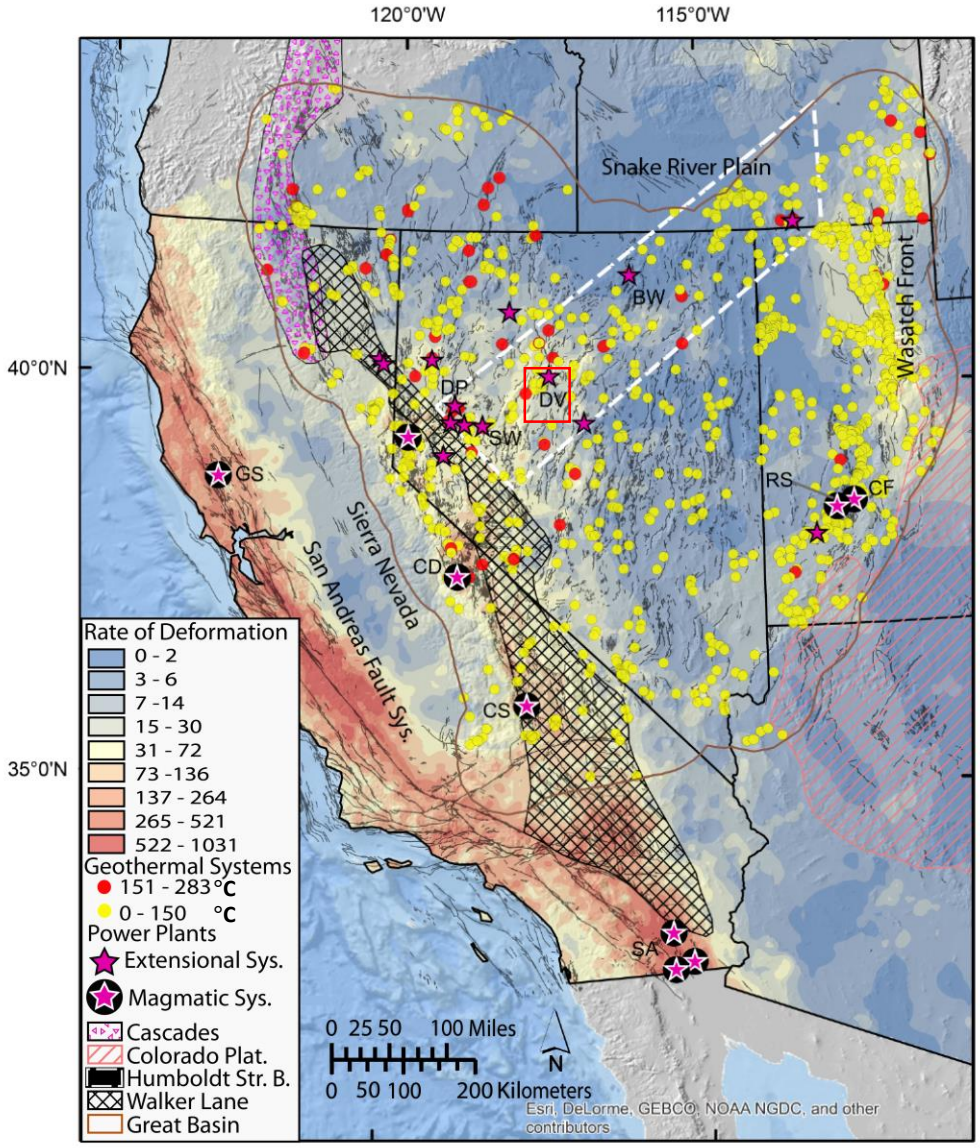

Figure 1.1. Rate of deformation mapped from the second invariant of strain rate tensor (10-9/yr), from (Kreemer, 2014; Kreemer et al., 2012) with geothermal systems, characterized by temperature, overlain (modified from (Faulds et al., 2012b). The study area, in Southern Dixie Valley, lies in a region of locally moderate strain rates that coincide with an abundance of extensional domain geothermal activity. The study area is outlined in red. Producing geothermal systems of note include Geysers (GS), Salton Trough (SA), Coso (CS), Casa Diablo (CD), Desert Peak (DP), Stillwater (SW), Dixie Valley (DV), Beowawe (BW), Roosevelt (RS), and Cove Fort (CF).

When compared to other natural resource industries (e.g. oil & gas, minerals) limitations in geothermal resource identification and assessment strategies exist in terms of categorization, advanced exploration, and financial modeling. The acceleration of the prospect to production field timeline is critical for decreasing periods of negative cash flow and for the expansion of the geothermal industry into development of smaller, distributed systems. First order problems in realizing this vision include the lack of a global standard of descriptions of geothermal resources and a prescription for advanced exploration techniques during early resource evaluation. Moecke and Beardsmore (2014) propose a geothermal play type terminology to improve reporting outcomes and help streamline the decision making process. This study uses the proposed terminology and employs recent exploration strategy advances to develop initial models for two adjacent Great Basin blind geothermal plays in west central Nevada.

Geothermal plays begin as a model that is a three-dimensional rationalization of available geological and geophysical data that dictates the initial boundaries and physical descriptions of the geothermal system controls. Moecke and Beardsmore (2014) adapt the following controls from general hydrocarbon play concepts described by Allan and Allan (2005): a) The reservoir unit(s) providing adequate permeability and storage capacity for commercial thermal fluids. b) Heat charge system defined by source and mode of transport. c) The regional topseal or caprock, typically a trap forming unit or surface. d) Temporal association of the previous three aspects. e) The play fairway, a geographic area of high probability resource access as defined by initial conceptual models (Figure 1.2).

The initial categorization of plays relies on the nature of the heat charge system. End members are convection and conduction dominated transport systems. Convection dominated systems are divided into “Magmatic,” “Plutonic,” and “Fault-controlled in Extensional Domain” play types; conduction dominated systems are divided into “Intracratonic Basin plays,” “Orogenic Belts with Adjacent Foreland Basins,” and “Crystalline rock/ Basement” play types. Each play type is characterized by a combination of geologic controls and in some cases as a combination of two types (e.g. magmatic and fault-controlled in extension domain).

1.1.1 **The Basin and Range Province**

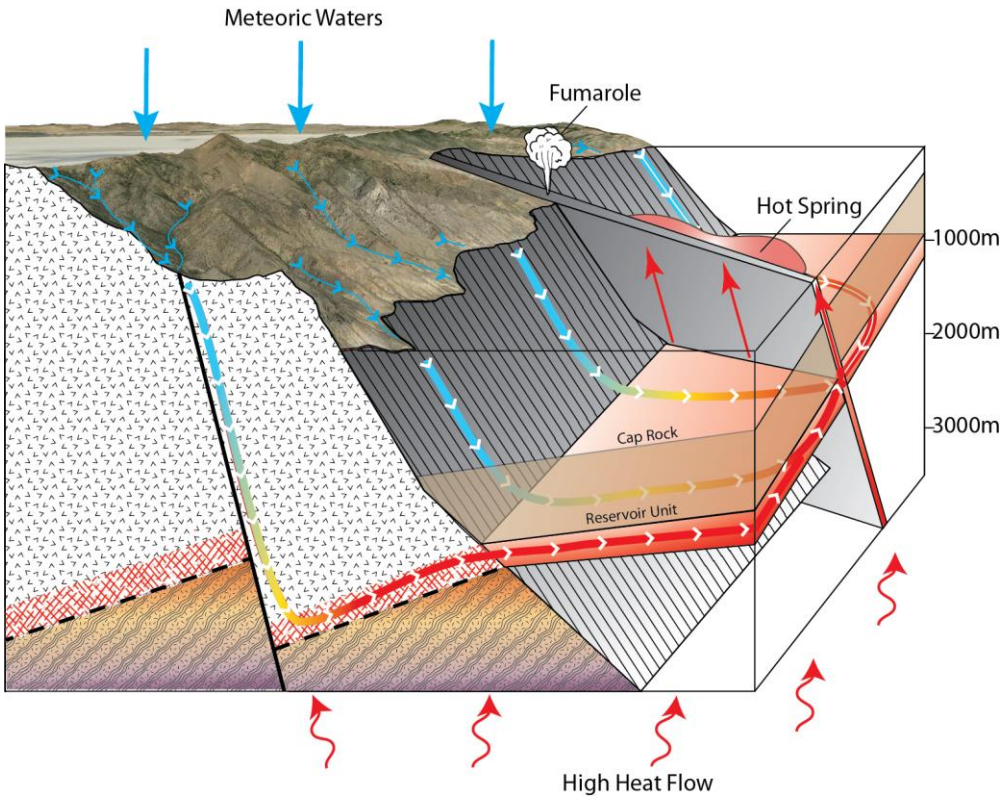

Figure 1.2. Annotated model of a basic, conceptual geothermal system highlighting a permeable reservoir unit, heat charge system, surface expression, and meteoric recharge similar to Dixie Valley.

Recent volcanism is restricted to the outer margins of the region, so the majority of Great Basin geothermal systems are convection-dominated extensional domain plays. Although a minority of the overall systems, convection dominated magmatic plays in extensional domains (e.g. Coso, Steamboat, Roosevelt) are also present and are typically high enthalpy systems, in excess of 160^{o}C (Faulds et al., 2012b), generating considerable amounts of electricity.

Research has shown strong correlations between Great Basin geothermal activity, high rates of geodetically measured transtensional crustal strain (Faulds et al., 2012b; Hammond and Thatcher, 2004; Kreemer et al., 2009; Kreemer et al., 2012), prominent heat flow (70-90 mW/m^2) (Blackwell, 1983; Blackwell and Richards, 2004; Sass et al., 1994), and active faulting (Bell and Ramelli, 2007; Faulds and Henry, 2008; Walker et al., 2005). More specifically and of a more regional importance is the well documented relationship between active geothermal systems and the orientation of active faults, principally those orthogonal to the least principal stress (Barton et al., 1997; Faulds et al., 2004) and zones of intermeshing and overlapping discontinuous faults segments (Faulds et al., 2011). Studies on geothermal systems worldwide have also found that related surface outflow (i.e. hot springs, mud pots, fumaroles) focus in areas of fault termination and interactions (Curewitz and Karson, 1997). Micklethwaite and Cox (2004) found that paleo-rupture arrest sites that correspond with aftershock locations generate enhanced permeability by concentration of small displacement structures and minimal development of low permeability fault gouge.

1.1.2 **Structural Configurations**

Other recent studies focused on developing advanced exploration techniques for initial site characterization have catalogued Great Basin geothermal systems and differentiated them by examination of the common structural elements. Faulds et al. (2011) state that structural settings that have enhanced potential of hosting geothermal resources are defined by “a) discrete steps in normal fault zones, b) intersections between normal faults and transversely oriented oblique-slip faults, c) overlapping oppositely dipping normal fault zones, d) terminations of major normal faults, or e) transtensional pull-apart zones” (Figure 1.3). More recently, recognizing that geothermal hybrid systems or systems characterized by a combination of two or more previously stated structural settings represent a majority of operating geothermal fields in the region. The previously stated correlation suggests that enhanced structural complexity favors the presence of readily exploitable geothermal systems.

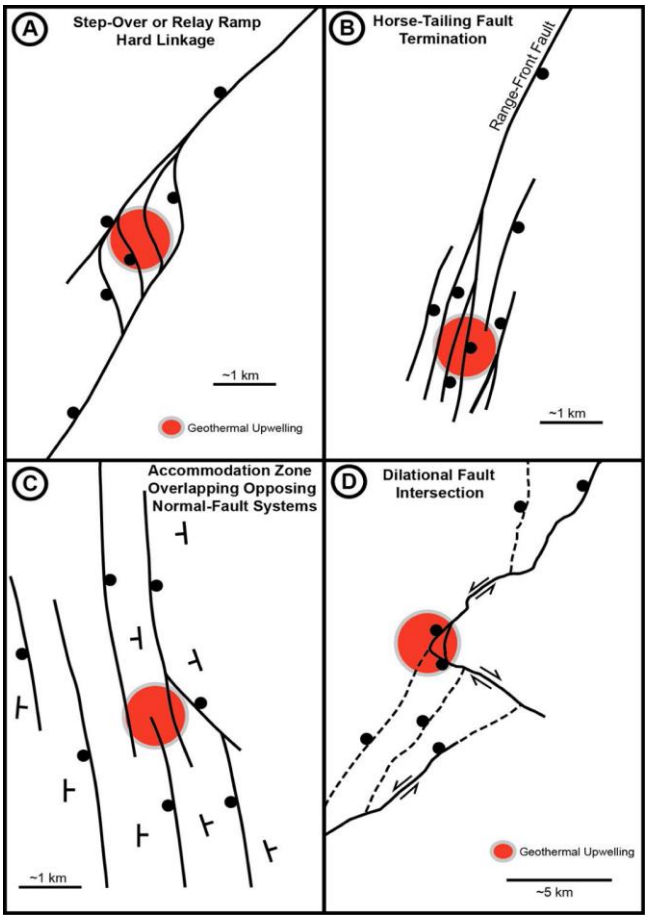

Figure 1.3. From Faulds et al. (2011). Four illustrations of favorable structural settings for geothermal systems. Strongest upwelling geothermal fluids are shaded in red. A. Step-over or relay ramp between two overlapping normal fault segments with multiple minor faults providing hard linkage between two major faults. B. Terminations of major normal faults, whereby faults break up into multiple splays or horsetail. C. Overlapping, oppositely dipping normal fault systems (accommodation zones) that generate multiple fault intersections in the subsurface. Strike and dip symbols indicate tilt directions of fault blocks. D. Fault intersection between oblique-slip normal faults.

1.1.3 **Other Characteristics**

Further advances in exploration include geochemical research on isotopic relationships in country rock, water samples, and soil gas flux and have been shown to help focus regional-scale

exploration, especially for blind geothermal systems. These studies can also provide reservoir temperature estimations, evidence for migration patterns, and help identify structural barriers within geothermal systems (Bergfeld et al., 2001; Edmiston, 1985; Fournier, 1977; Gorynski et al., 2014; Shevenell and Coolbaugh, 2011). Geophysical exploration tools have the ability to express the contrast of physical properties (e.g. temperature, density, magnetic susceptibility, resistivity, velocity) for the interpretation of structures, composition of buried rocks, high-stand hydrothermal mineral deposition, and electrical properties associated with mass transport of fluid in the subsurface.

Any prescribed exploration approach for a given play type will need to be proven as the most effective combination of exploration tools capable of revealing subsurface conditions for the selection of drilling targets. For the Great Basin in particular, an emphasis should be placed on the relationship between the occurrence of geothermal systems, neotectonics, critically stressed structures, dilation and slip tendency, and faults that step, overlap, terminate, or intersect. Thereby, collecting data that relates to structural architecture, fluid temperature and migration of the geothermal system is important. These data are used to develop an initial 3D model that constrains critical geologic controls and effectively reduces the spatial target volume with what is deemed to be characteristic temperature and permeability of an exploitable geothermal system.

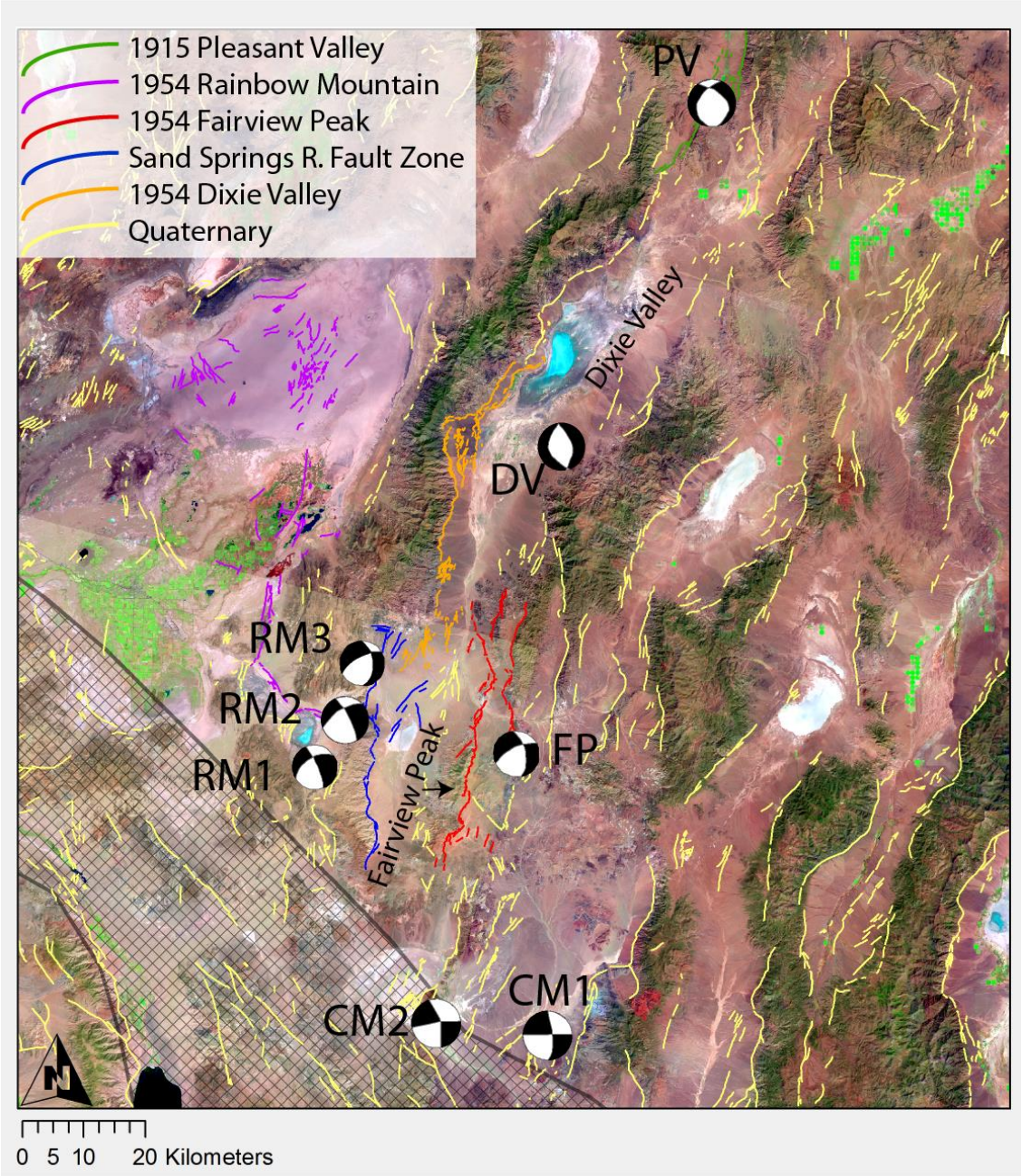

Figure 1.4. Distribution of Quaternary faults and focal mechanisms for historic earthquakes in the Central Nevada Seismic Belt (CNSB), modified from Bell et al. (2004). The Hypocenter for the Fairview Peak event was just east of Fairview Peak and the derived focal mechanism defines dextral-oblique motion along a nodal plane oriented 347˚. The Dixie Valley event hypocenter is located in central Dixie Valley and the focal mechanism defines almost pure normal slip along a nodal plane oriented 350˚. Cedar Mountain events (CM1, CM2), Dixie Valley event (DV), Fairview Peak event (FP), Pleasant Valley event (PV), Rainbow Mountain events (RM1, RM2, RM3)

1.1.4 **Pirouette Mountain and Elevenmile Canyon Geothermal Systems**

The Pirouette Mountain (PM) and Elevenmile Canyon (EMC) geothermal systems are blind, fault-controlled extensional plays located in discreet sub regions of the major accommodation zone between Fairview Valley and Dixie Valley. This region represents the locust of ~300 km of intermeshing and overlapping historical and Quaternary surface faulting known as the central Nevada seismic belt (CNSB) (Bell et al., 2004) (Figure 1.4). These geothermal systems were initially discovered through a wildcat drilling campaign by the Hunt Energy Corporation in the late 1970's. Hunt Energy drilled three deep wells before bankruptcy forced them to abandon the project. In 1999 the U.S. Navy acquired portions of these lands as part of a land withdrawal for the Naval Air Station Fallon (NASF) electronic warfare training range and exploration was subsequently resumed by the Navy Geothermal Program Office (GPO) in 2005 (Figure 1.5).

Located 60 km north of the study area is the 62 MW Dixie Valley dual-flash geothermal field (DVGF), which is one of the largest and hottest (>285^{o}C) geothermal systems in the state of Nevada. Since 1988 the 5.5 km long field has been extracting thermal energy from 2500 to 3500 m below the surface (Blackwell et al., 2007) near Stillwater Gap. The Stillwater Gap is a 10 km section of the major range bounding fault that separates Dixie Valley from the northern Stillwater Range. The Stillwater Gap is also interpreted as a major step-over or relay ramp in the Stillwater frontal fault system and as a zone of fault intersection where the northeast trending frontal fault cross-cuts older, northerly oriented structures to form a compound or hybrid structural setting, considered to be most favorable. Other geothermal systems located along

this major normal fault and potentially sourced from the same deep convection system includes; South Hills and Hyder Hot Springs to the North, and Dixie Comstock Mine, Dixie Meadows, EMC and PM to the south (Figure 1.5).

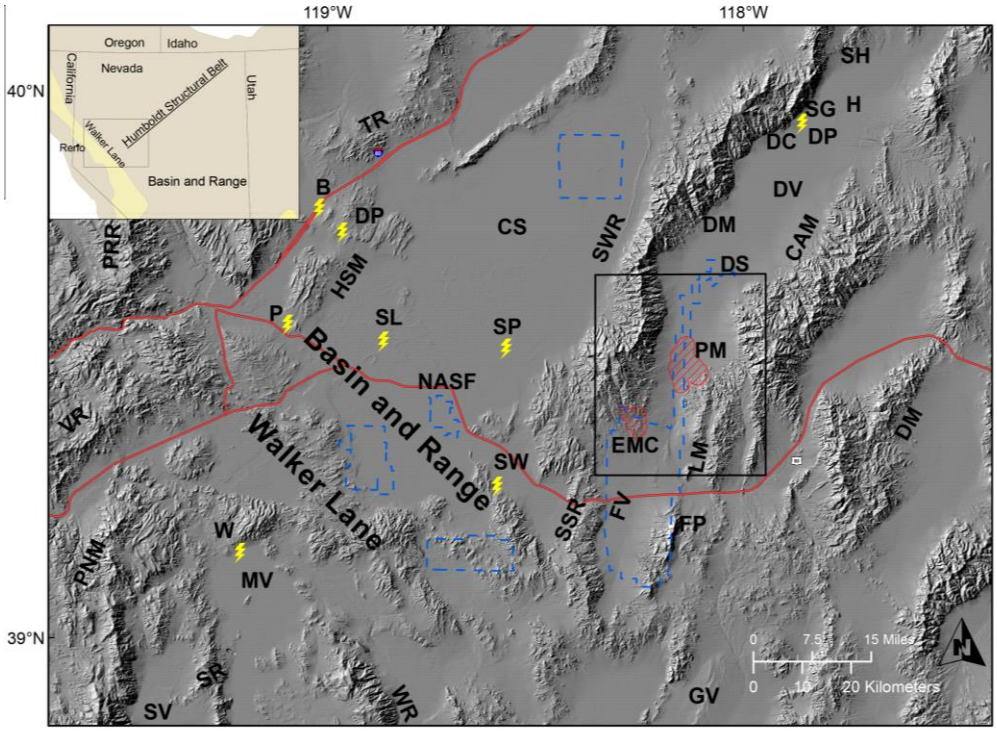

Figure 1.5. USGS 30m digital elevation model (DEM) derived hillshade map of prominent physiographic features that include transverse ranges of the NW trending Walker Lane and characteristic NE striking ranges of the Basin and Range. Notable basins/valleys; DV – Dixie Valley; FV – Fairview Valley; GV – Gabbs Valley; SV – Smith Valley; MV – Mason Valley; CS – Carson Sink; PL – Pyramid Lake; Notable ranges; PRR – Pah Rah Range; VR – Virginia Range; PNM – Pine Nut Mountains; SR – Singaste Range; WR – Wassuk Range; SSR – Sand Springs Range; FP – Fairview Peak; LM – Louderback Mountains; DM – Desatoya Mountains; CAM – Clan Alpine Mountains; SWR – Stillwater Range; HSM – Hot Spring Mountains; TR – Trinity Range; Notable Geothermal Systems; SH – Sou Hills; HS – Hyder Hot Springs; DC – Dixie Comstock Mine; Dixie Settlement (DS); Stillwater Seismic Gap (SG); PM – Pirouette Mountain; EC – Elevenmile Canyon; Producing Geothermal Fields; B – Brady's; DP – Desert Peak; P – Patua; SL - Soda Lake; SP – Stillwater; SW – Salt Wells; W – Wabuska; DP – Dixie Valley; Naval Air Station Fallon (NASF) and outlying training ranges outlined in dashed blue line. Study area outlined in black line. Geothermal systems of interest (EMC, PM) red hachured areas

The PM geothermal system is located in an accommodation/displacement transfer zone where dextral oblique slip from the northern termination of the Louderback Mountains fault is transferred to normal slip along the southern termination of the Dixie Valley fault and other structures. As normal faults terminate they commonly splay into multiple strands and form what is known as a horsetail pattern. Terminations are also characterized by greater fault density and less accumulated slip (i.e. less fault gouge), which can result in areas of enhanced permeability. Fault tip tensional stress in extensional environments can also enhance fault dilation by causing minor perturbations of the horizontal stress field, thus generating a larger aperture fracture and facilitating enhanced fluid flow (Curewitz and Karson, 1997). Surface ruptures of the historic 1954 Fairview Peak event also terminate several kilometers to the south of the PM geothermal systems. These west-dipping fault traces are in close proximity to the east-dipping Dixie Valley fault, and the concealed continuations of these traces likely intersect and terminate at depth and further enhance permeability. These structural characteristics are all coincident with a prominent thermal signature that is likely related to the combination of multiple structural settings common to geothermal systems of the Great Basin (Faulds et al., 2013).

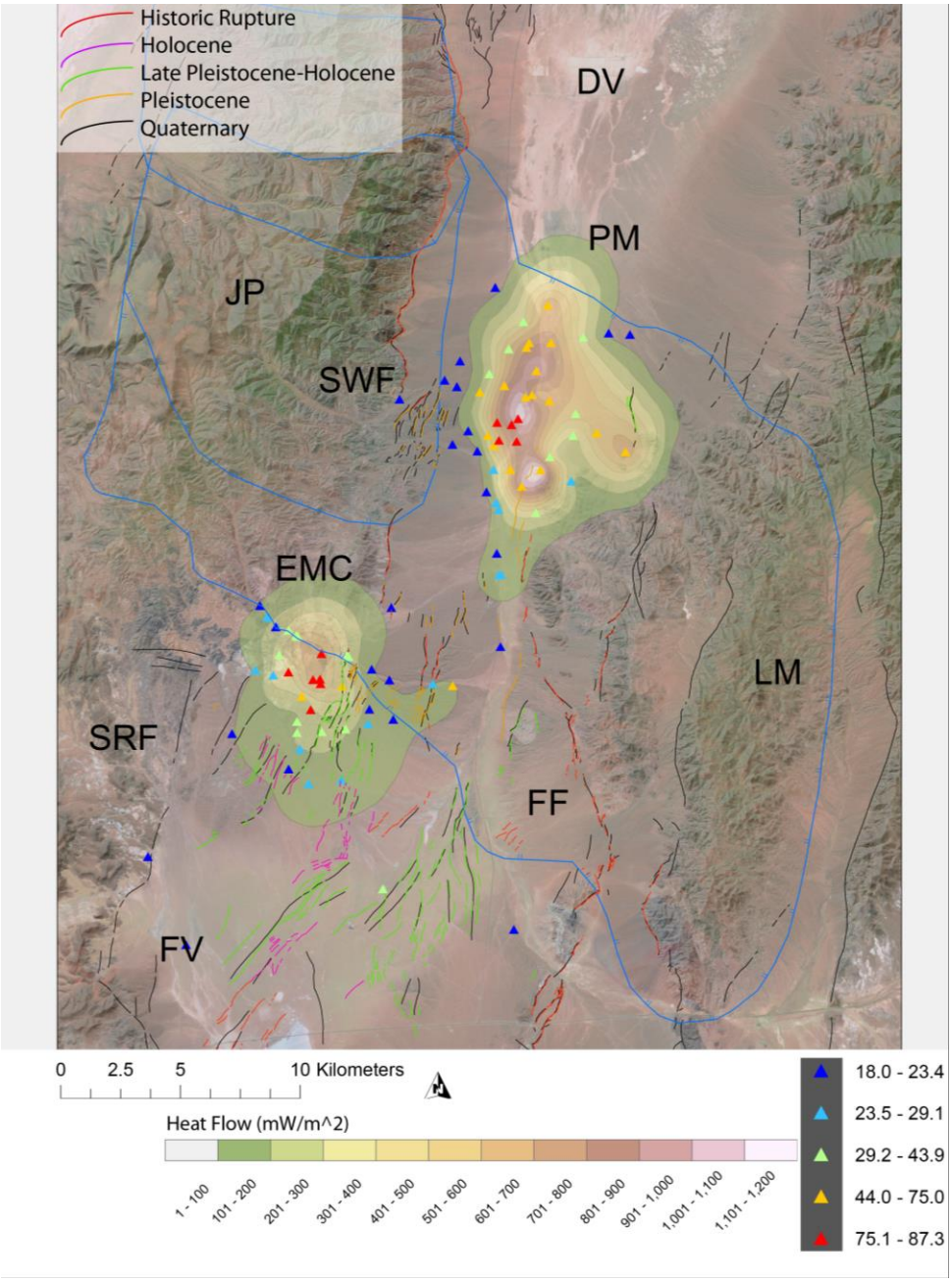

Figure 1.6. LANDSAT8 data overlain on a digital elevation model of the study area , as outlined in Figure 1.5, including Job Peak (JP), Fairview Valley (FV), Louderback Mountains (LM), Dixie Valley (DV), Sand Springs Range frontal fault (SRF), Stillwater Range frontal fault (SWF), and the Fairview Peak fault (FF). Pirouette Mountain (PM) and Elevenmile Canyon (EMC) Geothermal systems as defined by associated heat flow measurements, contoured where background temperatures are generally exceeded, as modeled by Williams et al. (2012). Stillwater Caldera complex boundaries in blue with hachures indicating caldera interior (Henry and John, 2013). Shallow (~187 m) temperature gradient wells are triangles shaded by temperature.

Thermal modeling based on 39 wells drilled by the Hunt Corporation were used to characterizes the geothermal system as a dissipating thermal aquifer primarily sourced by geothermal fluids upwelling along a horst structure that heats meteoric fluids at the contact between Oligocene volcanic basement and valley fill in the central reach of the accommodation zone (Williams, 2012). Mixing appears to produces strong lateral basinward flow, evidenced by the complex asymmetric heat flow pattern (Figure 1.6). Strong mixing also appears to be complicating the estimation of reservoir temperatures through geochemical analysis. Analyses by both Hunt and the GPO suggest that reservoir temperatures range 90-120 C.

The EMC geothermal system is located in a major 5.5 km step-over between the range-front fault systems of the Sand Springs Range, to the west, and the Stillwater Range to the east (Figure 1.6). The area is commonly referred to as La Plata Canyon or Elevenmile Canyon and contains numerous faults ranging in age from Neogene to Quaternary and includes surface ruptures from the 1954 events. The step-over seems to accommodate strain transfer around the southern Stillwater Range as fault orientations deflect to the northeast or terminate into the west-northwest trending Oligocene caldera margin in Elevenmile Canyon (Figure 1.6). The step-over and the north-northeast trending faults that intersect the caldera margin ring fractures are also considered a hybrid of favorable structural settings and are a potential source for increased fracture density, dilation, and permeability.

Williams (2012) also examined the 34 wells drilled by the Hunt Corporation in the Elevenmile-La Plata Canyon area and established that there is marginal heat loss associated with the EMC geothermal system and that it is not well constrained by drilling data.

Temperature data from shallow wells measured as high as 58˚ C at 150 m. However, when deeper drilling was attempted the wells failed to intercept higher temperatures at depth and thermal gradients became isothermal below 530 m.

In terms of heat loss, estimations can be made into the size of the system using the sum of the surface heat flow above background conditions. An empirical relationship between the prospective energy production supported by the geothermal system and the total natural state surface heat loss states that production is equal to 1 to 10 times the natural heat loss (Williams, 2012; Wisian et al., 2001). An analysis of numerous temperature gradient wells most accurately characterizes the EMC and PM thermal anomalies and give production estimates of 8 MW and 25 MW, respectively, which implies an optimistic generation capacity potential up to 80 and 250 MW. For comparison the Dixie Valley power plant operates at 6 times the natural state heat loss.

The goal of the GPO exploration program was to apply several exploration methods and identify which tools or combinations of tools were most effective at delineating successful drilling targets. Exploration included shallow thermal characterization studies, acquisition of remote sensing data, detailed geologic mapping, fluid/rock geochemistry, and multiple geophysical exploration datasets. A significant amount of this work was completed through a partnership with the University of Nevada-Reno Great Basin Center for Geothermal Energy. Through this partnership 2-meter temperature probe surveys were conducted as a rapid and economical approach to identify and characterize the horizontal extent of shallow known and potentially unknown thermal anomalies (Skord, 2011). A LiDAR data set and low-sun-angle

photography were acquired and interpretations provided new mapping of Quaternary units and neotectonic structures in southern Dixie Valley (Helton, 2011). A hyperspectral remote sensing survey for hydrothermal alteration mineral surface mapping revealed previously unknown deposits of kaolinite, alunite, opal, chlorite, and gypsum (Figure 1.7) (Lamb, 2011). The GPO also drilled sixteen ~150-meter thermal gradient wells and analyzed fluids from two of the wells for isotope geothermometry.

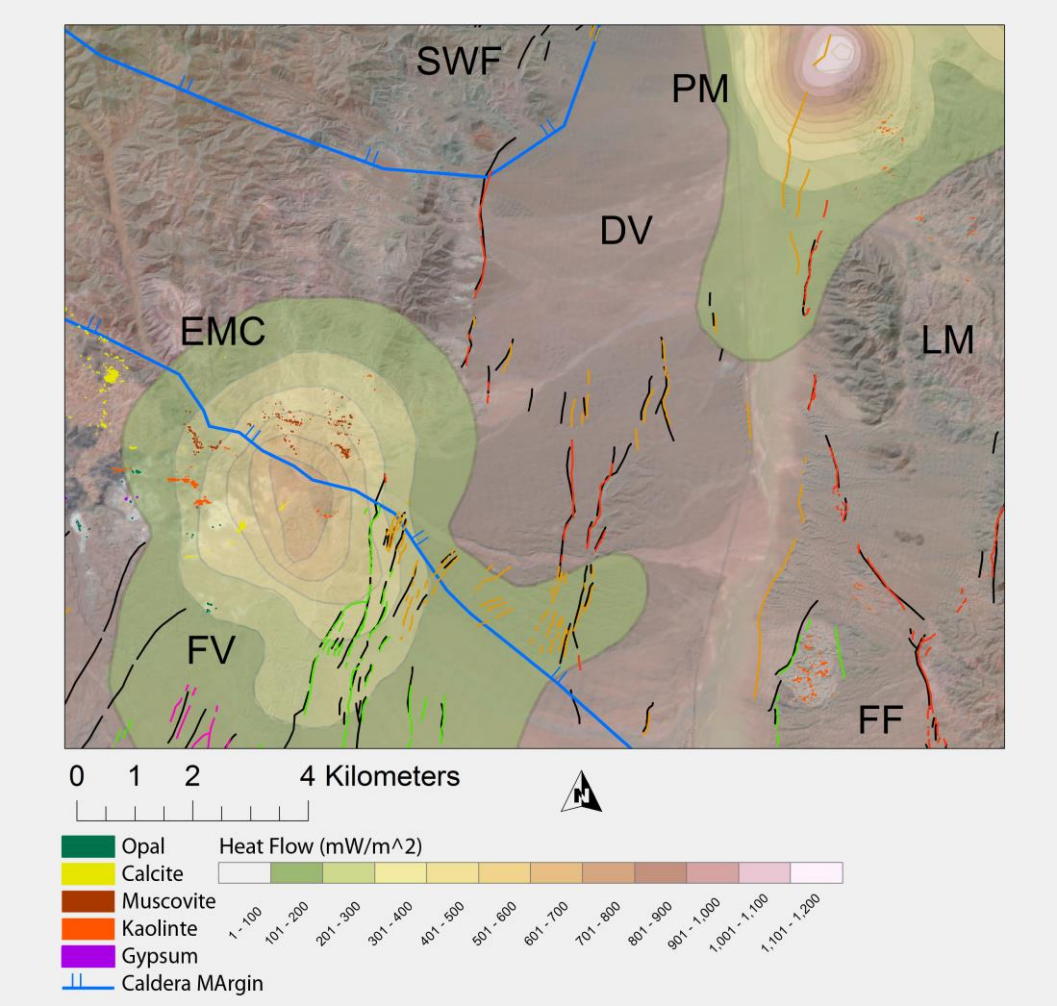

Figure 1.7. Digital elevation model of area outlining significant surficial hydrothermal alteration coincident with the Elevenmile Canyon (EMC) and Pirouette Mountain (PM) geothermal systems of interest, also includes Fairview Valley (FV), Louderback Mountains (LM), Dixie Valley (DV), Fairview Peak Fault (FF), and the Stillwater Range frontal fault (SWF).

1.2 **Purpose**

The purpose of this study is to develop initial structural models for the EMC and PM areas (Figure 1.5) in order to identify drilling targets. To best direct future drilling efforts, the development of models will rely on the integration of multiple datasets and includes six major

activities and/or datasets. 1) New detailed geologic mapping of mainly Neogene-Quaternary structures and map units in a major accommodation zone between range front faults. 2) Analyses of kinematic data from fault slip measurements for paleo-stress inversion in Stereonet 9 (Allmendinger et al., 2011), and the comparison of modern analogs using slip and dilation tendency analysis. 3) Ar-Ar dating on 5 samples of Miocene basalt and andesite flows that overlie a section of Miocene lacustrine sediments in minor angular unconformity to constrain the onset of the most recent period of deformation. 4) The interpretation of ~50 km of 2D seismic data, including velocity panels, acquired and processed to produce high resolution images of structures that offset blocks of anisotropic volcanic strata to ~4 km depth. 5) A reprocessed gravity dataset that includes ~100 new data points, specifically in areas of structural complexity and along select 2D seismic lines. 6) A new high-resolution, reduced-to-pole aeromagnetic survey to help delineate major structures.

This study will evaluate the stratigraphic and structural controls for geothermal activity as the initial model conditions that dictate fluid flow, with a focus on the geometry, kinematics, and mechanics of extensional faulting as it specifically relates to the EMC and PM geothermal systems. New detailed geologic mapping and fault kinematic data will be integrated with existing geologic map data in ArcGIS to establish the modern geologic framework in a digital format. New geochronology data will be used to constrain the onset of major Basin and Range extension for the region. Paleo-stress data derived from fault slip data will be compared to modern stress field data from borehole breakout studies and moment tensor data. Geophysical data from interpretation of aeromagnetic, gravity, and 2D-seismic data will establish the

orientation of major basin bounding structures and how potentially older buried structures might be interacting with active faults. All the data will be presented in a series of geologic cross sections that demonstrate the conflation of multiple datasets into a best fitting model of the subsurface conditions and to identify primary targets for exploration drilling.

2. Geologic Setting

2.1 Physiographic and Tectonic Setting

The southern Dixie Valley study area is located in west-central Nevada, about 200 km east of Reno, NV in the northern Great Basin of the western USA. The Great Basin is bound on the east by the Colorado Plateau, on the west by the Sierra Nevada/Walker Lane, on the south by the Mojave block, and to the north by the Snake River Plain (Figure 1.1). At 360,000 km^2 of internal drainage and rugged topography, the study area is at the Basin and Range's greatest width.

The northeast Great Basin may have begun extending as early as ~40 Ma (Henry et al., 2011). This is prior to development of the modern Pacific-North America boundary that is characterized by the inception and northward migration of the Mendocino Triple Junction (MTJ) at ~30 Ma (Atwater and Stock, 1998). However, this period overlaps with intense volcanic activity related to the ignimbrite flare-up, which may have initiated extensional strain in the Basin and Range. It is well documented that from 16-17 Ma (Dickinson, 2006, 2013; Fosdick and Colgan, 2008; McQuarrie and Oskin, 2010; McQuarrie and Wernicke, 2005) major extension was active throughout the region with an array of orientations for the extensional axes that

ranged from 280°-300° , with an average orientation of ~282° (Colgan, 2013; McQuarrie and Wernicke, 2005).

Modern GPS measurements suggest that around 25% of the Pacific-North American relative plate motion is partitioned onto strike-slip fault systems in the Walker Lane and eastern California shear zone (Hammond and Thatcher, 2004; Kreemer et al., 2009). Some of this motion is then transferred into the Great Basin in the form of extension. The Walker Lane is dominantly transtensional deformation along northwest striking faults with minor, yet pronounced, east-west oriented transpressive accommodation zones that separate the western Great Basin from the Sierra Nevada block. It extends from the southeast in the region of Lake Mead and the Garlock Fault to northeast California and the southern Cascade Arc with diminishing cumulative offset from south to north.

As a physiographic boundary, the Walker Lane can be described as diversely oriented ranges that separate north-northeast trending ranges of the central Great Basin from the north-south Sierra Nevada Mountain Range (Faulds and Henry, 2008; Faulds et al., 2005). Observations by Faulds et al. (2004) describe Walker Lane motion as decoupling of the Cascade Arc-Sierra Nevada block micro-plate from the Cordillera along the western Great Basin margin in a northwest direction with respect to a stable Colorado Plateau. The characteristic north-northeast striking normal faults of the Great Basin are a likely far-field response of progressive dextral shear plate motion transfer beyond the Walker Lane.

Dixie Valley is part of a broad region of high heat flow known as the Battle Mountain heat flow high (Lachenbruch and Sass, 1977) that overlaps a zone of pronounced Cenozoic tectonic

activity that extends from Reno, NV to Elko, NV known as the Humboldt Structural Zone (HSZ) (Figure 1.1) (Rowan and Wetlaufer, 1981). The HSZ forms the structural link between active displacement of the north-central Walker Lane to active displacement in the Wasatch belt of western Utah and southern Idaho (Rowan and Wetlaufer, 1981). The HSZ is most notably characterized by an abundance of anomalous east- northeast-striking (late Paleogene?) sinistral faults that likely formed as part of an early Mendocino Triple Junction (<30 Ma) related period of broadly distributed constrictional strain (Dewey, 2002; Faulds et al., 2003).

Zones where east-northeast-striking sinistral faults and major north-northeast-striking normal faults interact within a west-northwest directed extensional strain regime may enhance localized permeability through increased fault and fracture density. This idea is supported by the spatially coincident northeast trending belt of high temperature (>150^{o}C) extensional domain geothermal systems (e.g. Desert Peak, Dixie Valley, Beowawe, Tuscarora) known as the Humboldt Geothermal Belt (Faulds et al., 2003; Faulds et al., 2012a). The presence of several notable geothermal systems of central and northern Nevada occurring along or near major faults and zones of preferential fault interaction in the HSZ indicates strong potential for additional discoveries in the region through structural analysis (Faulds et al., 2003).

2.2 **Stratigraphic Framework**

The study area is underlain by Mesozoic metasedimentary and metavolcanic basement rocks, Eocene to Miocene volcanic and sedimentary rocks, late Neogene to Quaternary alluvium, and hydrothermal deposits related to Neogene and Quaternary alteration (Figure 2.1). The description below focuses on the Cenozoic rocks in the area.

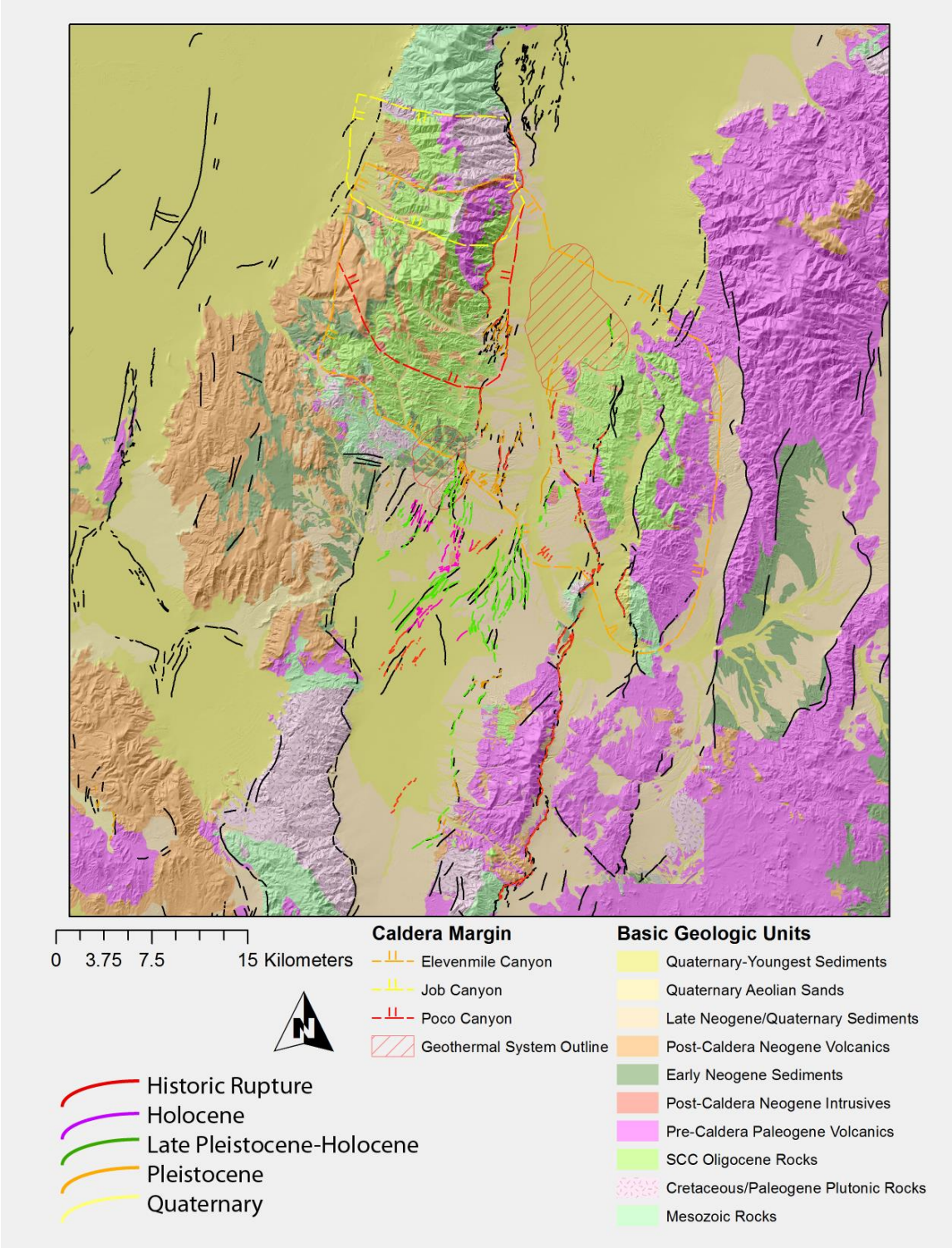

Figure 2.1. Basic geologic map of the study area as defined in figure 1.5 showing significant groups of stratigraphic units and structural features.

The study area coincides with the 29-25 Ma Stillwater Caldera Complex (SCC), which consists of three overlapping calderas and extends from the southern Stillwater Range east across Dixie Valley to the southwestern Clan Alpine Mountains. The SCC is a rare, well-exposed example of a multi-cycle caldera system with underlying plutons extended into tilted fault blocks in a 10 km cross section of outcrop. The south half of the SCC exposed in the southern Stillwater Range is tilted 55^{o}-75^{o} degrees to the east and is structurally distinct from the north half that is steeply tilted to the west 70^{o}-90^{o}. Tilting occurred during extension ca. 24-16 Ma (Henry and John, 2013; Hudson et al., 2000; John, 1995)

The oldest of the three eruptive centers is the 29 Ma Job Canyon Caldera that initially effused 1500 m of intermediate-composition lava flows before collapsing and erupting ~2000 m of crystal poor rhyolitic intracaldera ash flow tuff and a minor amount of resurgent lava flows. Volcanic rocks are intruded by the quartz monzodiorite IXL pluton. Following a ~3 Ma hiatus in volcanic activity, units related to the Poco Canyon (PCC) and Elevenmile Canyon (ECC) calderas and the adjacent Freeman Creek granite pluton were emplaced in a period of overlapping caldera volcanism. The PCC and ECC are defined by two distinct, but locally adjacent intracaldera tuffs, caldera-collapse breccias, a trachydacite ash-flow tuff of ECC, and locally derived tuffaceous sediments. The stratigraphic thickness of units associated with the PCC is in excess of 4500 m. The thickness of rhyolite to trachydacite ash-flow tuff and associated sedimentary units of the ECC exceeds 4000 m. The north and central areas of the PCC and ECC are intruded by the composite Freeman Creek pluton (Henry and John, 2013; John, 1995).

Post-caldera early Miocene igneous rocks include silicic intrusives, flow domes, and volcaniclastic sedimentary rocks. From K-Ar ages, paleomagnetic data, and field relations these rocks range in age from 25-22 Ma and formed during or after a brief period of earliest Miocene extension following cessation of major ignimbrite activity in the SCC (Hudson and Geissman, 1991; Hudson et al., 2000; John, 1992; John and Silberling, 1994). The early Miocene also produced a 15-km wide silicic dike swarm that extends from the southern ECC across Dixie Valley, the Louderback Mountains, and into the western face of the Clan Alpine Mountains. The dikes intrude and crosscut faults related to earliest Miocene extension, Mesozoic rocks, rocks of the ECC and PCC, and post-caldera rhyolites. The east-southeast orientation of the dikes may support a period of north-northeast directed extension.

A basin formed during this period may be represented by the Miocene non-marine sedimentary rocks that unconformably overlie Mesozoic and Tertiary rocks south of Elevenmile Canyon. The stratigraphic package consists of well-indurated siltstone, sandstone, pebble to boulder conglomerate, and ash-fall tuff deposited in lacustrine and fluvial environments (John, 1992; John and Silberling, 1994). Conglomerate clasts are sub-rounded to rounded and sourced primarily from tuffs of the ECC, Miocene silicic intrusive rocks, and sparse Mesozoic rocks. The basal contact is not exposed and the unit is highly susceptible to weathering, which makes for generally poor exposure and complicates estimations of thickness. The unit is estimated to be in excess of 250 m. Paleocurrent measurements taken in conglomerate outcrops near La Plata Canyon support the south-southwest transport direction suggested by John (1992). Initial age estimations for deposition (John, 1992) are based on an overlying hornblende andesite flow

unit with a K-Ar age of 15.3±0.5, suggesting an equivalent age for the uppermost part of the unit and a good deal of uncertainty for the age of the lowermost section.

A thick sequence (>500 m) of Miocene age lava flows that include flow breccias and minor pyroclastics conformably (or in very minor angular discordance) overlie the Miocene sedimentary rocks (John, 1992). John (1992) also provides ages ranging from 15.3 Ma for the hornblende andesite lava flows to 14.4-13.0 Ma for four samples of the basaltic andesite (Figure 2.3). The volcanic stratigraphy is further refined herein with 5 new K-Ar ages of associated flows, described in a later section.

Surficial deposits of Pleistocene and Holocene age drape large pediment surfaces that slope southeastward at multiple levels away from Elevenmile and La Plata Canyons into Fairview and Dixie Valley. The oldest units of Pleistocene age are two similar alluvial fan deposits characterized by the slight variation in development of calcic soils as a result of being subjected to periodic episodes of weathering. These fan deposits interfinger with a similar age fine-grained basin fill deposit and all unconformably overlie Miocene sedimentary rocks. The oldest Holocene age fans overlie beach bar deposits related to the 10.4-11.7 ka Lake Dixie highstand and contain the 6.85 ka Mazama ash. Late Holocene fans include 1.5 ka Mono Craters tephra. Neogene and Quaternary sediments combine to fill the modern basins of Dixie and Fairview Valley to depths beyond 2 km (Bell et al., 2004).

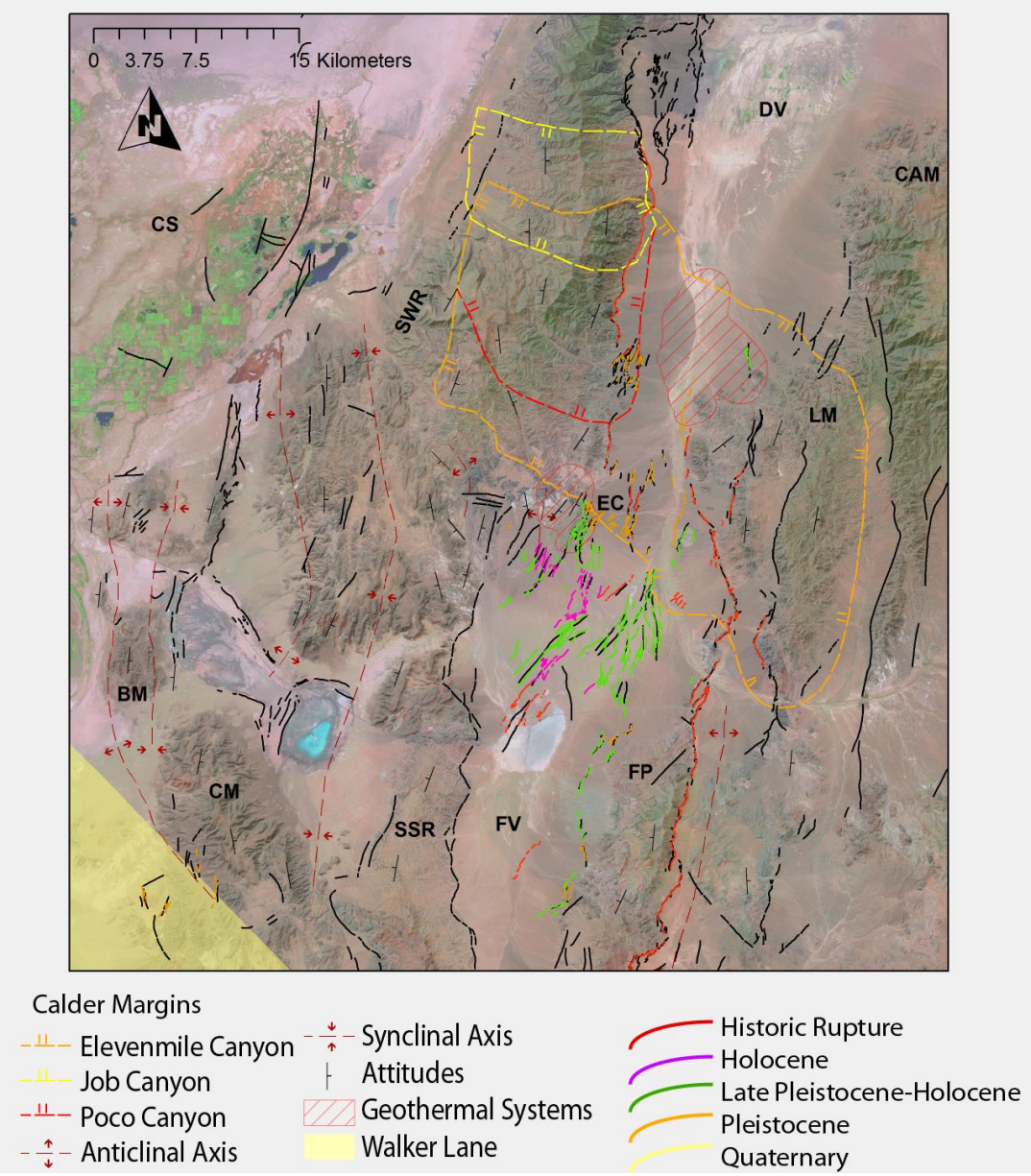

Figure 2.2. Digital elevation model, same scale as Figure 1.6, Dixie/Fairview Valley area map with heat flow anomalies depicted (Williams, 2012), including Job Peak (JP), Fairview Valley (FV), Louderback Mountains (LM), Dixie Valley (DV). Pirouette Mountain (PM), Elevenmile Canyon (EC), Bunejug Mountains (BM), Cocoon Mountains (CM), Sand Springs Range (SSR), Fairview Peak (FP), Stillwater Range (SWR), Carson Sink (CS), and Clan Alpine Mountains (CAM). Accommodation zone fold axes are displayed in dashed orange lines and faults as solid black lines with balls on downthrown side. Strike and dip direction is approximated from this and previous studies (Bell, Caskey, & House, 2009; N. Hinz, 2011; N. H. Hinz, Faulds, & coolbaugh, 2014; Page, 1965). Caldera Boundaries from Henry et al. (2013). Abbreviations from

2.3 Structural Framework (Oligocene to present)

Relative to the surrounding region of west-central Nevada, the geology of the southern Stillwater Range area is exceptionally complex. The oldest structures are associated with the emplacement of the Luning-Fencemaker allochthon and juxtapose lower Mesozoic phyllite above younger Late Triassic limestone at La Plata Canyon. The subsequent and highly prominent structures of the southern Stillwater Range are associated with the emplacement and collapse of the Job Canyon, Poco Canyon, and Elevenmile Canyon calderas of the late Oligocene. Large ring fractures define the margins of the three major calderas and can be traced across the valley into the Louderback Mountains.

The current structural framework is dominated by generally east or west dipping, north-northeast striking normal faults. This faulting is characteristic of the west-northwest directed extension in the northern Basin and Range province driven by transform motion at the plate boundary and dextral slip in the Walker Lane to the west. This deformation is responsible for development of prominent basins forming as a series of primarily moderately tilted horst and graben structures. Fairview Valley, for instance, is a large basin less than 10 kilometers wide that structurally forms a dominantly west-tilted half-graben with a basement depth beyond 2 kilometers. It is Fault bounded on the west by the moderately west tilted Sand Springs Range and on the east by the moderately west tilted Fairview Peak.

Northern Dixie Valley is similar to Fairview Valley because it is also a large, broad, deep basin of similar width and bound on the west and east by the frontal fault systems of the Stillwater Range and Clan Alpine Mountains, respectively. Southern Dixie Valley dramatically

narrows and shallows at the latitude of the northern Louderback Mountains. The Clan Alpine and Louderback Mountains are north-south oriented, east-tilted, fault blocks bound by moderate to steeply west dipping dip-slip faults. The majority of the northern Stillwater Range is a northeast-trending horst block bound on the west by the Rainbow Mountain fault and on the east by the Dixie Valley fault. The southernmost Stillwater Range is characterized by extensional accommodation zones that crisscross the range and define opposing zones of east- and west- tilted fault block domains.

The surrounding region contrasts in magnitude and style of extensional faulting with the study area in that it is characterized by Oligocene and Miocene strata that dips 15˚-30˚, compared to 50˚-80˚ in the SCC. The narrow, shallow graben of southern Dixie Valley also contrasts the broader, deeper basins that surround the area such as Fairview Valley, central and northern Dixie Valley, Carson Sink, Salt Wells Basin, Gabbs Valley, and Jersey Valley (Figure 1.5). Within the areas of steeply tilted strata, motion appears to have been accommodated by low

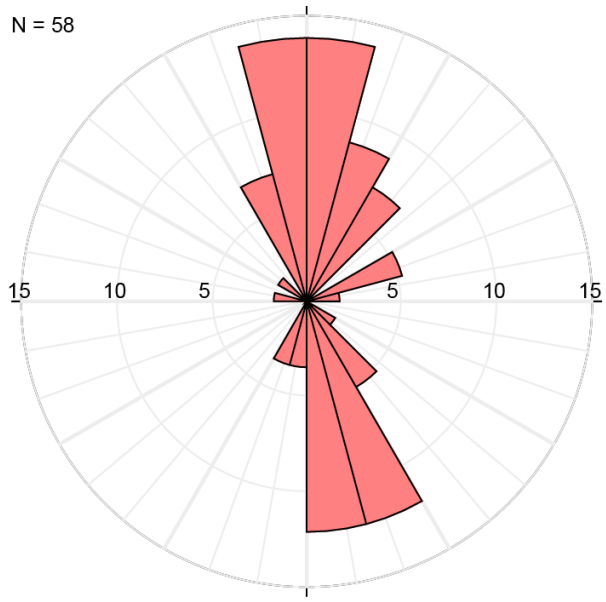

Figure 2.3. Rose diagram of all fault plane strike measurements collected in geologic mapping study area. Largest petals (>10%) represent over 50% of the dataset and demonstrate that the majority of faults measured strike northerly.

angle normal faults that have since been rotated out of kinematic favorability to near or past horizontal. The sub-horizontal faults are cut by younger moderate to high angle normal faults more closely related to the modern stress regime.

This pattern of two-staged extensional basin development is well documented across western and central Nevada, Wassuk Range/Walker Lake area (Cassel et al., 2014; Fosdick and Colgan, 2008; Lee et al., 2009; Oldow et al., 2008; Stockli et al., 2003; Gorynski et al. 2013), Sierra Nevada-Basin and Range transition (Fosdick and Colgan, 2008; Henry and Perkins, 2001) and central Nevada (Colgan et al., 2008; Fosdick and Colgan, 2008). However, the timing of onset and widespread vs. localized extension is not well constrained. Hudson et al., (2000) apply paleomagnetic data to support initiation of the first phase of extension at ~24 Ma, and Colgan et al. (2013; 2008) cite specific regional geologic relations to indicate Basin and Range extension starting around 17-16 Ma. Parry et al. (1991) and Waibel (2011) provide field

evidence for a rotation in the early to mid-Miocene east-west extension direction along north-striking faults to west-northwest extension developed on an array of NNE-striking normal faults kinematically linked to the older north-south structures. Regardless of the exact timing of the initiation of extension in the region and the viability of extension axis rotation, a two-stage deformation history complements the structural Framework of the SCC where gently tilted 16-13 Ma volcanic rocks rest on an angular unconformity on moderately-steeply tilted Late Oligocene-age volcanic strata associated with the SCC.

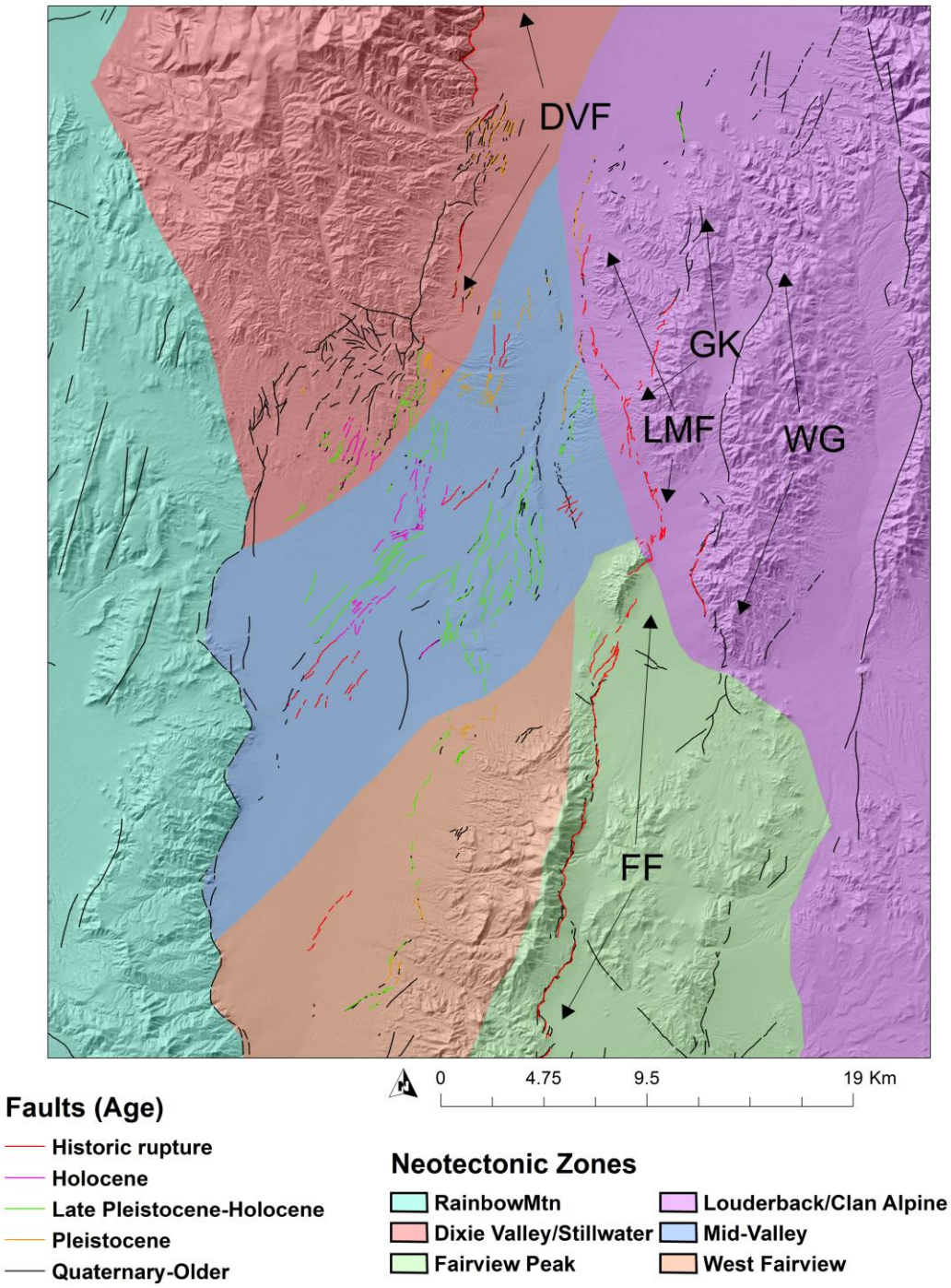

Figure 2.4. Neotectonic fault zones in the Dixie/Fairview Valley area. The zones are defined by the rupture pattern, orientation and distribution. Including the Fairview Fault (FF), Louderback Mountains Fault (LMF), Gold King Fault (GK), Westgate Fault, and Dixie Valley Fault(DVF).

2.4 A Review of Historic Seismicity

The study area is divided into 6 neotectonic structural zones primarily based on interpretations of orientation and historic rupture history as evidenced by previous researchers (Bell et al., 2004; Bell and Tingley, 1984; Caskey et al., 1996; Slemmons, 1957) and detailed fault mapping with high resolution LiDAR and low-sun angle photography (Calvin et al., 2012; Helton, 2011), field reconnaissance, and new mapping. These are shown on Figure 2.4: 1) Fairview Peak, 2) Louderback Mountains, 3) Dixie Valley, 4) Mid-valley, 5) West Fairview, and 6) Rainbow Mountain. The following descriptions of each neotectonic zone from the study area are based largely on interpretations from Calvin, et al. (2012) and Caskey et al (2004).

2.4.1 Fairview Peak:

This zone is characterized by right oblique, primarily down-to-the-east motion along north-northeast-south-southwest oriented structures, similar to the 1954 Fairview Peak earthquake (M7.1) (Figure 1.4) along the Fairview Peak fault a north-northeast-trending, east-dipping fault on the east flank of Fairview Peak (Figure 2.4). The surface ruptures associated with the event began in this southern zone with the Fairview Peak fault in the vicinity of Slate Mountain. It continued 32 km north to Chalk Mountain where it begins to form a left-stepping en echelon pattern before splaying into multiple, west-dipping fault strands. The surface rupturing event has as much as 3-4 m of offset, diminishing to ~1 m or less. This event triggered a second earthquake minutes later on the Dixie Valley fault.

2.4.2 Louderback Mountains:

This zone includes faults of the Clan Alpine Mountains and Louderback Mountains and the northern continuation of surface ruptures related to the 1954 Fairview Peak event. The eastern most rupture associated with the event occurs along the West Gate fault, which bounds the western edge of the Clan Alpine Mountains. Starting just south of highway 50, an 8 km rupture formed as a result of the event along the range-front salient and a 2 km rupture also formed along the range-front salient further to the north. The northern reach of this fault forms the eastern margin of the southern Louderback Mountains and suggests that the nature of the range is more akin to a tilted structural block being faulted away from the Clan Alpine Mountains than to a large structural block undergoing exhumation. A distinctive left stepping en echelon pattern that offsets Neogene volcanic was also observed from where the ruptures initiate

The Louderback Mountains fault is characterized by a series of discontinuous north-northwest oriented, right-oblique, down-to-the-west ruptures that formed during the 1954 event. They extend 14 km from just north of Chalk Mountain and along the western edge of the Louderback Mountains before terminating near the northern extent of the Louderback Mountains (Figure 2.4). The Gold King fault splays from the Louderback Mountains fault along a north-northeast strike and offsets Oligocene SCC rocks of the Louderback Mountains and bifurcates the Louderback Mountains structural block. West-facing ruptures generated by the 1954 event form an 8.5 km chain of discontinuous motion parallel to the West Gate fault 3-4 km to the east (Bell et al., 2004; Caskey et al., 1996).

2.4.3 **Dixie Valley:**

This zone comprises mainly of the Stillwater Range frontal fault system. Surface ruptures associated with the 1954 Dixie Valley earthquake (M6.9) start at Elevenmile Canyon and extend over 30 km northward. Maximum surface displacement occurred north of the project area and just south of the Dixie Settlement (Figure 1.5). Associated surface ruptures near Elevenmile Canyon occur at the Stillwater range front and splay into multiple strands that cut and terminate into the large alluvial fan at the mouth of the canyon. This termination of 1954 ruptures is spatially coincident with the known Elevenmile Canyon geothermal system. This zone is also coincident with a several kilometer-wide structural right step from the mouth of Elevenmile Canyon to active faults of the La Plata Canyon area and Sand Springs Range frontal fault system. This accommodation zone of numerous overlapping step faults of similar orientation and opposing dip direction results in a nested graben structures with some of the largest known Holocene fault offsets in Dixie and Fairview Valley (Bell et al., 2004).

2.4.4 **Mid-valley:**

This zone consists of northeast trending ruptures of limited length and displacement between the La Plata Canyon area on the west and the Louderback range-front zone on the east. An oblique orientation with respect to the N-S trending primary displacement zones of Dixie Valley and Louderback Mountains and a lack of cross cutting relationships with these adjacent zones strongly suggests this is a zone of structural linkage. The zone is characterized by NE-SW trending ruptures (including ruptures of 1954 event), originating near US 50 in the SW and terminating in the Louderback Mountains piedmont to the NE, that cross-cut older northerly striking faults that offset Neogene basin fill terraces. This zone appears to be a NE

projection of the Sand Springs Range-front fault system. The cross-cutting relationships and alignment with the Sand Springs structure suggests this zone formed under the modern stress regime and is kinematically linked to a recent history of large magnitude extension in the CNSB. Displacement within the zone appears to be purely normal, forming 25-30 cm scarps with no evidence of strike-slip offset. Some 1954 ruptures in this zone occur along older scarps, suggesting events with similar rupture patterns.

2.4.5 **West Fairview:**

This is a zone of N-S trending ruptures located on the western flank of Fairview Peak that appears linked to the older north-south ruptures of the Mid-valley fault zone. It also Includes a zone of northeast-striking, west dipping, 25-30 cm tall ruptures formed in a left stepping pattern at the southern end of Fairview Valley. The scarps appear fresh in LiDAR images and the left stepping rupture pattern is consistent with right lateral strain release. This suggests that the ruptures are associated with the 1954 event. Lack of access due to the presence of a highly active bombing range precludes field verification of this interpretation.

2.4.6 **Rainbow Mountain:**

This zone is characterized by east-dipping normal to right-oblique faults that bound prominent west-tilted half-grabens on their western margins. The basins are structurally linked by a 6 km-wide step over zone made up of a prominent west-northwest striking dextral fault. The Rainbow Mountain zone also includes surface ruptures from the 6 July and 23 August 1954 Rainbow Mountain-Stillwater earthquake sequence, which is defined by three moderate to

large earthquakes. The associated surface ruptures and numerous others are north-northwest- to north-northeast oriented, normal and right-oblique faults (Caskey et al., 2004).

2.4.7 **Neotectonic Summary:**

In summary, each zone can be characterized by late Pleistocene to Holocene multi-event surface ruptures that include ruptures from the well documented 1954 events. The Fairview Peak and Louderback Mountain zones experience right-lateral oblique-slip and the Dixie Valley zone is dip-slip motion. The Mid-Valley and West Fairview Peak zones appear to link Dixie Valley-La Plata Canyon-Sand Springs faults on the west with the Louderback Mountains zone on the east, a zone of mixed normal and right-oblique motion.

These zones also represent the central reach of the CNSB, a pronounced concentration of historical western basin and range seismic activity that stretches over 300 kilometers (Figure 1.4). This north-trending zone of moderate to large magnitude historic earthquakes includes the 1954 Fairview Peak and Dixie Valley events.

Prominent power-producing geothermal areas, Stillwater, Dixie Valley, Salt Wells, and Gabbs Valley, are all located in the CNSB and are associated with known faults, but none with historic rupture activity. They appear to manifest most strongly, commonly as fumaroles, near rupture terminations. This inspired an examination by Caskey and Wesnousky (2000), where they modeled increased stresses after earthquake ruptures at the rupture terminations. Their results suggest that hydraulic conductivity is improved by increasing brittle fracture dilatancy stemming from fracture development unaccompanied by decreased normal stresses that generate a higher ratio of shear stresses near the rupture terminations.

3. Methods

3.1 Detailed Geologic Mapping

New detailed geologic mapping of the area south of Elevenmile Canyon was completed in an examination of a major accommodation zone that structurally links the northern continuation of the Sand Springs frontal fault with the Stillwater Range frontal fault (Figure 3.1). Previous mapping of the La Plata Canyon quadrangle (John and Silberling, 1994) identified the tilted Tertiary rocks, but lacked the structural detail to explain the deformation history related to staged basin evolution and formation of local contractional structures formed in an extensional environment.

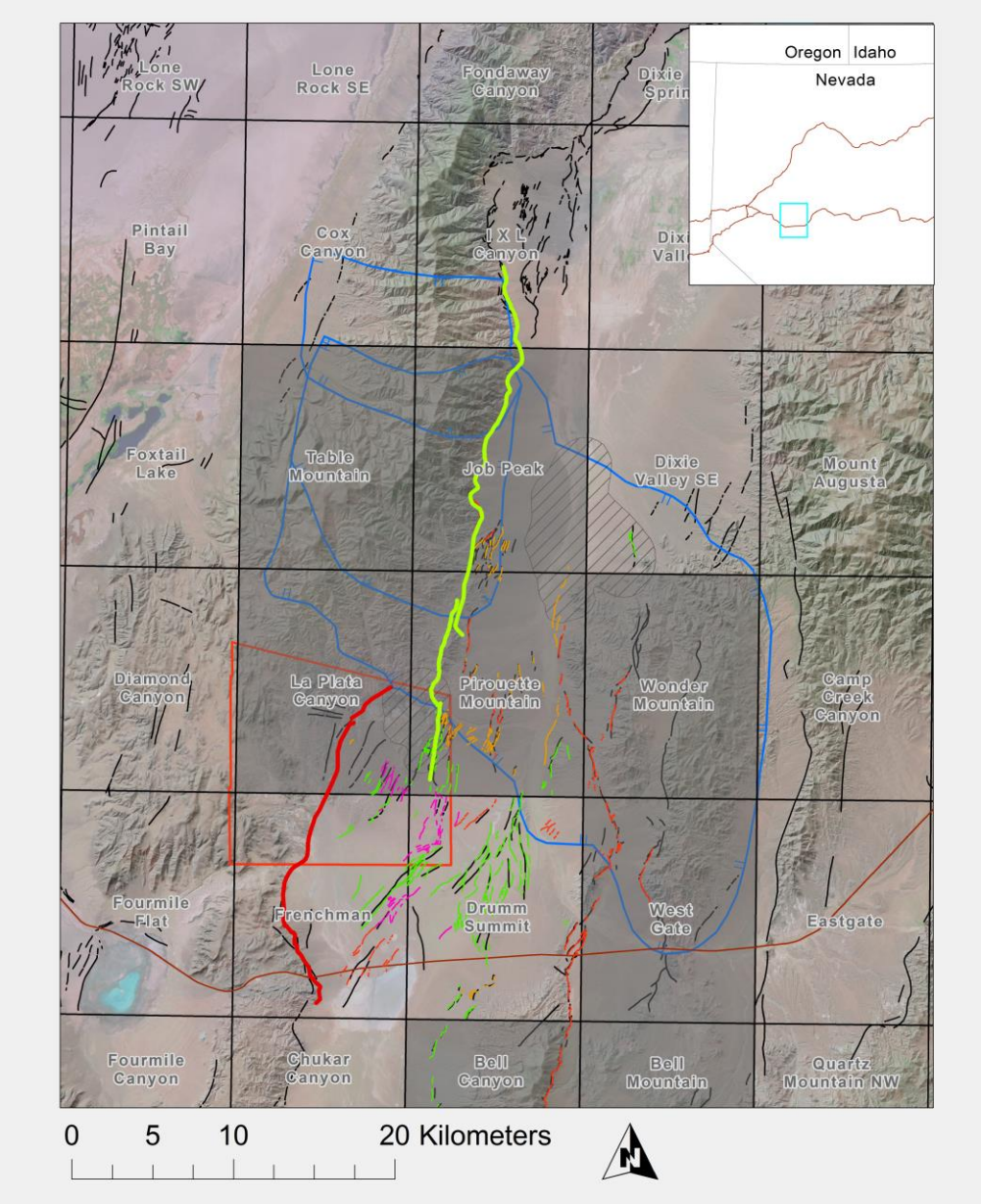

Figure 3.1. 7.5' Topographic map index with names, shaded quadrangles are previously mapped quadrangles. New geologic mapping conducted for this study is outlined in red. EMC and PM Geothermal Systems are outlined by grey hatch areas, SCC is outlined in Blue, Sand Springs frontal fault is the heavy red line, and the Stillwater frontal fault is the heavy green line. Fault coloring is from Figure 2.4.

Obtaining new data on strain indicators and/or previously unmapped faults was also critical in developing a hypothesis for the structural controls of the Elevenmile Canyon geothermal

system. The geothermal system occurs at the southern margin of the Stillwater Caldera Complex in Elevenmile Canyon, where a network of north-northeast-south-southwest trending faults cut a tilted Neogene sedimentary basin and Quaternary units before terminating into Mesozoic basement and Oligocene volcanic rocks. The interaction between this major right step in range-front faults, the numerous ring fractures associated with the Oligocene caldera margin, and the potential for reactivation of the margin as a fault during earlier periods of deformation present strong evidence for increased fracture density, dilation, and circulation of geothermal fluids.

Mapping was also used to clarify the structural relationship between the Neogene sedimentary basin and the overlying ~14-16 Ma Miocene volcanic sequence. This required an emphasis on determining the presence of an angular unconformity between the two units that would define their temporal relationship in terms of simultaneous or distinct periods of deformation for the two tilted units. The distinction would be supported by several Ar/Ar dates to refine the relationship.

Mapping also supported a more complete integration and interpretation of geophysical datasets, specifically 2D-reflection seismic data that could potentially image similarly deformed units. It also supports integration of geological data with available geophysical data by providing an exposed analog of potential subsurface conditions. In addition, I integrated large amounts of previously recorded data into a single ArcGIS geodatabase for ease of interpretation and generation of basin scale cross sections.

3.2 Fault Kinematic data

Structural data from the map area were compiled and analyzed using Stereonet 9 and FaultKin 7 (Allmendinger, 2014; Allmendinger et al., 2011; Marrett and Allmendinger, 1990). These programs were used to compute bedding and fault-slip data in examination of variations in the Neogene- to present stress orientation and stress ratios for the Dixie/Fairview Valley study area. Attitudes of exposed faults in and around the Neogene basin were measured along with orientations of kinematic indicators where present, such as slickenlines, for analysis of the slip sense and characterization of prominent fault populations (Angelier et al., 1985; Gauthier and Angelier, 1985).

Data were further interpreted using a moment tensor summation and the P-T-B dihedral stress inversion (Angelier, 1989; Marrett and Allmendinger, 1990), by which fault plane orientations and kinematic indicators are combined to generate a fault slip datum that can be converted to kinematic axes. Shortening-extension-intermediate kinematic axes or (P)ressure-(T)ension-(B)Intermediate are generated from each datum and the dataset is analyzed for mean vectors as a determination of principal paleo-stress axes. A linked Bingham distribution is also generated, which effectively determines a best-fit orientation for the entire fault-slip dataset (Allmendinger et al., 2011).

An examination of various stress tensors and their relationship with the orientation of young faults in the study area was conducted in an effort to identify critically stressed faults with the highest tendency for slip and/or dilation as primary sources for enhanced fluid flow. For this analysis we used 3D Stress, a program developed by Alan Morris et al. (1996) at the

Southwest Research Institute that rapidly computes slip and dilation tendency for all orientations of lines and planes by generating a shear stress vector for a given stress tensor. Stress tensors for the study were derived from a variety of sources including paleo-stress analysis, borehole breakout studies, geodetics, and historic rupture analysis. This method also allows for the evaluation of focal mechanism solutions as a proxy for regional stress orientations by qualitatively comparing slip tendency maps of various stress tensor origins.

3.3 **Ar/Ar Geochronology**

It is generally accepted that after 8-10 Ma approximately 30% of Pacific-North American dextral plate motion was accommodated by transtension in the Walker Lane-Eastern California Shear Zone and extension in the Basin and Range. The histories of extension and shear are less certain for the period from 25 Ma to 13 Ma and are placed in two models. One model interprets the ancestral Walker Lane as the locust for plate-margin dextral shear accommodation beginning around 22 Ma with mild, localized extension initiating closer to 25 Ma as a result of magmatism, then shifting to more widespread and intense extension from 15-13 Ma (Oldow, 1992; Oldow et al., 2001). The other model suggests extension was either moderate or nonexistent from 25 to 15 Ma and became extreme, but highly localized, from 15 to 13 Ma before giving way to widespread extension at ~10 Ma that continues today (Anderson et al., 2012).

To address how these interpretations might apply to the study area, I utilized $^{40}Ar/^{39}Ar$ geochronology on five samples of the post-caldera Neogene andesite and basaltic andesite that overlie the tilted Neogene basin sediments with a minor degree of angular unconformity. The

Neogene sediments unconformably overly the 25.1 Ma tuff of Elevenmile Canyon (Henry and John, 2013; John, 1995) and lack evidence of ash/tuff deposits related to the 19.48 Ma eruptions of the nearby Fairview Peak caldera that forms Fairview Peak (Figure 2.3) (Henry, 1996a, 1996b; Henry and John, 2013). This suggests that the age of basin formation and deposition, of the Neogene sediments is bracketed by the age of the Fairview Peak Caldera (19.48 Ma) and the stratigraphically lowest portion of the overlying volcanic sequence. Furthermore, based on their depositional relationship the majority of faulting, tilting and folding of the basin would have occurred after deposition of the stratigraphically highest portion of the volcanic sequence. Understanding these relationships allows us to test the two models and either lend support to one or suggest a possible alternative.

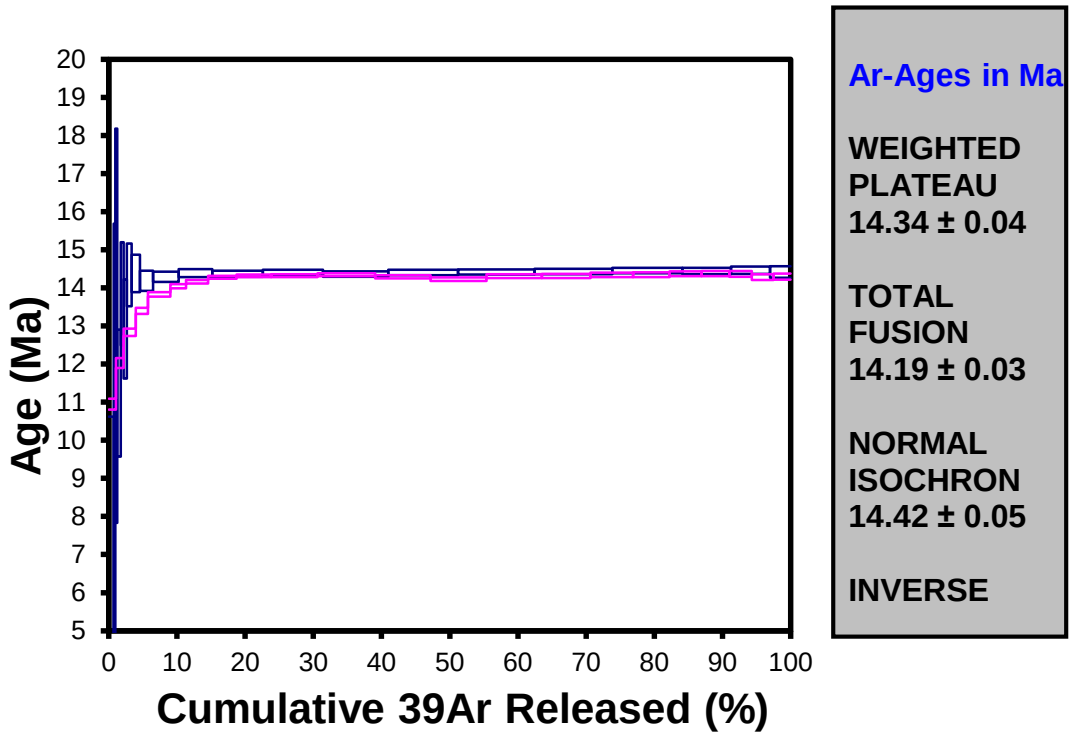

Figure 3.2. $^{40}Ar/^{39}Ar$ age spectra for sample LP-12. Ground mass step-heated age spectra in purple and plagioclase step-heated age spectra in blue overlain to review concordance between analysis methods.

Five samples were selected for their stratigraphic relationship to the Neogene basin. Mineral separates of plagioclase and whole-rock samples were analyzed using the $^{40}Ar/^{39}Ar$ step-heating method at the Oregon State Argon Geochronology Laboratory (OSAGL). Samples were cleaned, crushed, sieved, and washed in deionized water and dilute HCl in an ultrasonic bath. Mineral separates were prepared with a Frantz isodynamic separator and binocular microscope. All samples and the Fish Canyon Tuff biotite standard were irradiated for 6 hours at OSAGL's TRIGA experimental reactor. All samples were incrementally step-heated by

resistance furnace and then relevant masses were measured on a Scientific Model ARGUS VI multi-collector mass spectrometer (Figure 3.2).

Of the 5 samples analyzed, 3 produced robust plateau ages and 2 were likely affected by excess Ar related to hydrothermal alteration (Table 1). Analysis of plagioclase samples yielded distinct plateaus and concordant ages for samples LP-4, LP-10, and LP-12. Plagioclase analysis for sample LP-9 produced discordant data with a minor plateau and LP-7 produced no useful data and was removed from the study. Analysis of groundmass from each sample yielded slightly discordant data at best, typical of ground mass analysis. Plateaus were placed where the total fusion and inverse age were concordant with the plateau ages. Plagioclase and ground mass age spectra data were overlain from each remaining sample to review concordance between the methods (Figure 3.2). Sample LP-12 (Figure 3.2) was perfectly concordant and samples LP-10 and LP-4 are moderately concordant. The LP-9 groundmass age spectra are not well matched with the plagioclase age and therefore the plagioclase age alone was used for this sample.

Table 1. Summary of $^{40}Ar/^{39}Ar$ age data for Miocene Volcanic Rocks

Sample Number	Unit	Rock type and stratigraphic position	Material	39 Ar (%)	*N	Weighted mean plateau age (Ma)	Inverse isochron age (Ma)
LP-10	Mb	Basaltic Andesite flow in direct contact with LP-9	Plag, GM	25.74	14	15.02 ± 0.06	14.99 ± 0.04
LP-4	Tya	Basaltic andesite flow near contact with Neogene basin sequence	Plag, GM	31.19	18	14.92 ± 0.04	14.89 ± 0.05
LP-9	Mb	Basalt flow directly above LP-10 of Miocene basalt sequence	Plag, GM	33.48	12	14.86 ± 0.35	14.64 ± 0.73
LP-12	Tya	Andesite flow in the middle of the Miocene andesite sequence	Plag, GM	86.84	30	14.34 ± 0.05	14.39 ± 0.05
LP-7	Tya	Andesite flow from the lowest portion of Miocene andesite sequence	GM	22.85	5	16.14 ± 0.17 <No Plateau>	16.06 ± 0.55

Note: All errors are reported at 2σ (95% confidence). Plag - plagioclase; GM - groundmass
*Number of heating steps

3.4 **2D-seismic acquisition and interpretation**

Integral to this study was the acquisition of ~50 km of active source seismic data acquired by Optim Inc. for the GPO in southern Dixie Valley. Five profiles ranging in length from 6.5 to 16 km were acquired with geophone and shot point spacing of 33.5 m (110 ft) (Figure 3.3). In all, 1,456 receiver stations were occupied during the survey and each station utilized 3-component digital sensors. Shots were produced by two in-line 28.4 MT (62,500 lbs) vibroseis trucks that completed 10 sweeps, each 12 seconds long, ranging from 8-100 Hz at 1,402 source locations. Data were recorded for 5 seconds at a 2 millisecond sample rate. The survey design was based on previous successful surveys for geothermal exploration performed in the basin and range by Optim Inc. (Pullammanappallil and Louie, 1993; Rhodes, 2011, Unruh et al., 2006). Long offsets achieved through extended line lengths allowed for imaging of deeper and steeply dipping

structures. Initial velocity models were derived from first arrival times picked from the raw shot gathers and then depth extended using coherency optimization and interactive selection. The velocity model was then incorporated into a Kirchoff pre-stack depth migration algorithm for accuracy in travel time calculation and correct placement of reflectors at depth. Images are produced by summation of seismogram values based on travel-time calculations by way of the velocity model.

Depth migrated seismic reflection profiles and velocity models were used for interpretation of faults and stratigraphic horizons in IHS Kingdom Suite seismic interpretation software (Kingdom Suite). Assumptions pertaining to the dip of structures and bedding were not made in the pre-stack migration, thus images generated are more likely to reveal true-depth and geometry of laterally complex structure. However, caution was exercised when assessing single reflectors as significant structures or bedding. Confidence in reflectors of interest relied on characteristics relating to high-amplitude dipping features, appearance as a series or package of isolated or offset reflections, strong variations in velocity, or confluence of additive interpretations from surface geology, well log lithology, or other geophysical interpretation.

3.5 **Gravity and Magnetic Data**

Gravity surveys have proven an effective tool for understanding and interpreting the nature and extent of extensional basin geometries and associated fault systems in areas where subsurface constraints are scarce, such as Dixie Valley. Multiple efforts conducting gravity surveys and processing and reprocessing data to characterize basement structures in Dixie Valley and the surrounding area have been conducted (Abbott et al., 2001; Blackwell et al.,

2000; Mankhemthong, 2008; Schaefer, 1983; Williams, 2012). Selected data from these previous surveys were combined with over 100 new gravity stations by using standard reduction processes and applied terrain correction algorithm to generate the complete Bouguer map, assumed density of 2.67 g/cc (Figure 3.3). New stations were acquired along long-offset 2-D reflection seismic survey lines for direct data comparison and joint modeling and focused in areas where critical structural elements were not clearly defined.

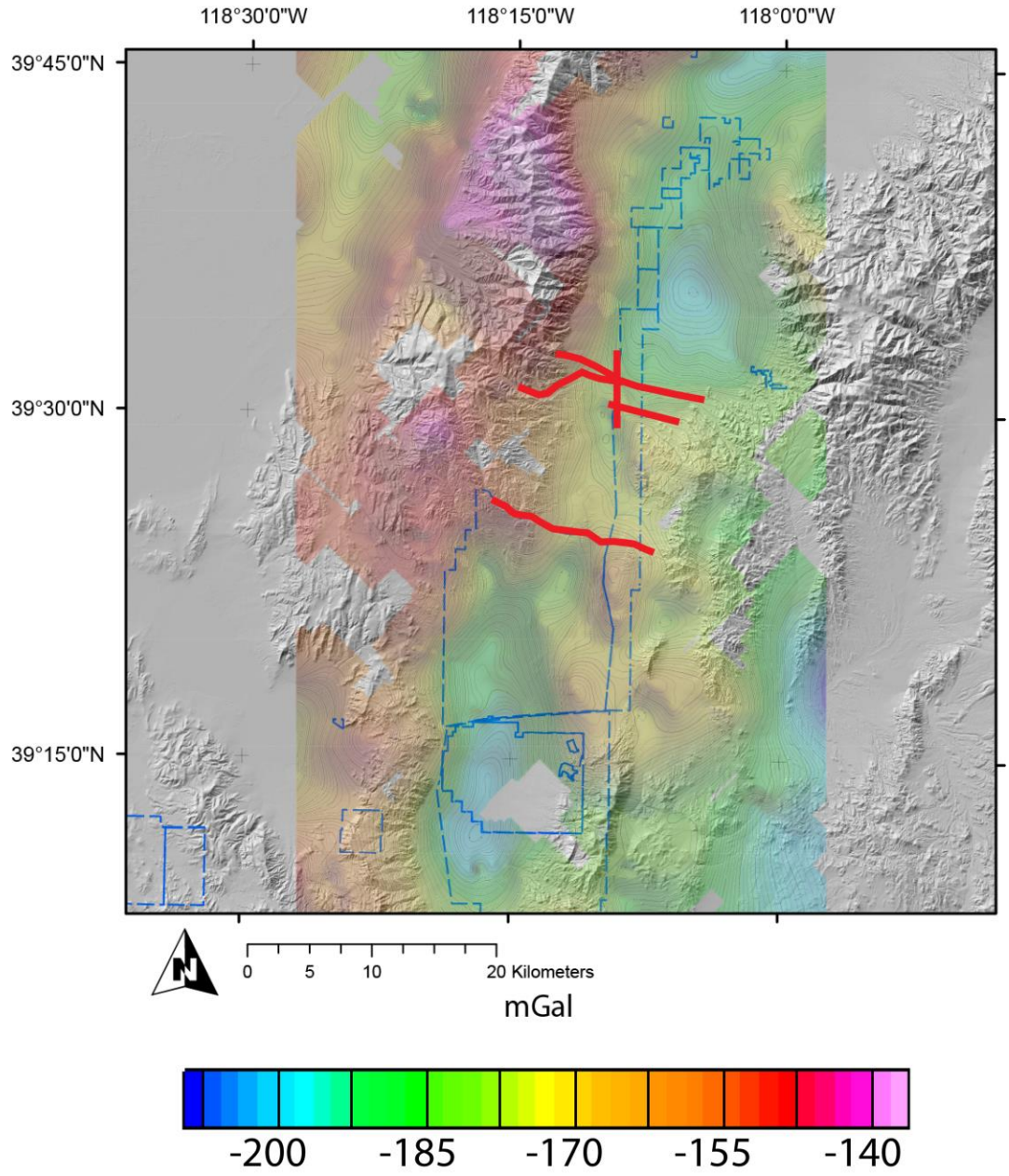

Figure 3.3. Complete Bouguer Anomaly 2.67 g/cc map. Red lines represent 2D-seismic acquisition profiles. Blue outline is the Dixie Valley Training Complex coincident with the study area.

In April of 2012 EDCON-PRJ, a well-respected aeromagnetic data acquisition and processing service company, acquired and processed aeromagnetic data over the study area, under

contract to the GPO, and tied it into a previously acquired dataset flown over the Clan Alpine Wilderness Study Area by the USGS. The new survey covered 593 square kilometers of mountainous terrain and gently sloping pediments ranging in elevation from 1200 m to 2300 m. A total of 3,342 line kilometers were acquired along 159 primary survey lines at a 200 m line spacing. The survey was a fixed-wing-borne, cesium-vapor magnetometer flown with an average of 217 m of terrain clearance. EDCON-PRJ corrected, reduced, and then leveled the data at tie line intersections before the data were reduced-to-pole. Reduction to the pole diminishes polarity effects that are the result of geometric obliquity of magnetized bodies in reference to the inclination of Earth's primary magnetic field (Blakely, 1996). The transformation relocates magnetic anomalies to a position that more accurately reveals the source bodies. The final reduced to pole grid calculation was based on a 63.53˚ inclination and a declination of 13.68˚ (Figure 3.4).

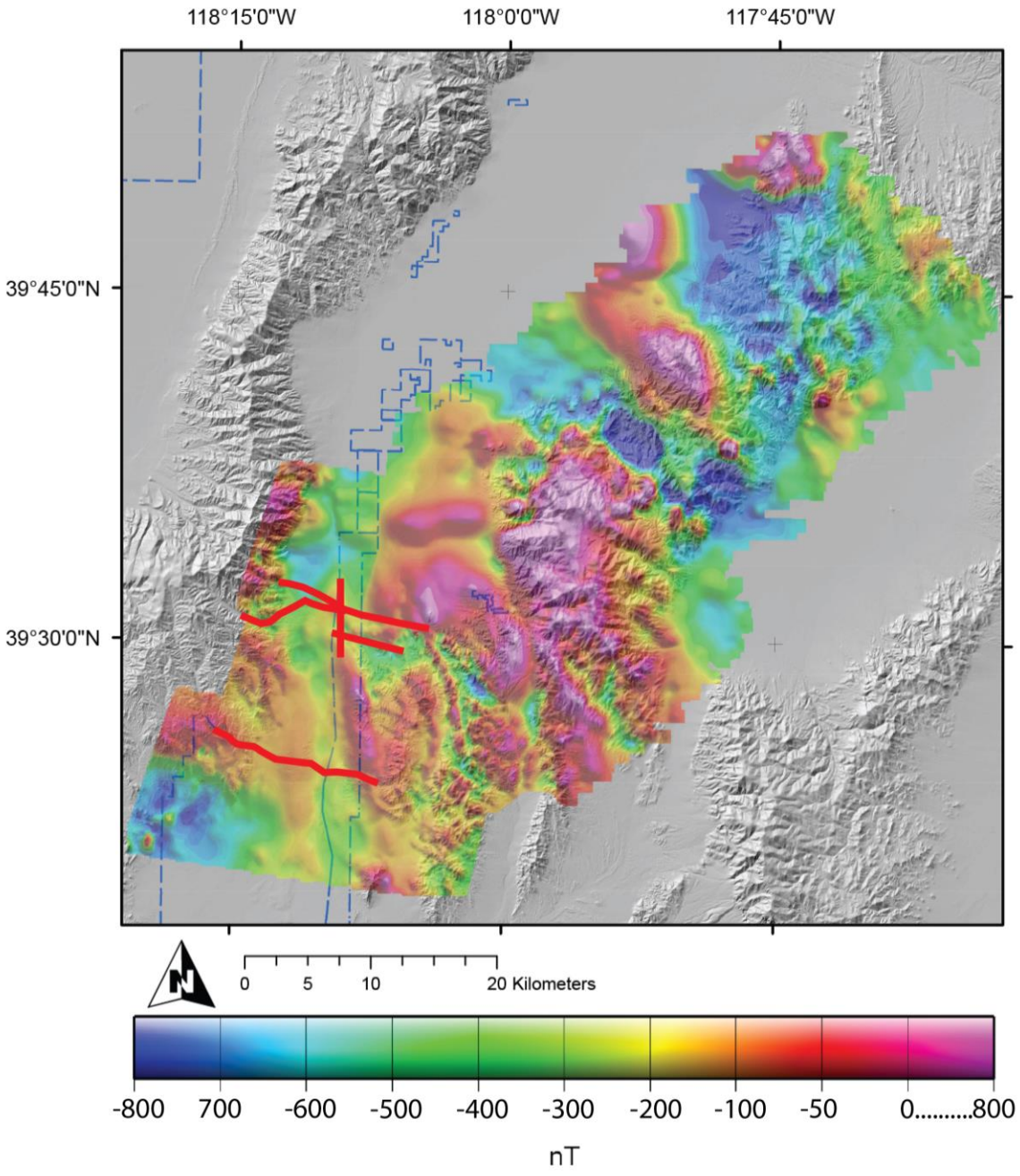

Figure 3.4. Color contour map of the aeromagnetic reduced-to-pole (RTP) anomaly map . Data has been corrected for magnetic inclination based on the surveys proximity to the North Pole.

The complete Bouguer gravity and reduced-to-pole magnetic data were gridded and initially interpreted using Geosofts Oasis Montaj software and were then imported to ArcGIS so that the data could be integrated with the larger body of work. Structural maps were developed by overlaying these images with Quaternary fault locations and examining relationships between the presence of neotectonic structures and distinct lateral variations in magnetic susceptibility and density (Figure 3.5). This step was critical for understanding the geometry of faulting where it has otherwise been masked by high rates of deposition, particularly in the area southern Dixie Valley where the PM geothermal system is located. I also applied the data to reinterpret the position of the caldera boundary by examining the magnetic response of areas known to represent the boundary from geologic mapping in the ranges and extrapolating that relationship into the subsurface.

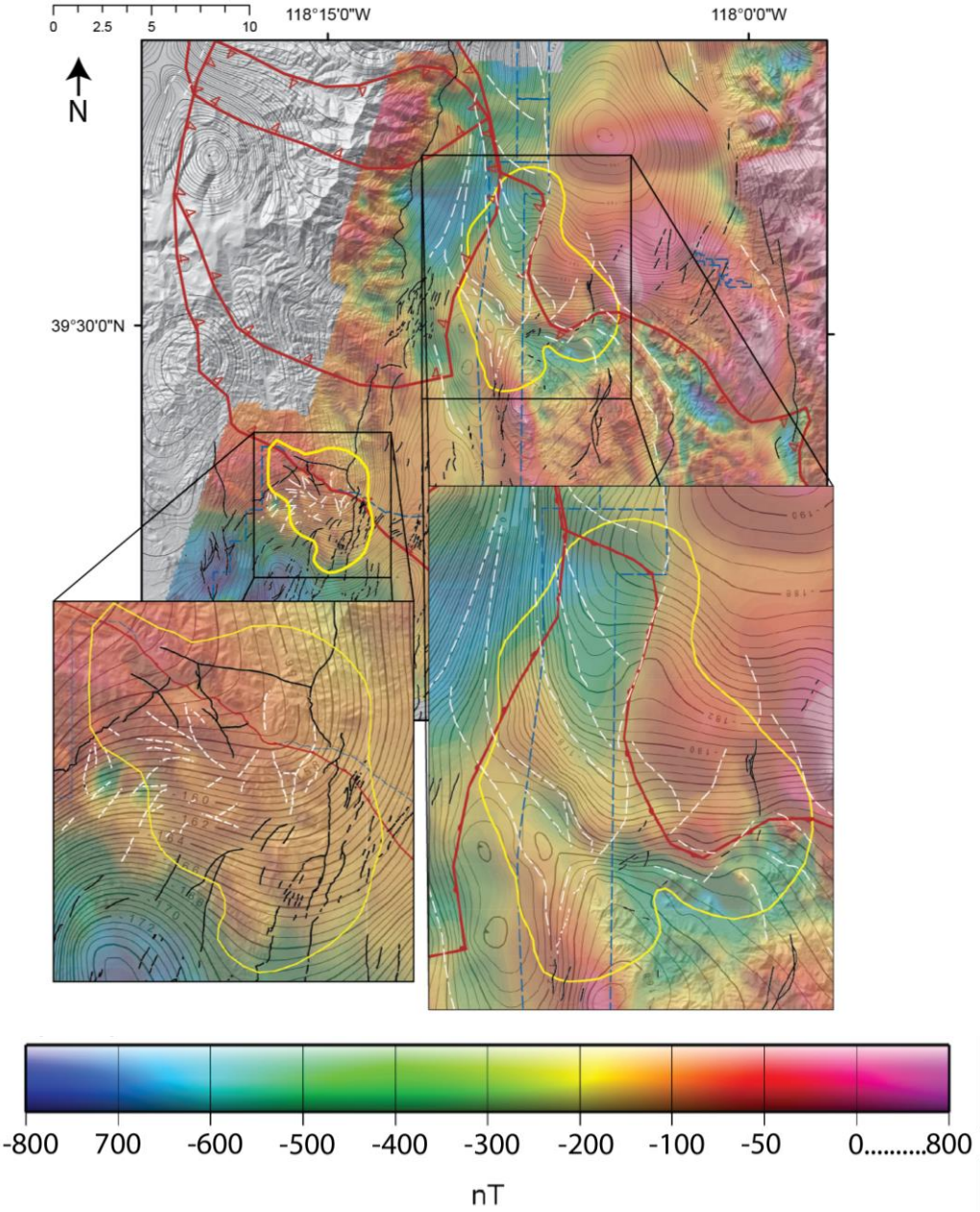

Figure 3.5. Structural interpretation of gravity and magnetic data in poorly characterized areas significant to PM and EMC geothermal systems. Gridded color map is reduced to pole magnetic anomaly data, scale is nT. Complete Bouguer anomaly overlain as 2 mgal contours. Quaternary faults are displayed as black lines and new fault interpretations are displayed as dashed white lines. Reinterpreted caldera margin displayed in dark red, half circles denote interior side. Navy training range outlined in dashed blue line for reference.

3.6 Structural Model

The development of the 3D structural model was completed through progressive iterations of geophysical and geological interpretations, such as detailed geologic mapping, fault rupture surface trace analysis, stress tensor data derived from kinematics, earthquakes, and borehole breakout studies. The faults were then characterized and prioritized based on their potential for impact on fluid behavior. The final 3D planes were modeled in Kingdom Suite and then exported to 3D stress for analysis of slip and dilation tendency. The apparent intensity of slip and dilation can then be compared to thermal models and interpretations made for future exploration targets.

4. Results

4.1 Seismic interpretation

Seismic lines 1, 2, 3, 4 and 5 were acquired along access roads that coincide with the Pirouette Mountain and Elevenmile Canyon geothermal systems (Figure 4.1). Lines 1, 2, 3, and 4 were oriented east-southeast to achieve image sections that were near perpendicular to the strike of known faults. Line 5 was shot in a north-south direction that intersects Lines 1, 2, and 3 so that horizon and fault interpretations could be made with greater confidence between lines that did not intersect. Seismic line 1 starts in the western piedmont of Dixie Valley near the mouth of Coyote Canyon and runs 8.2 km east-southeast, crossing the valley bottom and terminating at Line 2 (Figure 4.1). Line 2 starts in the drainage of East Lee Canyon within the Stillwater Range and west of the frontal fault. From East Lee Canyon Line 2 extends 15 km (9.4

miles) across Dixie Valley and up the eastern piedmont to the upper section of the Hercules Canyon alluvial fan (Figure 4.1). Line 3 starts 2 km south of Line 2 and runs roughly parallel to the east-southeast for 6 km (3.7 miles) to the Louderback Mountains range front (Figure 4.1). Line 5 starts 2 km south of Line 3 and continues 6.4 km (4 miles) north and ties Lines 1, 2, and 3 together before terminating ~3 km north of Line 1.

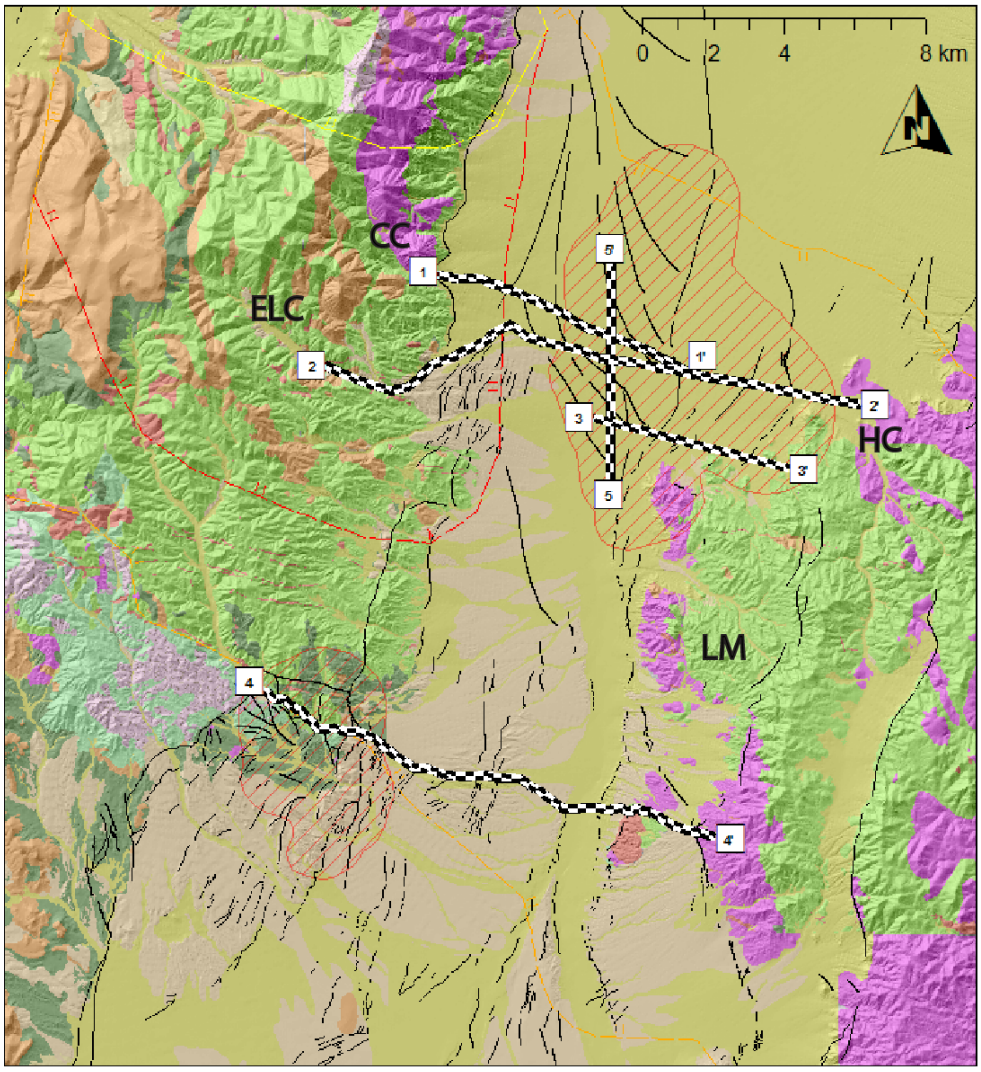

Figure 4.1. Geologic map from Figure 2.2 with 2D-seismic line locations as black and white checkerboard lines and integrated structural interpretation from gravity and magnetic data, faults are black lines. Labels refer to following locations Coyote Canton (CC), East Lee Canyon (ELC), Hercules Canyon (HC), and Louderback Mountains (LM).

The western section of Lines 1 and 2 cross a major relay ramp in the southernmost Stillwater Range frontal fault (Figure 4.2). The relay ramp interior is characterized by multiple Pleistocene and younger faults of opposing dip direction that includes 1954 ruptures of notable structural complexity in terms of terminations, and intersections. The eastern edge of Line 2 is

the only other intersection with a Quaternary structure, a north trending, west dipping normal fault (Figure 4.2). The central part of the survey overlies the PM geothermal system.

The seismic stratigraphy expressed in Lines 1, 2, 3, and 5 is defined by an uppermost Quaternary unit of unconsolidated basin fill that appears in the seismic sections as an upper section of thinly layered sediments and a lower section of more thickly layered sediments (Figure 4.1 and Plates 1-6). The variation in thickness of layering may suggest periods of differential uplift, where high sedimentation rates resulting in thick layering are driven by high tectonic uplift rates and vice versa for thin layering of sediments. This concept also resolves the slight variation in degree of dip between the thickly layered section that is more tilted to the west than the thinly layered upper section (Figure 4.3). Imaged fault offsets in Lines 1 and 2 image gentle tilting of Quaternary sediments to the west and support half-graben morphology in these sections (Plates 1-11) as a result of dominant down to the East displacement along the Stillwater Rage Frontal Fault (Figure 4.3). The greatest offsets in the Quaternary unit appear to coincide with the northward terminating portion of the relay ramp in the frontal fault of the Stillwater Range (Figure 4.2 and 4.3). The base of the Quaternary unit is defined in Figure 4.3 and Plates 1-10.

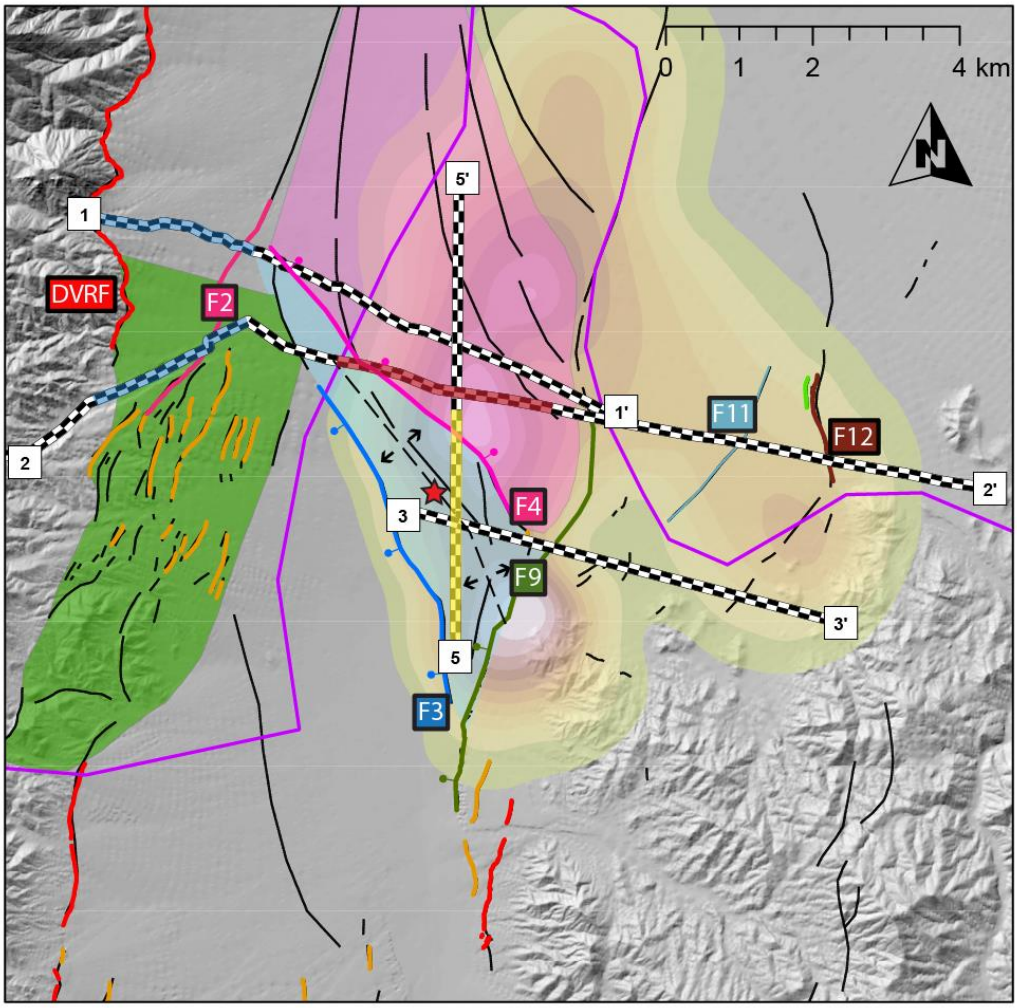

Figure 4.2. Detailed structure map of the northern seismic survey area that includes Lines 1, 2, 3, and 5 as black and white lines with labels. Red shading on seismic line 2 represents section from Figure 4.3, blue shading represents sections in Figure 4.4, and yellow shading represents the section in Figure 4.5. Red lines are faults with historic ruptures, orange are Pleistocene age, green are Holocene age, black are Quaternary or older, and purple lines are interpreted as potential caldera boundaries. Faults with balls on the downthrown side are color coded and generally represent the near surface projection of faults from the seismic interpretation in the following figures. The blue fault represents Fault 3, the pink fault represents Fault 4, and the dark green fault represents Fault 9. The relay ramp in the Stillwater Range frontal fault is shaded in green, the axial portion of the accommodation zone is shaded in pink, and the oblique anticlinal accommodation zone is shaded in blue and the corresponding fold axis is a dashed black line with arrows indicating direction of tilted strata. Red star denotes location of the 66-16 Hunt Energy well. Colored squares correlate fault surface traces with near surface projections of fault interpretations from the seismic sections.

The stratigraphy below the Quaternary fill includes tuff, latite porphyry, and rhyolite associated with SCC volcanism. There is a clear angular unconformity visible in the seismic data at the base of the Quaternary unit where broad packages of reflections in the volcanic section appear to have a higher degree of tilting (Figure 4.3). These more steeply tilted reflectors also appear to terminate abruptly against a group of reflections, similar in amplitude, but more steeply tilted in the opposite direction near shotpoint 480. This is shown in Figure 4.3 and is denoted by the green shaded area that appears to terminate against the purple shaded area. This relationship is interpreted to be a faulted contact between similar volcanic units of the SCC along a fault that has been rotated about a horizontal axis in the modern hanging wall of the frontal fault to an orientation no longer compatible for slip within the modern stress regime, i.e. the dip of the fault is too shallow. This boundary may also represent a caldera margin within the SCC, possibly between the Poco Canyon and Elevenmile Canyon calderas, as suggested by the caldera boundary approximation in Figure 4.2.

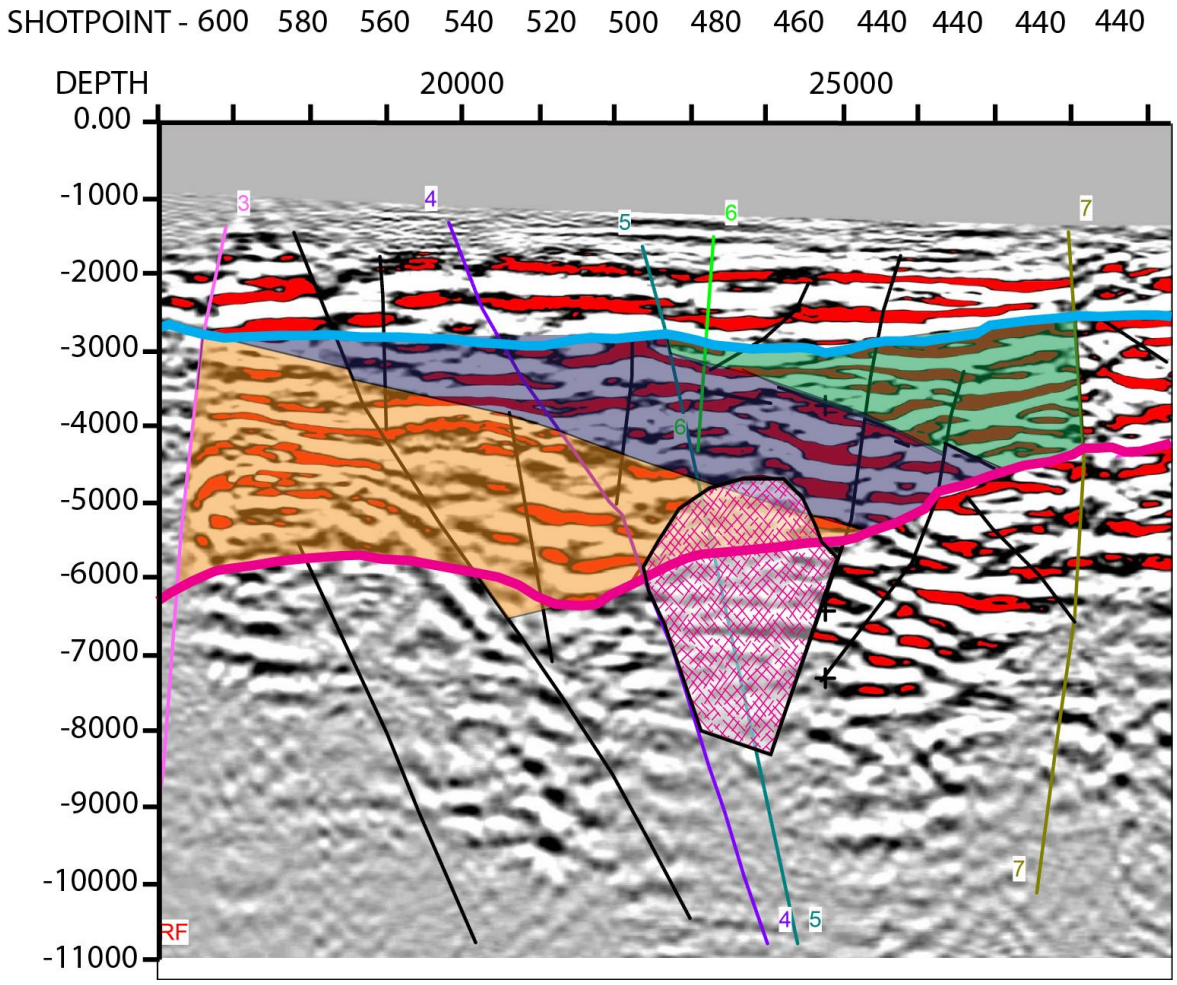

Figure 4.3. Line 2 seismic section as defined in Figure 4.2. Faults are colored and numbered. Base of Quaternary is the uppermost horizon, colored light blue. The pink horizon represents the base of SCC stratigraphy contact with underlying basement. The bell-shaped maroon horizon defines the "washout" zone described in the text. Shaded areas define variable dip domains in the SCC section bound by rotated faults, caldera margins or possibly both. There is no vertical exaggeration. Full section in Plate 2. Shotpoint station numbers are labeled at the top of the figure. Depth and distance are labeled in feet and there is no vertical exaggeration.

A second low angle structure dividing zones of apparent dip variation is also denoted in Figure 4.3 by juxtaposition of the purple and orange shaded zones. The down-dip projection of this structure intersects Fault 4 and appears to be associated with a zone of anomalously low amplitudes and poor reflections, as indicated by the pink hachured zone (Figure 4.3) commonly

referred to as a “washout” or “dimout,” that coincides with the surface location for the known thermal anomaly at Pirouette Mountain. The low amplitudes and poor reflectivity associated with the “washout” are anomalous given the central location in the seismic section, which makes it the highest fold, and the relatively well imaged surrounding area. Fold refers to the redundancy of common depth point (CDP) data, i.e. the number of seismic traces that imaged the same point in the subsurface, and allows for the assumption that areas of high fold are commonly well imaged. The “washout” also appears to be associated with a steeply, north-northeast dipping structure where the Louderback Mountains Fault steps over at Pirouette Mountain to the Stillwater Range Frontal Fault (Figure 4.2). This phenomenon could be explained as an area of intersecting faults that generate a zone of high fracture density and increased permeability. This could cause hydrothermal alteration that can affect the strength/rigidity of the host rock. The combination of these effects on rock strength have a direct impact on the seismic response seen in Line 1 and is further supported by a similar “washout” response in Line 2 (Figure 4.3).

Below the SCC stratigraphy of tilted, folded, and faulted reflectors is a third package of broader amplitude reflections, the pink horizon (Figure 4.3 and Plates 1-10) that I interpret as volcanic basement, possibly linked to the Freeman Creek pluton exposed in the northern SCC (Figure 2.1). This seismic section may also include pre-Cenozoic metamorphic rocks of the Clan Alpine Sequence that may be associated with discrete packages of strong reflections in the deeper part of all sections where coherency and reflection amplitude give way to affects associated with attenuation (Figure 4.3 and Plates 1-10).

The Dixie Valley fault (DVRF) is identified in Line 1 as the termination of irregular and sparsely continuous reflectors primarily associated with the Upper and Lower Quaternary section and the uppermost ECC section. A discrete package of steeply dipping reflections juxtaposed against a less steeply dipping package of reflectors is also interpreted as a faulted contact near shotpoint 460 at ~-1800 m (-6000 ft) depth. The DVRF resides in a low fold section on the western edge of Line 1 and results in a poor reflection image of the steeply dipping structure. The DVRF is identified in Line 2 as displacement across continuous reflectors of the Upper and Lower Quaternary (Figure 4.4 and Plates 1-4). Sparse reflections in the shallow seismic section coincide with a prominent dip-discordance, where east-dipping reflections interpreted as SCC volcanic units and the underlying west-dipping reflectors of the basement terminate against the DVRF (Figure 4.4). The dip of the DVRF in the seismic sections in Figure 4.4 are ~60˚ near the surface and may steepen slightly at depth, but are more or less planar to depths beyond 3,000 meters in Lines 1 and 2 (Figure 4.4). The DVRF appears slightly less steep in Line 2 due to the slight obliquity of the line orientation to the DVRF as it exits Coyote Canyon and descends the alluvial fan (Figure 4.1).

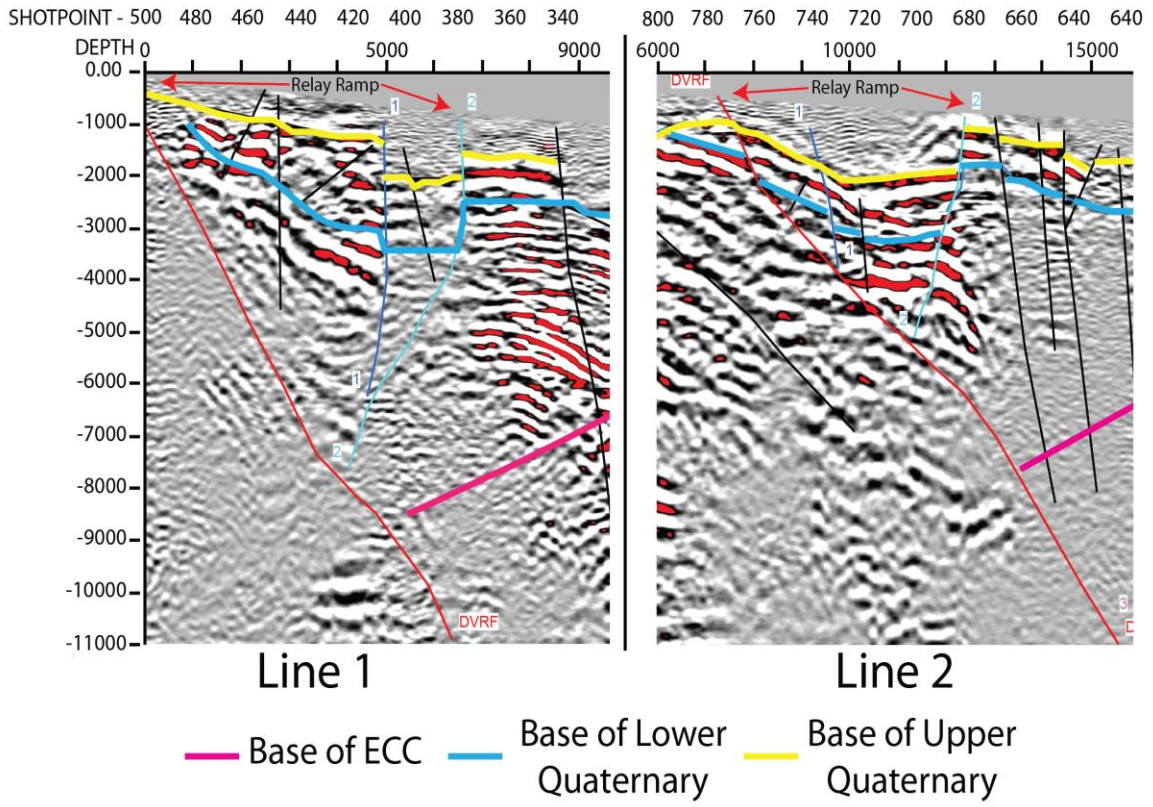

Figure 4.4. Sections of Lines 1 (left) and 2 (right) from Figure 4.2 that image the Stillwater Range frontal fault (DVRF) and faults associated with the relay ramp (Figure 4.2). Full seismic sections can be viewed in Plates 1 and 2. Shotpoint station numbers are labeled at the top of the figure. Depth and distance are labeled in feet and there is no vertical exaggeration.

The relay ramp geometry (Figure 4.2) is also visible in the seismic sections of Lines 1 and 2 (Figure 4.4). The near surface projection of faults 1 and 2 correlate spatially with the horse-tailing pattern observed at the surface within the relay ramp of the Stillwater Range front fault at East Lee Canyon (Figure 4.1 and 4.2). Fault 2 is a west-dipping fault that forms a minor hanging wall graben with the DVRF and a graben in graben structure with Fault 1, which is interpreted as the steeply east-dipping termination of the southernmost Stillwater Range

frontal fault (Figure 4.2). Offset of prominent reflectors in the Quaternary section appear to be as much as 900 meters along the DVRF and 180 meters along Fault 2 (Figure 4.4) for a cumulative offset that exceeds 1 km.

Faults 3 and 4 are oriented slightly antithetic to the dominant structural trend in Dixie Valley and define the anticlinal accommodation zone (Figure 4.2) that coincides with the northwest trending intrabasin high described in the interpretation of surface geophysics (Figure 3.6). Faults 3 and 4 can be viewed in Lines 1 and 2 (Figure 4.3 and Plates 1-4) and the northeast dipping Fault 4 is also visible in Lines 3 and 5 (Figure 4.5 and Plates 5 and 9). Lines 1 and 2 offer the best cross sectional profile of the complexly faulted intrabasin high and Line 5 displays the north directed basinward transition and Fault 4, but due to the low fold on the southern edge of Line 5 the intrabasin high is not imaged well (Figure 4.5). Fault 4 also offsets a north-northeast dipping panel of basement strata (Figure 4.5) that forms the northeast limb of the oblique anticlinal accommodation zone (Figure 4.5). Fault 4 is critical to the study due to its proximity to the near surface heat flow high and its apparent nature to block geothermal fluid flow across the intrabasin high (figure 4.2).

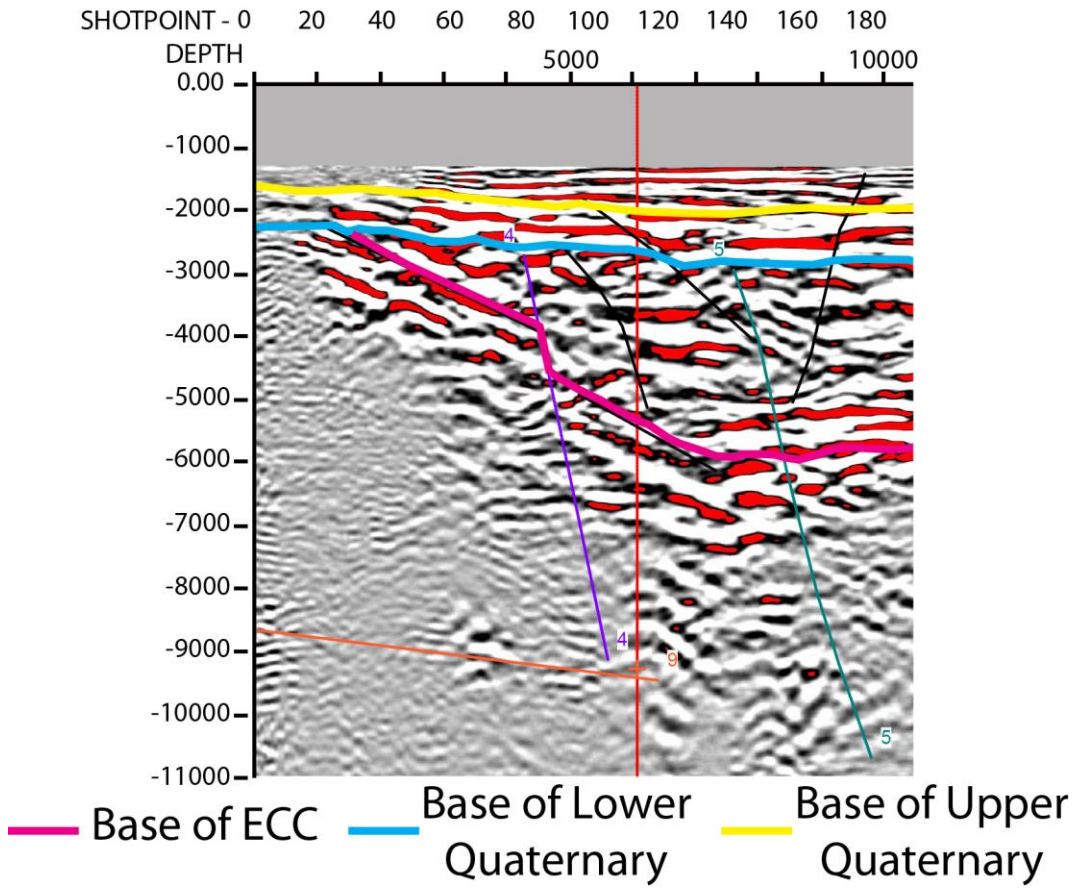

Figure 4.5. Seismic section of Line 5 as defined in Figure 4.2. Faults 4 and 5 define major structures on the northeast limb of the oblique anticlinal accommodation zone (Figure 4.2). The base of SCC strata, represented by the pink horizon was measured to have ~100 meters of offset across fault 4. Red vertical line represents intersection with Line 2 (Figure 4.2). Shotpoint station numbers are labeled at the top of the figure. Depth and distance are labeled in feet and there is no vertical exaggeration.

Faults 5-8 (Figure 4.5 and Plates 1-3, and 5) are north to northwest oriented, steeply dipping structures that reside in the axial portion of the accommodation zone (Figure 4.2). They appear to be curviplanar structures that rotate about a near vertical axis from an orientation more

synthetic to the intrabasin high clockwise to being more synthetic with the major range bounding structures on the west before terminating (Figure 4.2).

Line 4 is an ~14 km long line that images Elevenmile Canyon, southernmost Dixie Valley, and the southern Louderback Mountain piedmont (Figure 4.6 and Plate 7). Line 4 crosses or nearly crosses a large number of Pleistocene, Holocene, and historic ruptures that terminate into or are incised by the drainage fed by Elevenmile Canyon (Figure 4.6). It also crosses the northern termination of the historic Fairview Peak rupture right before it splits northward into the Gold King and Louderback mountains Faults (Figure 4.6).

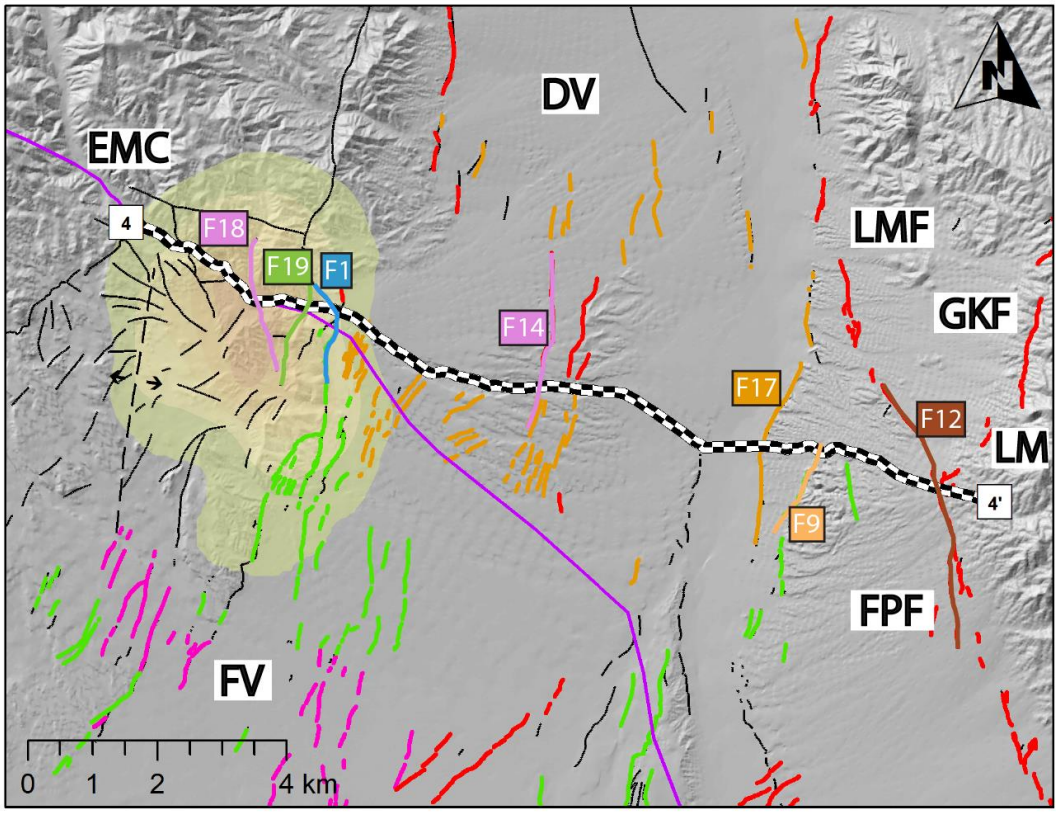

Figure 4.6. Detailed structure map of the southern seismic survey area that includes Lines 4 as a black and white line with labels. Red lines are faults with historic ruptures, orange are Pleistocene age, green are Holocene age, pink are Holocene/Quaternary age, black are Quaternary or older, and purple lines are interpreted as potential caldera boundaries. Elevenmile Canyon (EMC), Fairview Valley (FV), Louderback Mountains (LM), Dixie Valley (DV), Fairview Peak Fault (FPF), Gold King Fault (GKF), and the Louderback Mountains Fault (LMF). Colored squares correlate fault surface traces with near surface projections of fault interpretations from the seismic sections.

The seismic stratigraphy expressed in Line 4, compared to the northern survey area, suggests a thinning of SCC- related volcanic units to the south and an increasing presence of Mesozoic metamorphic rocks similar to those found south of Elevenmile Canyon in the study map area (Plate 12). Quaternary strata appear to be more thickly layered near the mouth of Elevenmile Canyon and more thinly layered in the central reach before becoming somewhat

incoherent as the section rises up the eastern piedmont (Plate 7). This phenomenon may be the result of a transition between alluvial versus lacustrine dominated depositional processes. The Overall Quaternary section appears to reach a maximum thickness of nearly 100 meters in southern Dixie Valley and thins to less than 10 meters at the edges (Plate 7). The underlying SCC volcanic section consist of tuffs associated with the younger Elevenmile Canyon Caldera. The reflection characteristics of the tuff are difficult to discern from the underlying basement unit on the west side of Line 4 where there appears to be an angular unconformity between the tuffs and what I interpret to be Mesozoic metamorphic basement (Plate 7). The tuffs appear to overly the basement with a fairly consistent thickness across the section and thin slightly at the edges. The small section of similar amplitude reflections in the Mesozoic section appear to fold and terminate against a low angle structure, possibly an old thrust associated with the La Plata Thrust (John and Silberling, 1994). The basement section further to the west is more clearly separated from the overlying tuffs as reflections become less continuous (Plate 7)

Historic fault ruptures at this latitude of the survey occurred as a subset of a large distribution of surface ruptures throughout Fairview and Dixie Valley (Figure 4.6). Ruptures are scattered across the alluvial fan surface of Elevenmile Canyon and not at the actual range front, which makes it difficult to identify a single rupture at the surface as the major range bounding fault. Based on my interpretation (Plate 7) there does appear to be a significant amount of offset on a steeply east-dipping structure near the mouth of Elevenmile Canyon (Figure 4.6) associated with Fault 1 (Figure 4.7 and Plate 7) that also defines the eastern edge of the relay ramp visible in Lines 1 and 2 (Figure 4.4) to the north. Faults 1 and 13-17 define a large graben,

its deepest part between Faults 13 and 15, and it appears to place the majority of vertical displacement at the Stillwater Range frontal fault (Figure 4.7 and Plate 7). The fault blocks within the graben appear to be affected by multiple periods of fault related deformation that possibly date back to the Mesozoic Luning-Fencemaker thrusts and also includes the 25-23 Ma period that resulted in nearly 100% extension of the SCC (Henry and John, 2013; John, 1995). This chronology of deformation results in a progression of lower angle structures being cross-cut by higher angle structures that define the modern graben structure (Figure 4.7 and Plate 7).

Structures further to the east include the southward continuation of Fault 9 that forms an apparent down to the west stair-stepping fault pattern with Fault 12 (Figure 4.7). These steeply west dipping structures form in the structural transition from down to the east Fairview Peak Fault displacement to right-oblique down to the west displacement of the Louderback Mountain and Gold King Faults (Figure 4.6). Despite the high fold of the line the reflection, coherency is lost at rather shallow depths and is likely the result of highly fractured and highly variable lithologic conditions that make interpretations of stratigraphy in this section highly speculative given the lack of reliable drilling data.

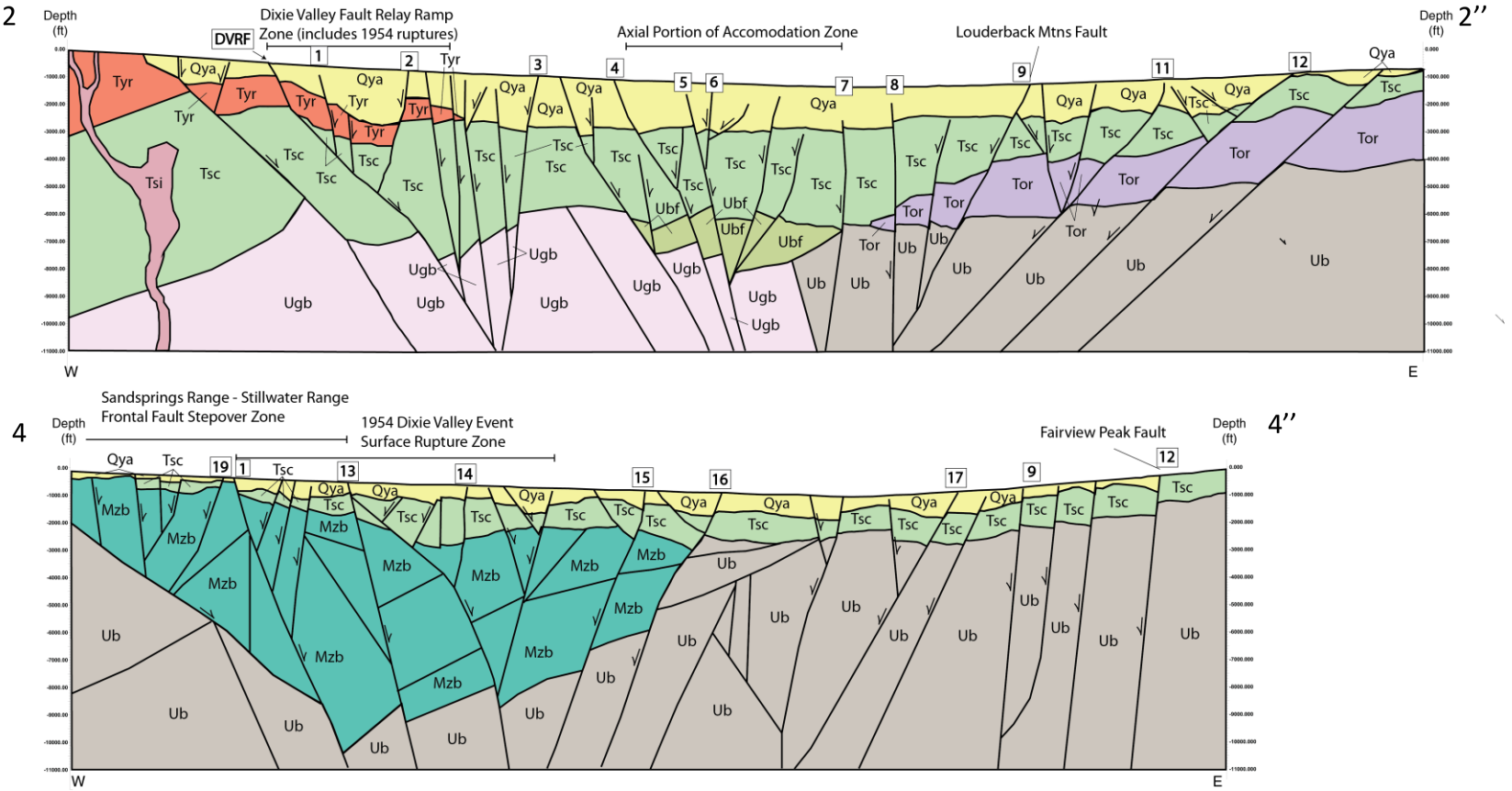

Figure 4.7. Geologic cross sections constructed along seismic lines 2-2’ (top) and 4-4’ (bottom) (Figure 4.1). Subsurface interpretations were based on geologic mapping and geophysical interpretations of gravity, magnetic, and 2D-seismic data of southern Dixie Valley and Elevenmile Canyon. The section 2-2’ identifies the axial portion of the accommodation zone at Pirouette Mountain where geothermal upwelling appears to be concentrated and the section 4-4’ identifies the eastern edge of the Sand Springs/Stillwater Range frontal fault stepover where it terminates into the Elevenmile Canyon coincident with the mapped heat loss of the Elevenmile Canyon geothermal system. Qya – Quaternary youngest alluvium, Tsi – Miocene silicic intrusion, Tyr – Miocene rhyolite, Tsc – Oligocene-Miocene volcanics of the Stillwater Caldera Complex, Tor - Oligocene rhyolite, Ugb – Undifferentiated granitic basement, Ub – Undifferentiated basement, Ubf – unidentified basin fill or altered rocks associtated with PM geothermal reservoir. Fault numbers correlate with seismic sections

4.2 Geologic Mapping

New mapping has provided an interesting modification to the structural history of the southern Stillwater Range as it relates to the most recent periods of extension. Previous research states that 70%-100% extension had occurred in the 29-25 Ma SCC at 25-24 Ma based on the fact that post caldera dike and dome emplacement related rocks are less tilted than the caldera related rocks (Hudson et al., 2000; John, 1992). Hudson et al. (2000) adds that pre-Neogene rocks of the southern Stillwater Range were coevally tilted with the Oligocene age caldera rocks in the hanging wall of a major detachment. Paleomagnetic data also suggests ~30˚ of counterclockwise vertical axis rotation related to either eastward expansion of the Walker Lane (Hudson et al., 2000) or the formation of the Humboldt Structural Belt. Henry (2013) cited unpublished apatite fission-track dating by Joseph Colgan and David John that suggests the southern Stillwater Range experienced an episode of major uplift on its eastern margin at 16-12 Ma. These data and interpretations suggest a period of relative tectonic quiescence or very minor extension in this region for a period starting ~24 Ma and ending around 16-12 Ma. This is why the focus of my mapping was to reevaluate the deposition and subsequent deformation of the perched Neogene basin and overlying volcanic rocks south of Elevenmile Canyon.

The Neogene basin developed at the base of a range that consisted of tilted Oligocene-Miocene caldera related and Pre-Neogene sequences south of Elevenmile Canyon. The Neogene basin, based on limited exposure, is filled by a lacustrine and fluvial sedimentary sequence that includes ash, tuffaceous siltstone, mudstone, sandstone, and a capping conglomerate. The sequence is also faulted, folded, and tilted to the east and west up to 56˚.

Overlying the basin sediments is a volcanic sequence of basalt, basaltic andesite, and andesite lavas. Additional volcanic exposures are located south and west of La Plata Canyon and extend to the eastern edge of the Carson Sink, the northern edge of the Sand Springs Range, and beyond. They consist mainly of volcanic flows, primarily basalts, and shallow intrusive rocks (Figure 4.8).

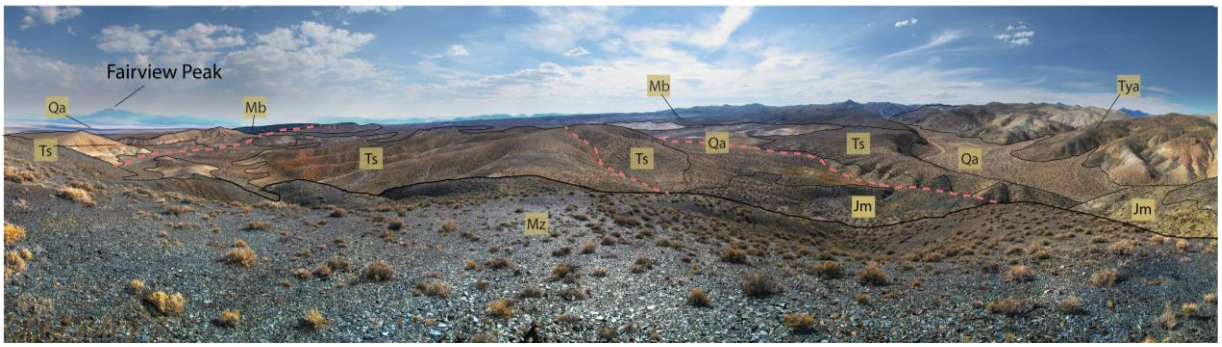

Figure 4.8. Annotated panoramic view looking south from the southern rim of Elevenmile Canyon onto the field mapping area of this study. Stratigraphy outlined in black and faults are dashed in red. Unit abbreviations are from mapping (Plates 12 and 13), Qa (Quaternary Alluvium), Mb (Miocene Basalt), Tya (Neogene Andesite), Ts (Neogene Sediments), Mz (Mesozoic Metamorphic Rocks), Jm (Jurassic Marble).

The geologic data provides insight on the timing and direction of extension for the broader study area by translating depositional relationships and dip of measured strata tilted by extensional faulting into least principal horizontal paleostress directions. Current and previous mapping (John and Silberling, 1994) indicates a pronounced angular unconformity between the Tuff of Elevenmile Canyon and the Neogene basin sediments that suggests a significant amount of extension prior to deposition that resulted in the tuff unit being steeply titled to the east-southeast (Figure 4.9).

The Neogene basin sediment upper contact with the younger volcanic sequence appears to have only a minor angular unconformity, if any, which suggests the two units were deposited in a common period of limited extension in the region (Figure 4.9). After deposition of the Neogene sediments and overlying volcanic rocks the adjacent units were faulted and tilted in two distinct periods of extension. The initial period resulted in the gentle tilting of the volcanic rocks and Neogene basin sediments 10˚ (mean dip) to as much as 26˚ to the southwest (Figure 4.9). This episode of moderate tilting does not provide strong evidence for any broad tectonic activity.

Further mapping analysis suggests the ensuing period of deformation, ~14 Ma to present, resulted in the formation of a major accommodation zone between the northern extension of the Sand Springs Range frontal fault and the Stillwater Range frontal fault. Within the accommodation zone faults dipping toward the east and west form small horst and graben features, complex fault intersections, and many terminations. The northern extent of the accommodation is bounded by the transversely oriented Elevenmile Canyon and the adjacent pre-Paleogene and Oligocene caldera rocks act as a barrier which faults either terminate into or deflect away from toward the Stillwater Range frontal fault (Figure 4.6).

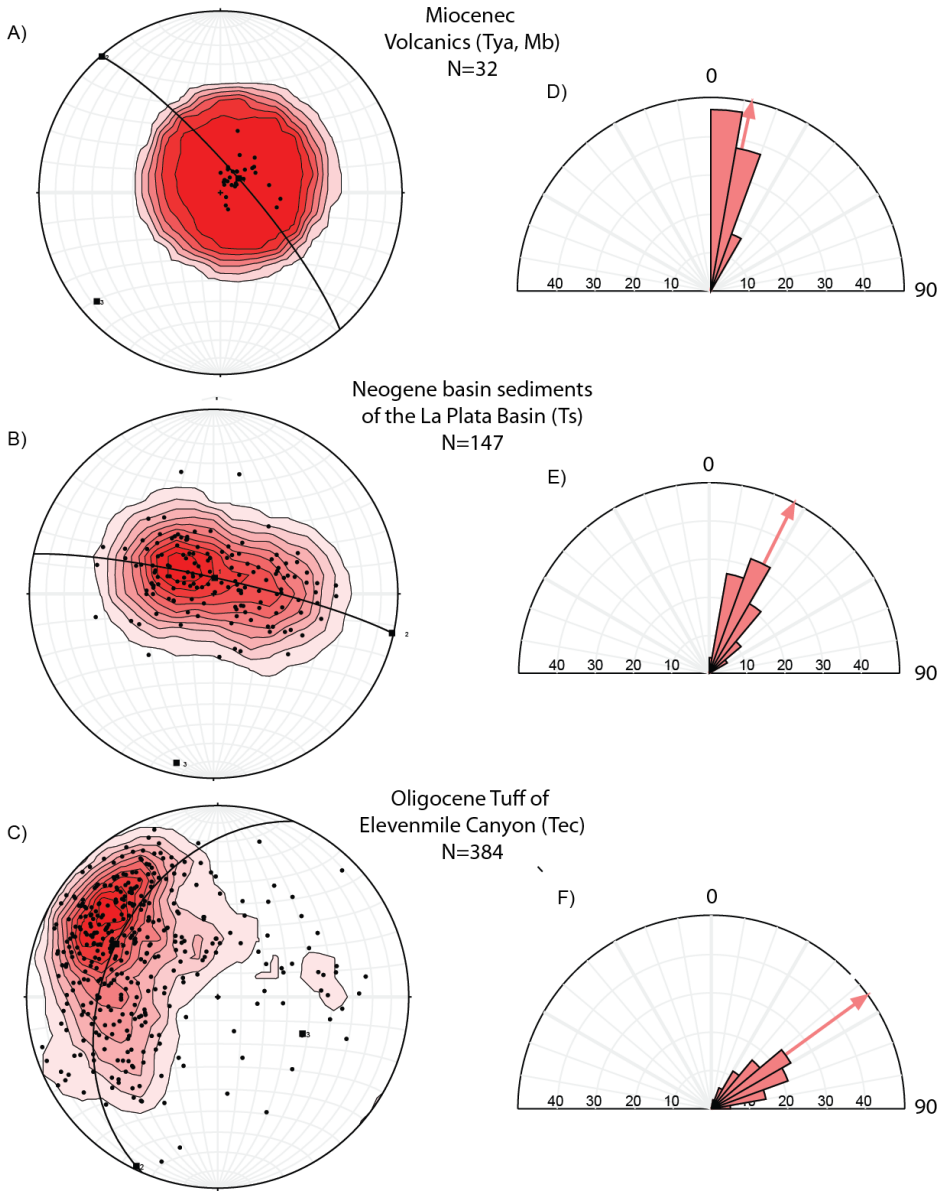

Figure 4.9. Lower hemisphere equal–area stereographic projection and comparison of measured bedding and layering, respectively, for sedimentary and volcanic units of the southern Stillwater Range stratigraphy. Left column shows poles to bedding or layering. Right column displays respective dip values as rose diagrams in 10˚ increments from horizontal (0˚) to vertical (90˚) and bin length value plotted as percentage of total. (A) Poles to basal contact of volcanic rocks (Tya and Mb) measured using three point problems; (B) Poles to bedding of Neogene basin sediments (Ts); (C) Poles to compaction foliation in 25.1 Ma tuff of Elevenmile Canyon (Tec). Kamb contouring applied to all datasets with 2σ intervals and a 3σ significance level. Data points are shown as black dots and conical best fit great circle based on a Bingham Analysis performed in Stereonet 9.

Aside from the initial southwest tilting of the volcanic rocks and the underlying Neogene basin sediments, geologic data from mapping seems to fit with major extension in central Nevada oriented 280˚-300˚, 17-16 Ma to present (Figure 4.9B), with minor evidence for reactivation of structures formed during collision or by lateral flow and/or gravitational collapse (Colgan, 2013; Colgan et al., 2008; Fosdick and Colgan, 2008; Zoback et al., 1981).

4.3 Timing of deformation

As previously discussed, the ~100% extension of the SCC occurred between 24 Ma and 25 Ma based on the age of untilted dikes that intrude the SCC. As previously stated (Table 1), the sample from the lowest stratigraphic unit in the volcanic sequence, LP-7, did not produce compatible ages between the groundmass and plagioclase analysis. We therefore accept the weighted mean plateau age of 16.14 Ma as a maximum age for the volcanic sequence and the age of the next oldest sample in the andesite stratigraphic sequence, LP-4, as a minimum age for LP-7 of 14.92 Ma. This information along with the unconformable nature of the depositional relationship between the Neogene basin sediments (Ts) and the Tuff of Elevenmile Canyon (Tec) (Figure 4.9 and Plate 7) suggests that from 25-24 Ma to 16-15 Ma the southern Stillwater range was being very slowly exhumed and forming a volcaniclastic-sourced lacustrine basin that experienced only slight, if any, tilting prior to the impending deposition of flows related to widespread volcanism.

It should be noted that basin and range extension is posited to have initiated in the East Range to the north at ~17-15 Ma (Fosdick and Colgan, 2008). The ~15 Ma period of volcanism buried the lacustrine basin for a period that presumably lasted until at least 14.34 Ma (LP-12,

Table 1). Similar data from the Tobin Range to the north for a basalt flow with a 14.11 Ma $^{40}Ar/^{39}Ar$ age interbedded with a similar lacustrine basin formation suggests that this period of volcanism may have lasted until ~14 Ma (Gonsior and Dilles, 2008). This assumption is also supported by a ~14 Ma, north-striking dike swarm in the Bunejug Mountains and Rainbow Mountain (Figure 1.5) (Bell et al., 2009; Hinz, 2011; Hinz et al., 2014) and similar undated basaltic andesite dikes of similar orientation (Plate 12) that cross cut the youngest andesite flow (LP-12, 14.34 Ma) (Figure 4.10). North-south oriented dike swarm activity may represent the last of this period of volcanism as it overlapped with the onset of east-west directed extension of the Basin and Range in the southern Stillwater Range.

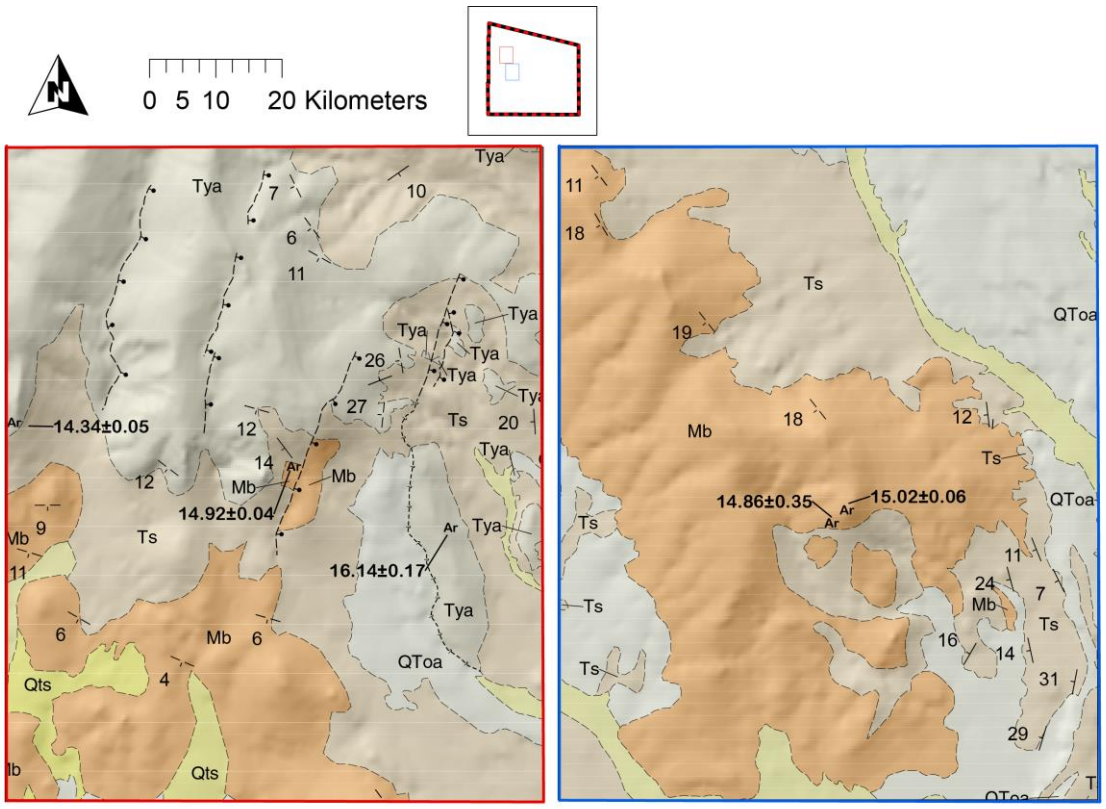

Figure 4.10. Detailed inset geologic maps with Ar sample locations, demonstrating the structural and stratigraphic relationship between Neogene sediment (Ts) and volcanic rocks (Tya, Mb). Similar orientation and degree of tilting to the southwest of units is observable, including where secondary deformation has occurred along north-northeast trending structures of the most recent period of extension. Ar geochronology sample locations with ages also support tilting to the southwest.

When compared with Basin and Range extension onset at ~15-12 Ma in the Wassuk Range (Stockli et al., 2002) the data creates an expression of extension migrating southward from the East Range, through the Stillwater Range and into the Wassuk Range just prior to initiation of dextral shear in the north-central Walker Lane beginning ~9-10 Ma (Faulds and Henry, 2008) to the southwest of the Stillwater Range. Although the orientation of the extensional structural fabric in the Dixie/Fairview Valley area are distinctly different in style then the dextral shear and

wrench faulting of the nearby Walker Lane (Figure 4.11) it is all consistent with east-northeast directed extension.

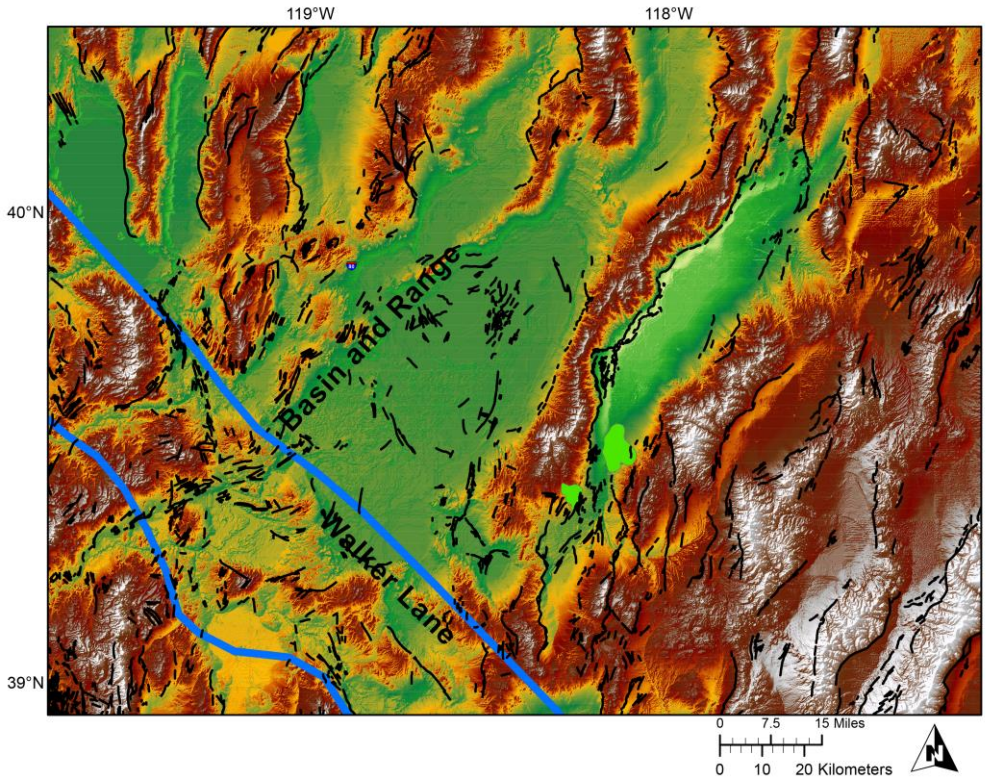

Figure 4.11. DEM base with Quaternary faults as black lines Walker Lane outlined in blue, and geothermal systems of PM and EMC shaded in bright green. The contrast between northwest directed shear in the Walker Lane and northwest directed extension in the Basin Range is clear in the orientation of not only Quaternary structures, but also in the orientation of ranges.

4.4 Geometry of Faulting

As previously discussed, both the PM and EMC geothermal systems reside in an area of prominent intermeshing Quaternary faulting along major northerly striking frontal fault systems and diffuse dextral shear zones. The study area cannot be defined by a single through-going fault or individual range front fault system, but dozens of smaller faults are distributed between

major range bounding faults. The Sand Springs and Stillwater Ranges frontal faults and the Fairview Peak fault and associated splays can all be observed to cross cut and/or terminate against late Cenozoic Structural patterns of the western Basin and Range (Bell et al., 2004), such as the SCC boundary at Elevenmile Canyon (Figure 4.6).

Faults range in orientation from due north to northeast with predominantly normal slip and a small component of right-oblique slip. Dextral shear strain is translated from the Walker Lane Belt in the form of local right-normal-oblique slip earthquakes like the Fairview Peak event. The hypocenter occurred in the northern extent of the diffuse strain transition zone between northwest directed dextral shear of the Walker Lane Belt and north-northeast striking normal faults of the central Basin and Range (Figure 1.4) (Bell et al., 2004; Caskey et al., 1996; Caskey et al., 2004; Slemmons, 1957).

The PM geothermal system is located in a ~6 km wide accommodation zone between two northerly striking, east- and west-dipping historically active fault zones that include ruptures from the 1954 Fairview Peak and Dixie Valley Earthquakes (Figure 4.2). This includes the northern termination of the Louderback Mountains, Gold King, and Westgate faults that make up the west dipping splays of the northern termination of the east-dipping, right-oblique Fairview Peak fault on the east and southward termination of the east dipping Dixie Valley Fault on the west (Figure 2.5). The west dipping splays of the Fairview Peak fault, such as the Louderback Mountains fault, bound major east-tilted blocks that are being actively dislocated from the Clan Alpine Mountains (Figure 4.7).

Based on structural interpretations of the historic rupture patterns, mapped Neogene-Quaternary faults, and gravity and magnetic data we were able to characterize the structural setting, in map view, in terms of specific geometry and geothermal activity. Geothermal activity at PM appears to occur where the basinward termination of the west-dipping right-oblique Louderback Mountains fault that bounds an oblique anticlinal accommodation zone on the east, steps to the west and translates motion to a series of right-stepping, east-dipping normal fault strands that eventually intermesh and join the Stillwater Range frontal fault. Extensive shallow drilling and heat flow data suggest that the geothermal activity is most intense in what could be interpreted as the north trending axial portion of this accommodation zone, which is orthogonally oriented to the regional direction of extension (Figure 4.2 and 4.7).

The axial portion of the accommodation zone, where heat flow is most intense, initiates where the oblique anticlinal accommodation zone dips northeast toward the southern Dixie Valley basin deep (Figure 4.2). This right-stepping pattern of down-to-the-east faulting of closely spaced, steeply dipping fault strands and intersections of east- and west-dipping faults is spatially coincident with shallow geothermal outflow (Figure 4.7) The axial portion of the accommodation zone can also be characterized, in part, as a caldera boundary between the Poco Canyon and Elevenmile Canyon Calderas (Figure 4.2). Evidence of concentrated heat flow in the axial portion of the accommodation zone as opposed to the anticlinal zone is most apparent in well 66-16 (Figure 4.2), a ~2,000 m well drilled into the central part of a shallow thermal anomaly identified by the Hunt Corporation. The shallow thermal environment of 66-16 was ~90˚ C, similar to previous drilling results; however, the deep portion of the well failed

to encounter fluids of significantly higher temperatures. The 66-16 well was drilled directly into the axis of the oblique anticlinal accommodation zone and completely missed the down-dip projection of east-dipping faults that appear to terminate into the accommodation zone and are the preferred orientation for permeability and translation of geothermal fluids near to the surface. If we assume a ~60˚ dipping Stillwater Range frontal fault (Figure 4.4) and we assume, based on seismic data, the concealed basinward strands of the east-dipping fault zone dip more steeply ~70˚-80˚ (Figure 4.3 and 4.7) then we could anticipate them intersecting at 3 to 4 km depth. These structurally favorable intersections would most likely yield enhanced permeability and provide detailed information on the behavior of the larger geothermal system at play.

The EMC geothermal system is located in a 5 km wide major right step from the Sand Springs Range frontal fault system to that of the southern Stillwater Range (Figure 4.6 and 4.7). Like many major stepovers in the Great Basin that host geothermal systems it is characterized by a complex network of faults both antithetic and synthetic to the frontal fault shear boundaries. The step over zone extends from the Oligocene SCC margin at Elevenmile Canyon ~5 km south and includes numerous Quaternary scarps and historic ruptures. However, in the area of highest heat flow Quaternary scarps are absent and mapped structures were inferred based on geomorphology, geologic relations and geophysical interpretations (Figure 4.6).

The structural pattern in the stepover demonstrates a clear relationship with the Oligocene SCC margin as numerous faults shift to a north-easterly orientation and antithetic structures are present where strain is deflected around this major structural boundary. Several north-northeast trending faults displace Neogene basin sediments and Oligocene volcanic rocks

against Mesozoic basement in a small, irregular graben in the frontal fault step over zone (Figure 4.7). The highest heat flow values are located near the eastern margin of this graben structure and both bounding faults down-dip projection also center under this prospective area. The west-dipping fault bounding the eastern margin cuts the actual caldera margin (Figure 4.6) and because the orientation is at a high-angle to the least principal stress there is strong evidence to support these two features playing a role as critical pathways in the translation of geothermal fluids near to the surface.

4.5 Slip and Dilation Tendency Analysis

Kinematic analysis of fault slip data was initially conducted on data collected from the geologic mapping area to compare orientations of principal strain and stress axes with similar data from the larger study area. Slickenlines and offset of layering were the primary kinematic indicators used to determine slip sense on 31 fault surfaces. The data show that the La Plata accommodation zone is characterized by moderate to steeply dipping normal to right-oblique slip faults with a minor sub-population of steeply dipping dextral/dextral-oblique faults (Figure 4.12a). The mapped extent for many of these faults required them to be approximated due to limited and poor exposure.

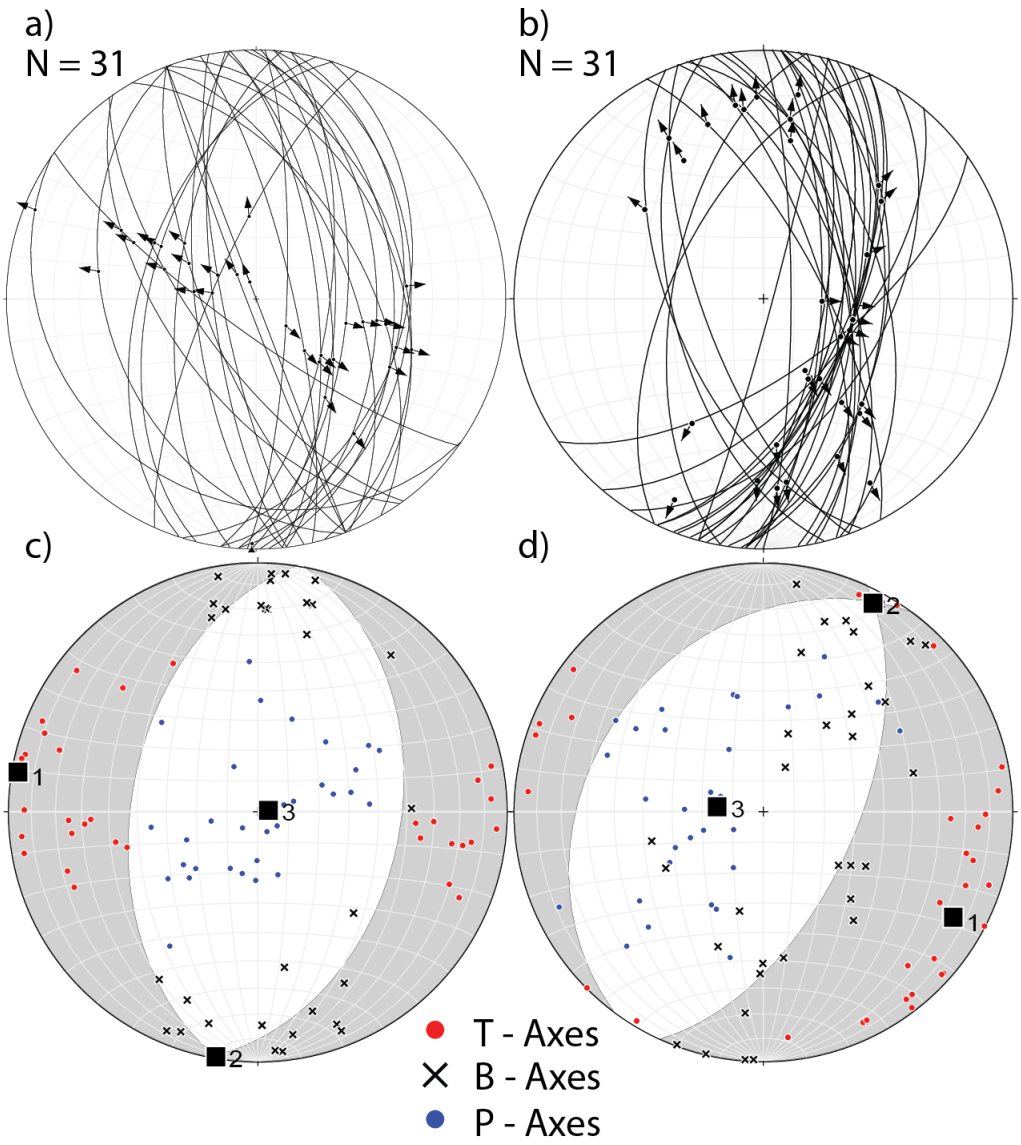

Mean Vector

T = 115.9/14.3 = σ_1 = ■3
B = 189.9/00.8 = σ_2 = ■2
P = 279.4/75.2 = σ_3 = ■1

Mean Vector

T = 279.9/02.9 = σ_1 = ■3
B = 024.8/04.0 = σ_2 = ■2
P = 085.1/87.0 = σ_3 = ■1

Figure 4.12. Kinematic fault measurements with hanging wall slip direction from a) the La Plata Basin mapping area and b) regional historic rupture surfaces summations and geodetic data associated with the 1954 Fairview Peak-Dixie Valley and Rainbow Mountain rupture sequences (Caskey and Wesnousky, 1997; Caskey et al., 1996; Caskey et al., 2004). Principal strain axes for each dataset, c) La Plata Basin and d) regional, calculated using the P &T dihedral method and moment tensor overlain using Stereonet 9 (Allmendinger et al., 2011). Analysis supports similar modes of extension with a slight clockwise rotation from older deformation preserved in La Plata Basin to the historic earthquakes of the locale.

The regional dataset includes fault kinematic data from studies related to the historic Fairview Peak, Dixie Valley, and Rainbow Mountain earthquakes (Caskey and Wesnousky, 1997; Caskey et al., 1996; Caskey et al., 2004) and inverted coseismic geodetic data (Hodgkinson et al., 1996). These data form a similar pattern of extensional faulting with a minor clockwise adjustment to the horizontal stress orientations and a slight increase in the overall dextral component (Figure 4.12b). The majority of these measurements represent the average strike, dip, and rake from multiple measurements taken along individual segments of surface ruptures that occurred in one of the previously mentioned historic events.

Principal axes of extension and shortening were then quantitatively determined by constructing lower hemisphere, equal area stereographic projections of fault-slip kinematics in the Stereonet 9 program {Allmendinger, 2014). The kinematic axes share a common plane with slip direction and the fault poles were determined by bisecting the orthogonal nodal planes of the projected fault surface. The kinematic axes, where (P)ressure refers to shortening and (T)ension refers to extension, form 45˚ angles with both the pole to the fault and the slip direction. The P- and T-axes represent the analytical equivalent to principal axes of the incremental strain tensor for the region represented by the dataset (Figure 4.12b) (Marrett and Allmendinger, 1990). Stereonet 9 also calculates a linked Bingham distribution analysis that produces a best fit fault plane solution for all kinematic data (Figure 4.12).

For the La Plata dataset the calculated eigenvectors for the symmetric portion of the displacement gradient tensor or mean principal stresses for the best fit fault plane solution are $\sigma_1 = 85^\circ/87^\circ$, $\sigma_2 = 190^\circ/1^\circ$, $\sigma_3 = 279^\circ/3^\circ$ (Figure 4.12a). The principal stresses for the regional

dataset are σ_1 = 279˚/75˚, σ_2 = 25˚/4˚, σ_3 = 116˚/14˚ (Figure 4.12b). The computed orientations agree nicely with west-northwest directed extension in the Great Basin that began 17-16 Ma. However, based on the new geochronology and previously published data the La Plata dataset is more closely related to a period of extension that lasted from ~14 Ma until about 10 Ma as a period of more variable extension, 280^o-300^o as a result of increased distribution of dextral motion prior to the formation of the Walker Lane (Dickinson, 2006, 2013; Fosdick and Colgan, 2008; McQuarrie and Oskin, 2010; McQuarrie and Wernicke, 2005). The modern dataset (Figure 4.12b) suggests an orientation for extension, based on the orientation of the least principal stress ($\sigma_{3)}$ of 296˚ (116˚)), that is more compatible with orientations post 10 Ma, 290^o -300^o, as horizontal stresses become more organized and less widely distributed with the formation of the Walker Lane(Colgan, 2013; McQuarrie and Oskin, 2010; McQuarrie and Wernicke, 2005).

Slip and dilation tendency analysis was performed on fault traces from the study area using the program 3DStress developed by Southwest Research Institute. The ratio of shear stress to normal stress on a given surface is the slip tendency and the dilation tendency is defined by the stress acting normal to a given surface (Ferrill and Morris, 2003; Morris et al., 1996). The individual slip and dilation tendency values are unitless and range from 0 to 1. A value of 1 is given to faults at the ideal orientation for slip or dilation under ambient stress conditions; 0 value indicates no potential for slip or dilation. The results of this initial analysis assume optimal dip for each fault because dip is largely unknown for many of the faults and it allows for the maximum potential slip and dilation tendency to be observed. The resulting analysis can also be displayed as the summation of slip and dilation tendency, ranging from 0 to 2, which provides a

proxy for optimal fluid flow potential in terms of along-fault and fault-to-fault variation in slip and dilation tendency.

Stress orientations, as previously mentioned, for the study area were approximated from previously cited data and the stress magnitudes were also assessed from regional published data on the topic (Barton et al., 1997; Blake, 2013; Blake and Davatzes, 2012; Davatzes and Hickman, 2010; Hickman et al., 2000; Hickman and Davatzes, 2010). Stress magnitude ratios consistent with a dominant normal stress regime where the vertical stress (S_v) is greater than the maximum horizontal stress (S_{hmax}), and S_{hmax} is larger than minimum horizontal stress (S_{hmin}) were applied to the study area. The actual magnitudes applied are S_v= 63 MPa, S_{hmax}= 55 MPa, S_{hmin}= 31 MPa and produce ratios of S_{hmin}/ S_{hmax} = 0.56 and S_{hmin}/ S_v = 0.49. These stress magnitude values are consistent with ratios and values reported from hydraulic fracturing well studies at the Dixie Valley power plant (Hickman et al., 2000) and with similar studies at Yucca Mountain (Stock et al., 1985). Under these stress conditions, north-northeast striking, 65˚-70˚ dipping fault segments have the highest tendency to slip and north-northeast striking, steeply dipping (>70˚) fault segments have the highest tendency to dilate. The slip tendency results were then compared to results derived from two other stress tensors from regional focal mechanism data for central Nevada (Doser, 1986; Zoback et al., 1981; Zoback and Zoback, 1980) (Figure 4.13). Each new stress tensor was derived from the same dataset, but since the focal mechanism data indicated both normal and strike-slip faulting the dataset was inverted once with σ_1 vertical (Figure 4.13a) and once with σ_1 horizontal (Figure 4.13b) so that both conditions could be examined. Given the proximity to the Walker Lane boundary the study area

has likely been and will likely continue to be affected by both normal and strike slip faulting stress regimes.

The slip tendency results for each scenario can be viewed in Figure 4.13, along with the given stress tensor and rose diagram. The rose diagrams are color coded according to slip tendency and group fault trends in 5˚ bins. Each rose diagram represents the same fault population under each unique stress regime and demonstrates that in the initial stress field the dominant fault trend has the greater slip tendency (4.13c) compared to the regional focal mechanism derived stress fields (4.13a and 4.13b) where it appears the greatest slip tendency occurs just outside the dominant fault trend. Given the inverted stress tensor's demonstration of greater consistency with the dominant fault trend and the modern extensional tectonic setting it is used to characterize the slip and dilation tendency for faults of interest to this study.

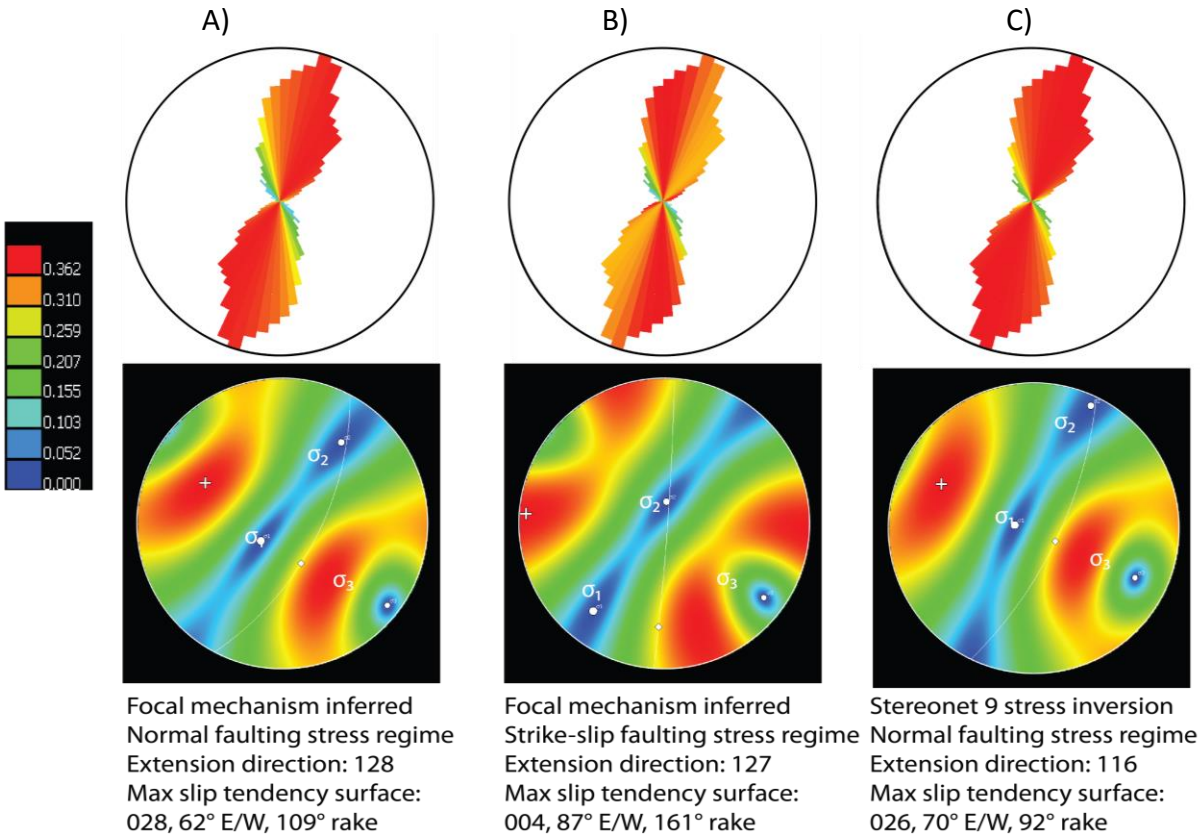

Figure 4.13. Structural analysis completed in 3DStress, color coded for slip tendency. Warm colors indicate higher tendencies. Results in each column are based on individual potential focal mechanism solutions, as discussed in text. Rose diagrams represent populations of fault orientations placed into 5^{o} bins. Columns A and B are based on the same compilation of Central Nevada earthquake data (Doser, 1986; Zoback et al., 1981; Zoback and Zoback, 1980), however A was analyzed as a normal faulting regime and B as a strike-slip regime. Column C utilized the focal mechanism inversion established in Figure 4.9 d) and demonstrates the a best fit for all active faults identified in the corresponding map in column C).

5. Discussion

5.1 Timing of Deformation

Analysis of geochronologic, structural, and stratigraphic data from this study and others reveal a sequence of deposition and deformation in which sedimentary and volcanic strata of the La Plata Basin sequence (Ts, Tya, and Mb) were deposited in a period of relative tectonic quiescence, ~24-14 Ma. The sequence was initially tilted ~15˚ to the west-southwest following deposition of the ~14-16 Ma volcanic sequence. The ensuing period of deformation tilted the sequence as much as 40^{o} to the east and west along north-northeast trending faults with motion that ranged from dominant normal to infrequent dextral (Figure 4.10). The data suggests that major Basin and Range extension began ~14 Ma for this locale and supports similar estimations of extension in this part of the Great Basin as reported in previous studies (Colgan and Henry, 2009; Colgan et al., 2008; Henry and Perkins, 2001; Rhodes, 2011; Trexler et al., 2004). This refinement of local geochronology creates a timeline of deformation that rationalizes discrete folding of the La Plata Basin sedimentary sequence as axial planar deformation perpendicular to a transtensional shear boundary and places it into a period of deformation that is more clearly understood and well known than the period prior to onset of Basin and Range extension in central Nevada.

5.2 3D Structural Model

Fault plane interpretations for the Pirouette Mountain and Elevenmile Canyon geothermal systems were generated through an iterative modeling and interpretation process that utilized geologic and geophysical data (geologic mapping, seismic reflection data, gravity, and

magnetics). Fault planes considered Quaternary in age, critical to fluid flow, and distinguishable across two or more seismic lines were imported into Petrel and constructed using the convex hull gridding tool for 3D visualization (Figure 5.1). The grid files were then imported to 3DStress for analysis of slip and dilation tendency by applying the previously described best fit stress tensor solution in Figure 4.13. This analysis resulted in a refined perspective on fault-controlled fluid flow supporting the geothermal systems based on stress conditions and fault geometry. Each gridded fault represents a buffered zone of increased fracture density on a micro- and macroscopic level that corresponds to a peak in potential permeability. This permeability is further enhanced by fault geometries that favor slip and dilation and concentrations of fault intersections and terminations.

We generally observe that faults identified for this analysis and specifically those associated with the Pirouette Mountain and Elevenmile Canyon geothermal systems are steeply east or west dipping structures (>60˚). The structures also appear to be planar to slightly curviplanar and maintain a steep dip angle to depths beyond 3,000 meters (10,000 ft). The surface rupture patterns demonstrate a high density of fault terminations and, however significantly fewer fault intersections.

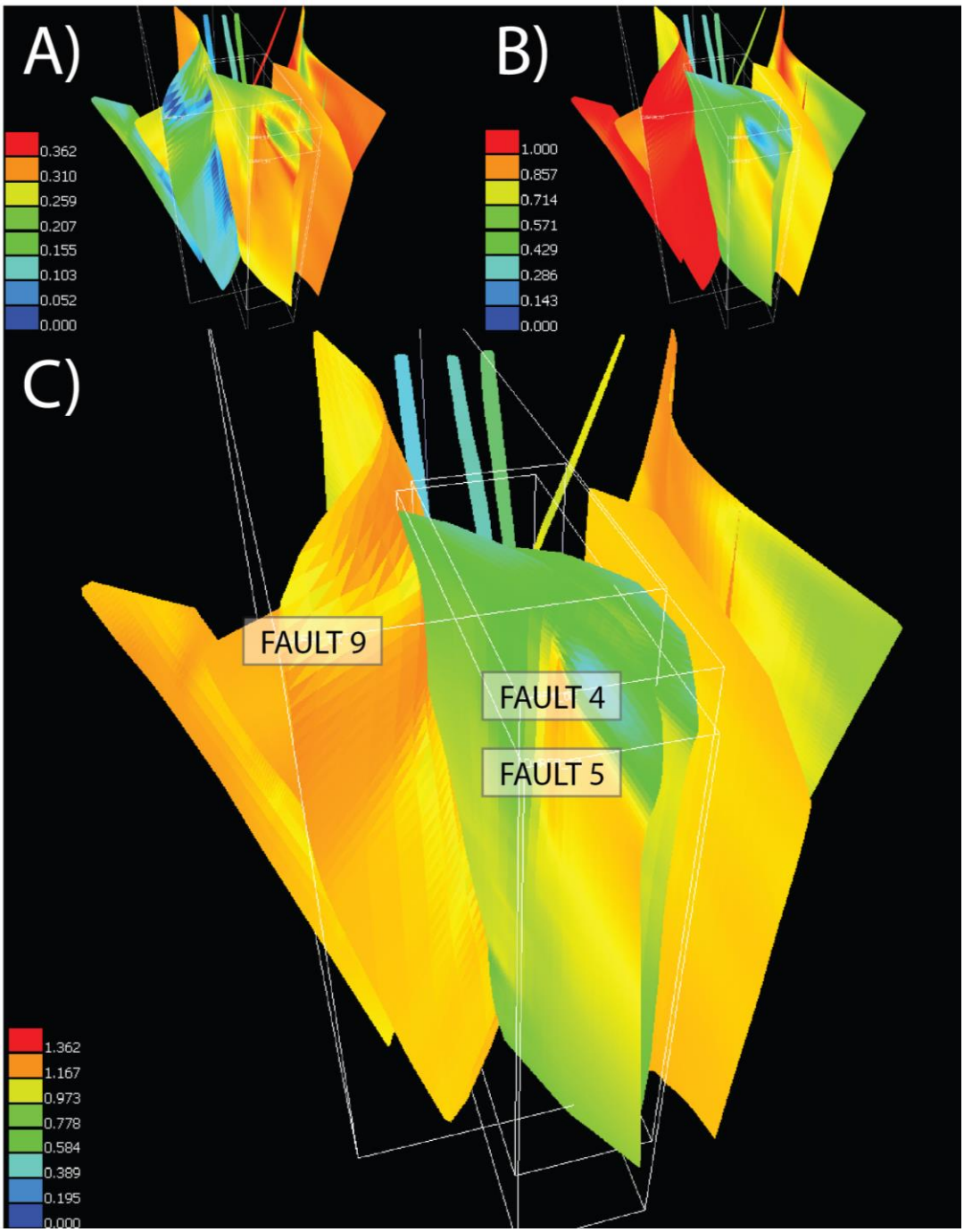

Figure 5.1. Planes interpreted as continuous between 2D-seismic lines evaluated in 3DStress for slip and dilation tendency at depth. View is looking southwest onto the Pirouette Mountain geothermal system. The right most plane defines the Stillwater frontal fault. Warmer colors correlate with increased slip and/or dilation tendency. A) is slip tendency, B) is dilation tendency, and C) is slip plus dilation tendency. Fault curvature suggests increasing slip and dilation tendency with depth. From top of section to base of section is 11,000 feet.

At Pirouette Mountain the fault geometries, albeit inferred from geophysical data, suggest a much higher incidence of fault intersections than surface patterns would suggest. This occurs across a zone of active sedimentation and spatially distinct concentrations of very recent local extension that varies along strike in orientation and sense of offset. The intersections appear to occur most commonly with faults of favorable orientation terminating against those of less favorable orientation, specifically the east to northeast dipping structure that bounds the intrabasin high (Figure 5.2). If the geometry is accurate, then based on the analysis the structures most likely to be associated with upwelling geothermal fluids would be steeply dipping north to northeast trending structures in the axial portion of the accommodation zone because they have the greatest tendency for slip and dilation and are located proximal to the highest values of measured heat flow. The area near the intersection of Faults 4, 5, and 9 are of particular interest due to their proximity to elevated heat flow measurements. Fault 9 represents some of the lowest slip tendency values and some of the highest dilation values and Faults 4 and 5 have intermediate slip tendency values and some of the lowest dilation values observed in the structural framework (Figure 5.1). As a result, the combined slip and dilation tendency analysis indicates that Faults 4 and 5 have the lowest combined values and Fault 9 has intermediate to high values with an understanding the results for Fault 9 are weighted more heavily toward a tendency to dilate.

These results support the observation that faults synthetic to the oblique anticlinal accommodation zone are not optimally oriented for slip or dilation (Figure 5.2) and act as a barrier to fluid flow. As a result, upwelling geothermal fluids associated with the Pirouette

Mountain Geothermal System do not migrate across this barrier in significant volumes. The presence of high heat flow near the surface supported by the higher slip and dilation tendency within the geothermal system where structures associated with the accommodation zone rotate to a more favorable orientation generate zones of high dilational fracture density that promotes circulation of shallow geothermal fluids (Figure 5.2).

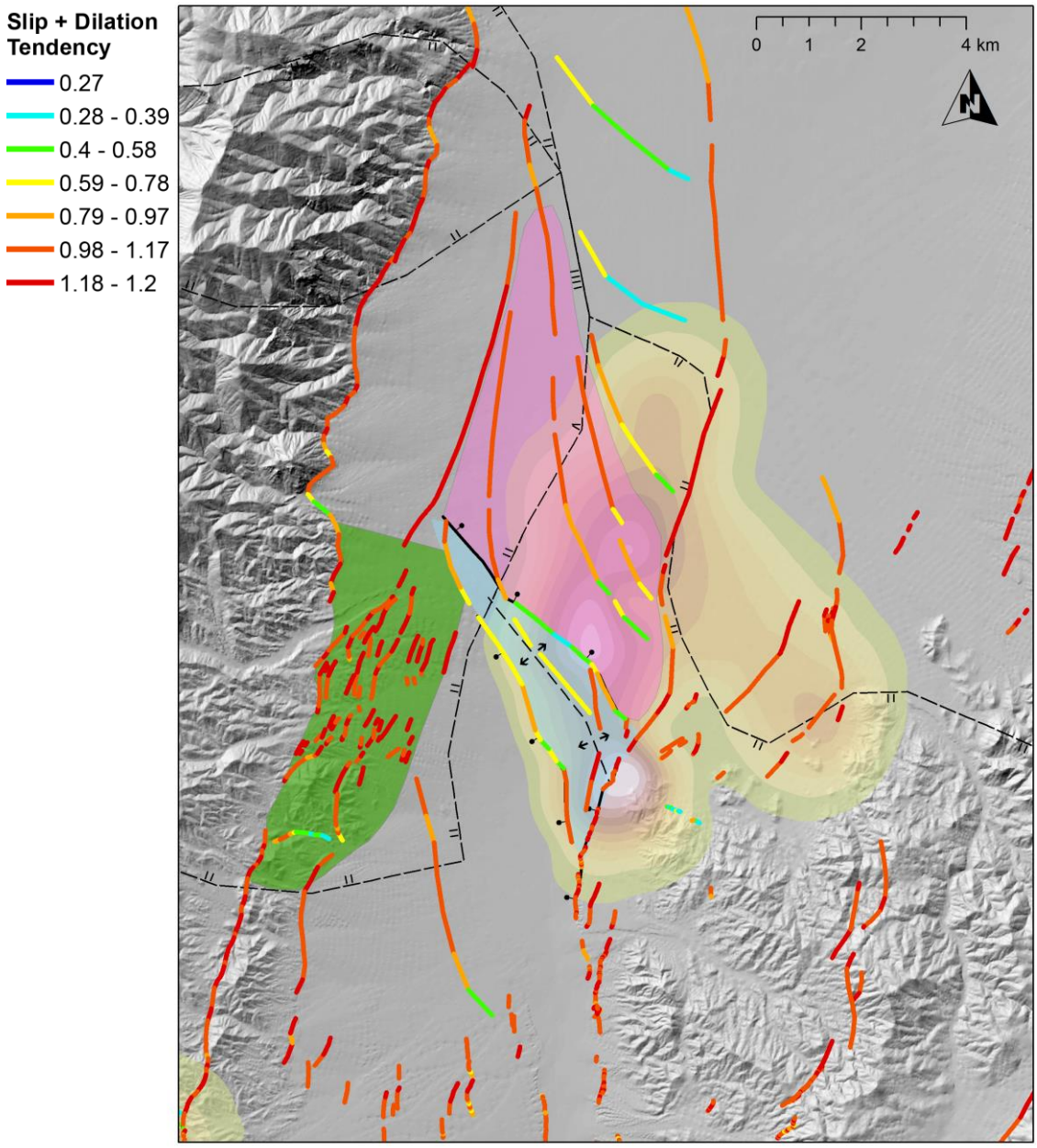

Figure 5.2. Map of structural features related to the PM geothermal system on a DEM base. Faults are colored based on slip and dilation tendency, warmer colors represent increasing tendency and cooler colors represent decreasing tendency. Shaded areas represent critical structural zones, Stillwater Range frontal fault relay ramp in green, oblique anticlinal accommodation zone in light blue, and axial portion of accommodation zone in pink. Fault balls indicate hanging wall of faults considered critical to understanding the fluid flow in the accommodation zone. Caldera margin is the dashed black line with hachures indicating caldera interior. Anticlinal fold axis defined by dashed line with arrows pointing in down-dip direction.

Compared to Pirouette Mountain, the Elevenmile Canyon geothermal system lacks a similar volume of data for the proposed 3D structural geometry given that there is only one 2D-seismic line that crosses the study area. The surface rupture pattern and complimentary surface geophysics provide the basis for our extrapolation of 2D-seismic fault interpretations into the 3D structural framework (Figure 5.1). The resulting framework suggests that the geothermal system is hosted where the eastern margin of the Sand Springs-Stillwater accommodation zone terminates into the Elevenmile Canyon caldera margin (Figure 5.3). The interpreted Stillwater Range frontal fault, Fault 1 (Plate 7) appears to have the largest amount of offset and the most favorable orientation for slip and dilation. However, the measured heat flow data suggests that the geothermal systems near surface manifestation occur in the footwall of this major range bounding structure. This suggests that the geothermal system either completely resides in the footwall or abandons the frontal fault as the primary conduit at a shallow depth and migrates through open fractures or a stratigraphic boundary into the footwall. In the case of the former it is possible that the geothermal system is hosted within the caldera margin that likely dips steeply to the south and rises along preferentially oriented structures and then flows along the natural hydrologic gradient. The latter might be due to the large accumulation of sediments in the hanging wall that could potentially be masking heat flow in the hanging wall and promoting migration into the footwall due to strong contrasts in permeability and low thermal diffusivity in the deep hanging wall graben. Regardless of which is correct both scenarios involve the caldera margin as a major conduit for fluid translation from depth.

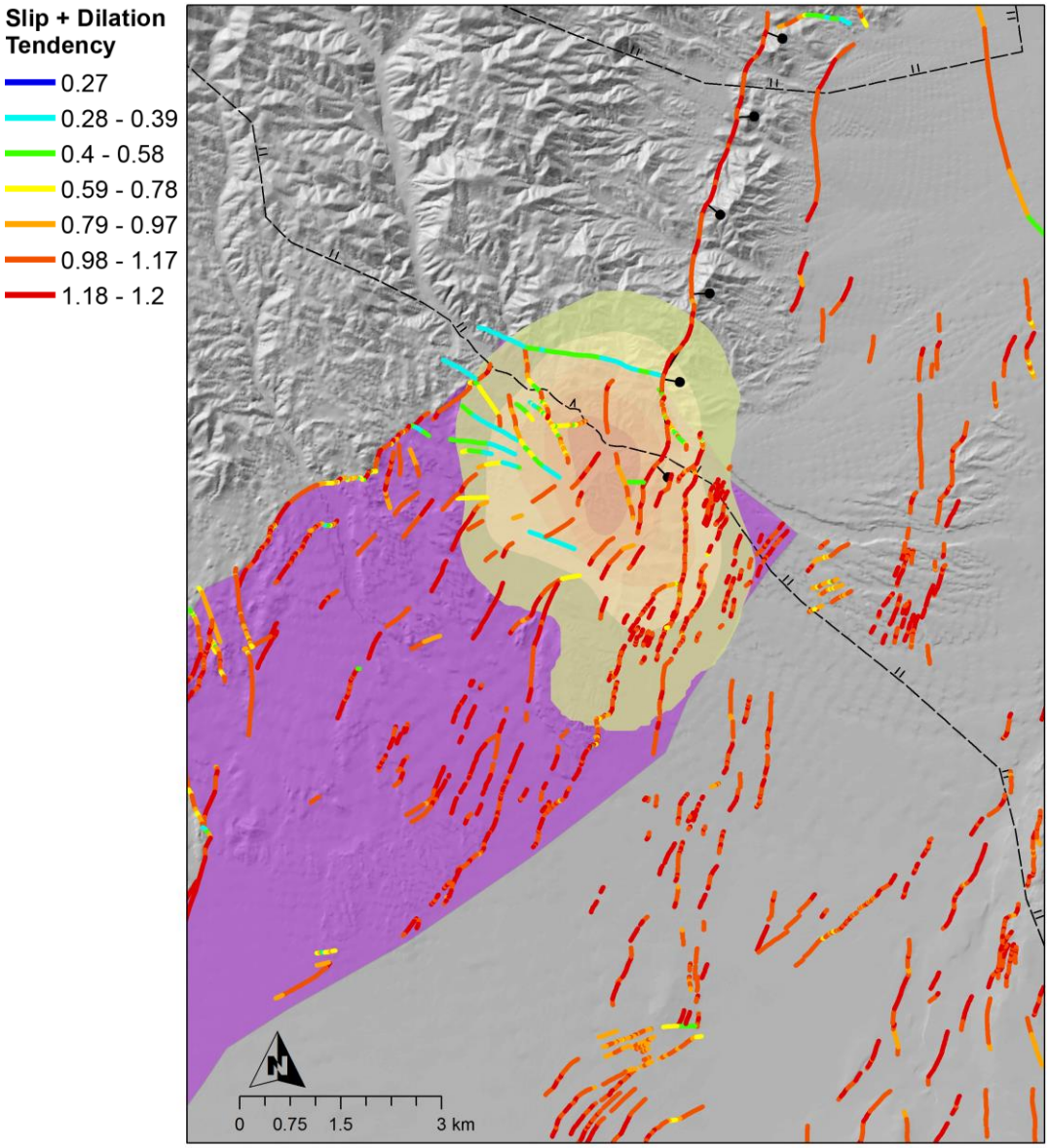

Figure 5.3. Map of structural features related to the EMC geothermal system on a DEM base. Faults are colored based on slip tendency plus dilation tendency, warmer colors represent increasing tendency and cooler colors represent decreasing tendency. Fault balls indicate the hanging wall of the Stillwater Range Frontal Fault. Purple shading represents Sand Springs -Stillwater accommodation zone. Caldera margin is the dashed black line with hachures indicating caldera interior.

5.3 Structural Controls on Geothermal Activity

A goal of this project was to evaluate previous studies and then integrate them into an interpretation of new data to create a structural framework that identifies the fluid pathways for deep circulation and upwelling of heated meteoric waters in the blind geothermal systems of southern Dixie Valley. Because previous attempts to exploit these resources had failed, the geothermal system was interpreted to be closely tied to structurally favorable settings where critically stressed fault zones with significant potential for dilation are oriented antithetically to the least principal stress direction (Barton et al., 1997; Davatzes and Hickman, 2010; Faulds et al., 2010; Faulds et al., 2013; Hickman and Davatzes, 2010; Moeck et al., 2009). Field reconnaissance, geophysical interpretations, structural analysis of faults, stress data, and slip and dilation tendency provide a new perspective on the characteristic geometries, kinematics, and deformation history and style that define the modern structural setting.

The study area is broadly characterized as a major accommodation zone that is a 10-20 km wide, 100 km long belt of intermeshing, east and west dipping, north-northeast oriented, active faults with motion that ranges from normal to dextral. This fault system incorporates multiple range bounding faults. It also includes numerous splaying, intersecting, and terminating faults that form step-overs, relay ramps, and displacement transfer zones that accommodate perturbations to the regional stress. Perturbations are theoretically generated by the proximity of the Walker Lane and represented by local strain transfer between dextral strike-slip and normal faults (i.e. Fairview Peak and Rainbow Mountain events transferred strain to the Dixie Valley fault).

The structural setting of the Pirouette Mountain geothermal system can be characterized as either a displacement transfer zone where dextral strain on the Louderback Mountains fault is transferred to normal strain on the Dixie Valley fault or as an accommodation zone where overlapping ruptures of opposing normal fault systems occur. Previous studies identify that little dextral offset occurs between correlative dikes that crop out on opposing sides of Fairview Valley (Caskey et al., 1996). This would suggest the accommodation zone description is the dominant setting given the large magnitude of vertical relief generated by extensional faulting. However, when considering the number of adjacent fault terminations and the Stillwater Range frontal fault relay ramp geometry that bounds the system to the west, the geothermal system is best described as a hybrid in terms of structural setting. This means that, similar to many of the producing geothermal systems of the Great Basin (Faulds et al., 2013), it appears to contain multiple favorable structural settings and supports the case for a causative relationship between structural complexity and geothermal potential. Thus, it should be considered a hybrid geothermal system of notable potential for exploitation.

Heat flow mapping indicates that shallow geothermal activity is most robust in the axial portion of the accommodation zone before terminating southward into the northwest plunging intrabasin high and the Louderback Mountains Fault. This intrabasin structure is also described herein as a fault-bound oblique anticlinal accommodation zone defined by a high central block (Figure 5.2 and 5.4)) with flanking depocenters crosscut by the overlapping, basinward dipping fault systems (Faulds and Varga, 1998). The northern limb of this anticline is visible in seismic line 5 (Plate 9) as a broad low amplitude structure dipping to the north-northeast and buried by

shallow lacustrine and alluvial deposits similar to those associated with Pleistocene Lake Dixie and the East Lee Canyon Alluvial Fan. The critical faults identified in Figure 5.1 and 5.2 (Faults 3, 4 and 5) that bound the oblique anticlinal accommodation zone are poorly oriented for slip and dilation and are acting as a low permeability zone that precludes fluid flow (Figure 5.4). However, where these structures intercept the northward continuation of the well oriented Louderback Mountains Fault (Fault 9) enhanced fluid flow appears to be occurring near the surface (Figure 5.2). This suggests that there is strong fracture permeability at this intersection and that there may be an intersection of a similar, unmapped, northerly striking structure with the anticlinal accommodation structure that coincides with the other significant near surface heat flow highs just to the north (Figure 5.4).

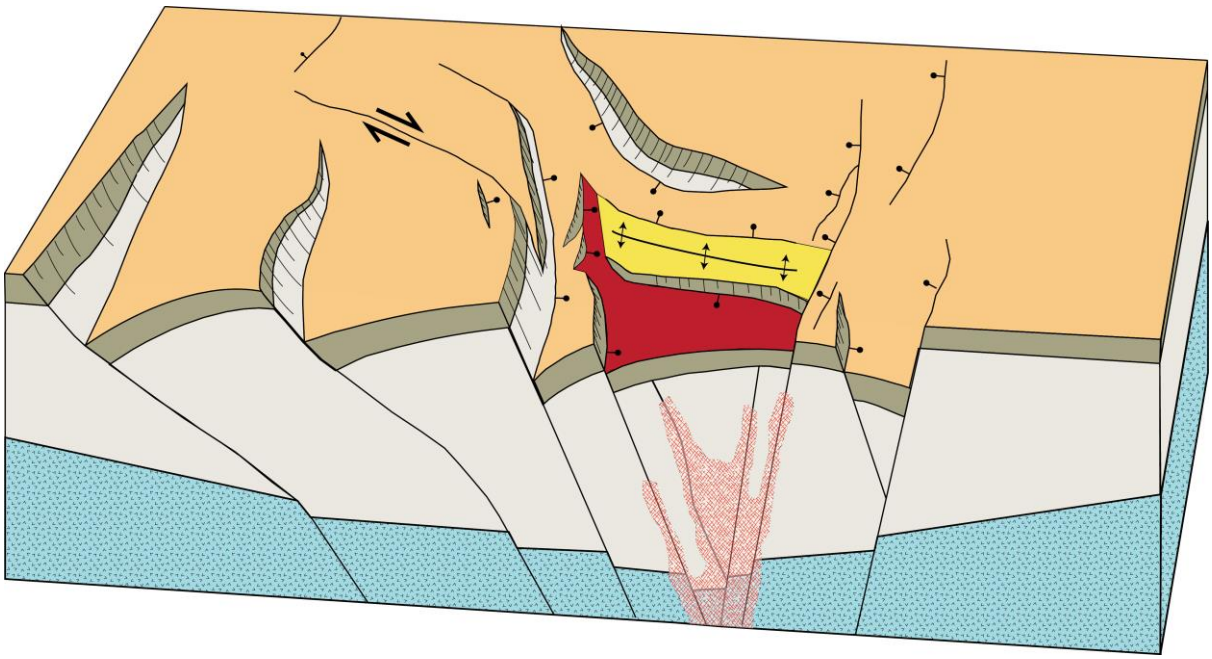

Figure 5.4. Schematic structural block diagram depiction of the oblique anticlinal accommodation zone (shaded yellow) formed between an oblique displacement transfer zone and a steeply dipping, synthetic normal fault bound relay ramp. Red shading identifies structurally favorable faults in the axial portion of the accommodation zone (shaded dark red) controlling fluid flow related to upwelling in the Pirouette Mountain Geothermal System before terminating against the oblique accommodation zone.

The Elevenmile Canyon geothermal system also resides in a hybrid structural setting. The dominant characteristic is a major step-over from the Sand Springs Range frontal fault to the Stillwater Range frontal fault. This is marked also by multiple east- and west-dipping normal faults that intersect the older north- south-dipping structures and generally terminate into the southern Elevenmile Canyon Caldera boundary. Based on the location of warm wells and heat flow data, the highest permeability appears to coincide with north-northeast striking faults in the immediate footwall of the Stillwater Range frontal fault. At this location several prominent structures terminate into or possibly cross-cut Elevenmile Canyon. This area also coincides with hydrothermal mineral alteration that may have formed during a period of higher base level

and/or a more intense period of geothermal activity (Figure 1.6) (Calvin et al., 2012; Lamb, 2011). This evidence suggests that the geothermal fluids rise along the caldera boundary flow laterally basinward towards Fairview Valley. The lack of more intense heat flow near the surface would suggest this smaller system to be a less economic resource that could benefit from further research.

Heat flow mapping and structural analysis of the study area show that meteoric waters ascend discrete segments of steeply dipping, north-northeast trending structures as a result of geothermal heating. These findings conform to those of previous studies that have shown faults and fractures oriented near orthogonal to the least principal stress direction to have the greatest hydraulic conductivity (Barton et al., 1997; Hickman et al., 2000; Moeck et al., 2009). An analysis of the modern stress regime where fault kinematics, geodetics, and focal mechanism solutions were examined to generate a common axis of extension that not only fits the local data, but also conforms to the regionally active northwest-southeast extension (Caskey et al., 1996; Hammond and Thatcher, 2007; Hodgkinson et al., 1996; Kreemer et al., 2009; Kreemer and Hammond, 2007; Zoback et al., 1994). Further, the relationship between the orientation and magnitude of the least principal stress and the resulting values of shear and normal stress resolve the distribution of slip and dilation tendency with respect to the given plane(s), thus, steeply dipping north-northeast trending faults are most likely to experience enhanced permeability under natural conditions, excluding any extreme or otherwise unknown variations to the frictional characteristics of a surface or rock type (Ferrill and Morris, 2003; Morris et al., 1996)x. Consequently, the predominance of geothermal activity along north-

northeast trending structures in the Great Basin and a lack of activity and/or barrier-like behavior related to west-northwest oriented structures are directly apparent.

6. Conclusions

Structural and stratigraphic data integrated into geophysical subsurface interpretations provide new insight on how the kinematics, shifting stress state, and fault behavior contribute to the structural framework contributing to the geothermal systems of southern Dixie Valley. The stratigraphy of southern Dixie Valley is composed of metamorphosed Mesozoic rocks deformed in the hanging-wall of the Luning-Fencemaker Thrust fault. These rocks are highly disrupted, intruded and overlain by the intense ignimbrite activity of the Stillwater Caldera Complex. Neogene strata deposited in post ignimbrite-flare-up quiescence and capped by volcanic rocks are exposed in the area. Perched in an abandoned basin above the modern valley floor, Neogene strata form gently to moderately east and west tilted fault blocks, transtensionally folded in places, and bound by northerly striking normal faults of the earliest basin and range extension beginning around 14 Ma. The perched basin, although formed under a slightly rotated extension axis, provides the ideal surface analog for interpretation of subsurface structural conditions related to the adjacent fault controlled geothermal systems.

The subsurface geology of the Pirouette Mountain geothermal system is made up of caldera deposits from the Stillwater Caldera Complex overlain by Quaternary sediments, with little evidence of Neogene sediment deposition. It also includes the Freeman Creek Pluton and the Mesozoic Metamorphic rocks they intrude or are faulted against. Subsurface geology of the Elevenmile Canyon geothermal system has a much thinner section of caldera related rocks and

rapidly transitions to Mesozoic Metaphoric rocks and older granitic rocks of the Cretaceous La Plata Pluton (Figure 6.1 and Plate 11). Although the Elevenmile Canyon geothermal system is clearly related to the southern caldera margin, there is some geophysical evidence to suggest that the Pirouette Mountain geothermal system also associates with a north-south oriented section of the caldera margin that is buried in southern Dixie Valley.

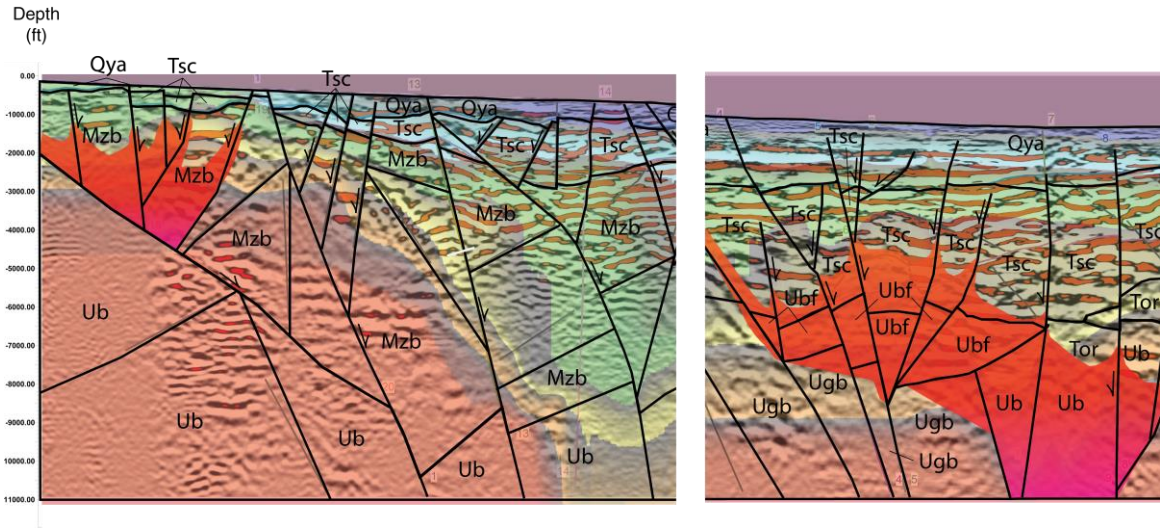

Figure 6.1. Seismic velocity model overlain with geologic cross section. Seismic sections 4 (left) imaging EMC geothermal system and seismic section 2 (right) imaging PM geothermal system. Potential fluid pathways shaded in red

The structural analysis of the Pirouette Mountain geothermal system reveals a hybrid structural setting characterized by several sets of structures oriented favorably for conduction of fluids. The first, an oblique anticlinal accommodation zone that separates two major normal fault systems. The second is a displacement transfer zone that translates minor dextral slip from the Louderback Mountains fault across the accommodation zone to the Dixie Valley Fault. The third is the left stepover or relay ramp in the Dixie Valley fault that bounds the accommodation

zone on the west. The Elevenmile Canyon geothermal system is also a hybrid structural setting characterized by a major step-over in the range bounding faults of the Sand Springs and Stillwater ranges, in which multiple north-northeast trending fault strands intersect and crosscut east-west trending faults that parallel Elevenmile Canyon. Both systems have numerous fault intersections and terminations that dip steeply, offset basement, and generate increased permeability at depth where they coalesce with other structures. They also share a relationship with a network of potential ring fractures related to the subsidence of the Stillwater Caldera Complex that may further enhance permeability at depth.

Kinematic fault data and focal mechanism solutions define a northwest-trending extension direction in central Nevada since 14-12 Ma with a slight clockwise rotation coinciding with the onset of lateral motion in the Walker Lane belt to the south. These data also establish the mean stress orientations and define moderate to steeply dipping north-northeast trending faults and fractures as having the highest tendency to slip and dilate. These orientations are also compatible with observations of elevated heat flow coinciding with similarly oriented faults at Pirouette Mountain and Elevenmile Canyon.

The results of this study identifies an axial portion of the accommodation zone at Pirouette Mountain that terminates antithetically into the axis of the oblique anticline at depths of about 2,000 m as a zone of particular interest that may represent the top of a moderate temperature reservoir. The east and west dipping faults located in the immediate hanging wall of the Dixie Valley fault where it crosses Elevenmile Canyon, were also identified as the favorable structural setting for geothermal activity related to the Elevenmile Canyon Geothermal system. However,

it appears that the fluids may be rising along the Caldera Margin at Elevenmile Canyon then flowing laterally to the south where they intersect preferentially oriented structures.

6.1 Recommendations for further exploration

Drilling of the Pirouette Mountain geothermal system prospect to a moderate depth, acquiring core, and evaluating the geochemistry of rocks and fluids associated with high temperature intervals would be very beneficial to a better understanding of the geothermal system life cycle and evaluation of the necessity for drilling deeper. The likely development scenario would include wells drilled beyond 10,000 feet. Unnecessary costs could be avoided by understanding the shallow upper reservoir section. There could also be revisions made to geophysical data and the occurrence model if core data, sonic logs, microseismic, and various well test data were acquired. Well data could be further used for joint modeling of the seismic, magnetic, and gravity to improve subsurface imaging laterally and to greater depths and the geochemistry of fluids, fluid inclusions, XRD, and radiometric and thermochronologic dating would improve our understanding of the age and nature of the geothermal system.

7. References

Abbott, R. E., Louie, J. N., Caskey, S. J., and Pullammanappallil, S., 2001, Geophysical confirmation of low-angle normal slip on the historically active Dixie Valley fault, Nevada: Journal of Geophysical Research: Solid Earth (1978–2012), v. 106, no. B3, p. 4169-4181.

Allmendinger, R., 2014, Rick Allmendinger's Stuff, Volume 2015.

Allmendinger, R. W., Cardozo, N., and Fisher, D. M., 2011, Structural Geology Algorithms: Vectors and Tensors, Cambridge University Press.

Anderson, R. E., Berger, B. R., and Miggins, D., 2012, Timing, magnitude, and style of Miocene deformation, west-central Walker Lane belt, Nevada: Lithosphere, v. 4, no. 3, p. 187-208.

Angelier, J., 1989, From orientation to magnitudes in paleostress determinations using fault slip data: Journal of Structural Geology, v. 11, no. 1, p. 37-50.

Atwater, T., and Stock, J., 1998, Pacific-North America plate tectonics of the Neogene southwestern United States: an update: International Geology Review, v. 40, no. 5, p. 375-402.

Barton, C. A., Hickman, S., Morin, R. H., Zoback, M. D., Finkbeiner, T., Sass, J., and Benoit, D., 1997, Fracture permeability and its relationship to in-situ stress in the Dixie Valley, Nevada, geothermal reservoir.

Bell, J. W., Caskey, S. J., and House, P. K., 2009, Geologic Map of the Lahontan Mountains Quadrangle, Churchill County, Nevada: Nevada Bureau of Mines and Geology.

Bell, J. W., Caskey, S. J., Ramelli, A. R., and Guerrieri, L., 2004, Pattern and rates of faulting in the central Nevada seismic belt, and paleoseismic evidence for prior beltlike behavior: Bulletin of the Seismological Society of America, v. 94, no. 4, p. 1229-1254.

Bell, J. W., and Ramelli, A. R., 2007, Active faults and neotectonics at geothermal sites in the western Basin and Range: Preliminary results: Geothermal Resources Council Transactions, v. 31, p. 375-378.

Bell, J. W., and Tingley, S. L., 1984, Quaternary fault map of Nevada, Reno sheet, Nevada Bureau of Mines and Geology, University of Nevada Reno.

Bergfeld, D., Goff, F., and Janik, C. J., 2001, Elevated carbon dioxide flux at the Dixie Valley geothermal field, Nevada; relations between surface phenomena and the geothermal reservoir: Chemical Geology, v. 177, no. 1, p. 43-66.

Blackwell, D., Smith, R., and Richards, M., Exploration and development at Dixie Valley, Nevada: summary of doe studies, *in* Proceedings Proceedings of the 32nd Workshop on Geothermal Reservoir Engineering Stanford University2007, p. 22-24.

Blackwell, D. D., 1983, Heat flow in the northern Basin and Range province: Geothermal Resources Council Special Report, v. v. 13, p. p. 81-93.

Blackwell, D. D., Golan, B., and Benoit, D., 2000, Thermal regime in the Dixie Valley geothermal system: Geothermal Resources Council Transactions, v. 24, p. 223-228.

Blackwell, J. D., and Richards, M., 2004, Geothermal map of North America: American Association of Petroleum Geologist, scale 1:6,500,000.

Blake, K., STRESS ANALYSIS FOR BOREHOLES ON DEPARTMENT OF DEFENSE LANDS IN THE WESTERN UNITED STATES: A STUDY IN STRESS HETEROGENEITY, *in* Proceedings Proceedings, Thirty-Eighth Workshop on Geothermal Reservoir Engineering2013.

Blake, K., and Davatzes, N. C., Borehole image log and statistical analysis of FOH-3D, Fallon Naval Air Station, NV, *in* Proceedings Proceedings, Thirty-Seventh Workshop on Geothermal Reservoir Engineering Stanford University, Stanford, California2012.

Blakely, R. J., 1996, Potential theory in gravity and magnetic applications, Cambridge University Press.

Calvin, W. M., Bell, J. W., and Hinz, N. H., 2012, Final Technical Report: Geothermal Assessment of NAS Fallon Land: Navy Geothermal Program Office Internal Document.

Caskey, S., and Wesnousky, S., 1997, Static stress changes and earthquake triggering during the 1954 Fairview Peak and Dixie Valley earthquakes, Central Nevada: Bulletin of the Seismological Society of America, v. 87, no. 3, p. 521-527.

Caskey, S., Wesnousky, S., Zhang, P., and Slemmons, D., 1996, Surface faulting of the 1954 Fairview Peak (MS 7.2) and Dixie Valley (MS 6.8) earthquakes, central Nevada: Bulletin of the Seismological Society of America, v. 86, no. 3, p. 761-787.

Caskey, S. J., Bell, J. W., Ramelli, A. R., and Wesnousky, S. G., 2004, Historic surface faulting and paleoseismicity in the area of the 1954 Rainbow Mountain-Stillwater earthquake sequence, central Nevada: Bulletin of the Seismological Society of America, v. 94, no. 4, p. 1255-1275.

Caskey, S. J., and Wesnousky, S. G., 2000, Active faulting and stress redistributions in Dixie Valley, Beowawe, and Bradys geothermal fields: Implications for geothermal exploration in the Basin and Range: 25th workshop on Geothermal Reservoir Engineering, Stanford University, p. p. 24-26.

Cassel, E. J., Breecker, D. O., Henry, C. D., Larson, T. E., and Stockli, D. F., 2014, Profile of a paleo-orogen: High topography across the present-day Basin and Range from 40 to 23 Ma: Geology, v. 42, no. 11, p. 1007-1010.

Center, O. G.-H., 2005, Geothermal Direct-Use Case Studies: Website: http://geoheat. oit. edu/casestudies. htm. Accessed: June, v. 23, p. 2008.

Colgan, J. P., 2013, Reappraisal of the relationship between the northern Nevada rift and Miocene extension in the northern Basin and Range Province: Geology, v. 41, no. 2, p. 211-214.

Colgan, J. P., and Henry, C. D., 2009, Rapid middle Miocene collapse of the Mesozoic orogenic plateau in north-central Nevada: International Geology Review, v. 51, no. 9-11, p. 920-961.

Colgan, J. P., John, D. A., Henry, C. D., and Fleck, R. J., 2008, Large-magnitude Miocene extension of the Eocene Caetano caldera, Shoshone and Toiyabe Ranges, Nevada: Geosphere, v. 4, no. 1, p. 107-130.

Coolbaugh, M. F., Raines, G. L., and Zehner, R. E., 2007, Assessment of exploration bias in data-driven predictive models and the estimation of undiscovered resources: Natural Resources Research, v. 16, no. 2, p. 199-207.

Curewitz, D., and Karson, J. A., 1997, Structural settings of hydrothermal outflow: Fracture permeability maintained by fault propagation and interaction: Journal of Volcanology and Geothermal Research, v. 79, no. 3, p. 149-168.

Davatzes, N. C., and Hickman, S., The feedback between stress, faulting, and fluid flow: Lessons from the Coso Geothermal Field, CA, USA, *in* Proceedings Proceedings World Geothermal Congress 20102010, p. 1-14.

Dewey, J. F., 2002, Transtension in arcs and orogens: International Geology Review, v. 44, no. 5, p. 402-439.

Dickinson, W. R., 2006, Geotectonic evolution of the Great Basin: Geosphere, v. 2, no. 7, p. 353-368.

-, 2013, Phanerozoic palinspastic reconstructions of Great Basin geotectonics (Nevada-Utah, USA): Geosphere, v. 9, no. 5, p. 1384-1396.

Doser, D. I., 1986, Earthquake processes in the Rainbow Mountain-Fairview Peak-Dixie Valley, Nevada, region 1954–1959: Journal of Geophysical Research: Solid Earth (1978–2012), v. 91, no. B12, p. 12572-12586.

Edmiston, R., 1985, Basin and Range Geothermal Systems with Fluid Temperatures of: Geothermal Resources Council Bulletin.

Faulds, J. E., Coolbaugh, M., Blewitt, G., and Henry, C. D., 2004, Why is Nevada in hot water? Structural controls and tectonic model of geothermal systems in the northwestern great basin: Geothermal Resources Council Transactions, v. v. 28, p. p. 649-654.

Faulds, J. E., Coolbaugh, M. F., Benoit, D., Oppliger, G., Perkins, M., Moeck, I., and Drakos, P., 2010, Structural Controls of Geothermal Activity in the Northern Hot Springs Mountains, Western Nevada: The Tale of Three Geothermal Systems (Brady‟ s, Desert Peak, and Desert Queen): Geothermal Resources Council Transactions, v. 34, p. 675-683.

Faulds, J. E., Garside, L. J., and Oppliger, G. L., 2003, Structural Analysis of the Desert Peak-Brady Geothermal Field, Northwestern Nevada: Implications for Understanding Linkages Between Northeast-Trending Structures and Geothermal Reservoirs in the Humboldt Structural Zone: Transactions-Geothermal Resources Council, p. 859-864.

Faulds, J. E., and Henry, C. D., 2008, Tectonic influences on the spatial and temporal evolution of the Walker Lane: An incipient transform fault along the evolving Pacific-North American plate boundary: in Spencer, J.E., and Titley, S.R., eds., Circum-Pacific Tectonics, Geologic Evolution and Ore Deposits: Tuscon, Arizona Geological Society, v. Digest 22, p. p. 437-470.

Faulds, J. E., Henry, C. D., Coolbaugh, M. F., Garside, L. J., and Castor, S. B., Late Cenozoic strain field and tectonic setting of the northwestern Great Basin, western USA: Implications for geothermal activity and mineralization, *in* Proceedings Geological Society of Nevada Symposium2005, p. 1091-1104.

Faulds, J. E., Hinz, N., Kreemer, C., and Coolbaugh, M., 2012a, Regional Patterns of Geothermal Activity in the Great Basin Region, Western USA: Correlation with Strain Rates: Geothermal Resources Council Transactions, v. 36, p. 897-902.

Faulds, J. E., Hinz, N. H., Coolbaugh, M. F., Cashman, P. H., Kratt, C., Dering, G., Edwards, J., Mayhew, B., and McLachlan, H., 2011, Assessment of favorable structural settings of geothermal systems in the Great Basin, western USA: Geothermal Resources Council Transactions, v. 35, p. 777-783.

Faulds, J. E., Hinz, N. H., Dering, G. M., and Siler, D. L., 2013, The Hybrid Model—The Most Accommodating Structural Setting for Geothermal Power Generation in the Great Basin, Western USA: Geothermal Resources Council Transactions, v. 37, p. 3-10.

Faulds, J. E., Hinz, N. H., Kreemer, C., and Coolbaugh, M. F., 2012b, Regional Patterns of Geothermal Activity in the Great Basin Region, Western USA: Correlation with Strain Rates: Geothermal Resource Council Transactions, v. v. 36, p. p. 897-902.

Faulds, J. E., and Varga, R. J., 1998, The role of accommodation zones and transfer zones in the regional segmentation of extended terranes: SPECIAL PAPERS-GEOLOGICAL SOCIETY OF AMERICA, p. 1-46.

Ferrill, D. A., and Morris, A. P., 2003, Dilational normal faults: Journal of Structural Geology, v. 25, no. 2, p. 183-196.

Fosdick, J., and Colgan, J., 2008, Miocene extension in the East Range, Nevada: A two-stage history of normal faulting in the northern Basin and Range: Geological Society of America Bulletin, v. 120, no. 9-10, p. 1198-1213.

Fournier, R., 1977, Chemical geothermometers and mixing models for geothermal systems: Geothermics, v. 5, no. 1, p. 41-50.

Gonsior, Z. J., and Dilles, J. H., 2008, Timing and evolution of Cenozoic extensional normal faulting and magmatism in the southern Tobin Range, Nevada: Geosphere, v. 4, no. 4, p. 687-712.

Gorynski, K. E., Walker, J. D., Stockli, D. F., and Sabin, A., 2014, Apatite (U–Th)/He thermochronometry as an innovative geothermal exploration tool: A case study from the southern Wassuk Range, Nevada: Journal of Volcanology and Geothermal Research, v. 270, p. 99-114.

Hammond, W. C., and Thatcher, W., 2004, Contemporary tectonic deformation of the Basin and Range province, western United States: 10 years of observation with the Global Positioning System: Journal of Geophysical Research: Solid Earth (1978–2012), v. 109, no. B8.

-, 2007, Crustal deformation across the Sierra Nevada, northern Walker Lane, Basin and Range transition, western United States measured with GPS, 2000–2004: Journal of Geophysical Research: Solid Earth (1978–2012), v. 112, no. B5.

Helton, E. L. B., John W.; Cashman, Patricia H.; Lazaro, Michael; Alm, Steve, 2011, Structural Analysis of Southern Dixie Valley Using LiDAR and Low-Sun-Angle Aerial Photography, NAS Fallon Geothermal Exploration Project, Dixie Valley, Nevada: Geothermal Resource Council Transactions, v. 35, p. 811-815.

Henry, C. D., 1996a, Geologic map of the Bell Canyon quadrangle, western Nevada, Nevada Bureau of Mines and Geology.

-, 1996b, Geologic map of the Bell Mountain quadrangle, western Nevada, Nevada Bureau of Mines and Geology.

Henry, C. D., and John, D. A., 2013, Magmatism, ash-flow tuffs, and calderas of the ignimbrite flareup in the western Nevada volcanic field, Great Basin, USA: Geosphere, v. 9, no. 4, p. 951-1008.

Henry, C. D., McGrew, A. J., Colgan, J. P., Snoke, A. W., and Brueseke, M. E., 2011, Timing, distribution, amount, and style of Cenozoic extension in the northern Great Basin: Field Guides, v. 21, p. 27-66.

Henry, C. D., and Perkins, M. E., 2001, Sierra Nevada–Basin and Range transition near Reno, Nevada: two-stage development at 12 and 3 Ma: Geology, v. 29, no. 8, p. 719-722.

Hickman, S., Zoback, M., Barton, C., Benoit, R., Svitek, J., and Summers, R., Stress and permeability heterogeneity within the Dixie Valley geothermal reservoir: Recent results from well 82-5, *in* Proceedings Proceedings 25th Workshop on Geothermal Reservoir Engineering2000, p. 256-265.

Hickman, S. H., and Davatzes, N. C., 2010, In-situ stress and fracture characterization for planning of an EGS stimulation in the Desert Peak Geothermal Field, Nevada.

Hinz, N., 2011, Preliminary geologic map of the Bunejug Mountains quadrangle, Churchill County, Nevada-Salt Wells Geothermal Area: DOE Geothermal Data Repository; University of Nevada Reno.

Hinz, N. H., Faulds, J. E., and coolbaugh, M., 2014, Association of Fault Terminations With Fluid Flow

in the Salt Wells Geothermal Field, Nevada, USA: Geothermal Resource Council Transactions, v. 38, p. 3-9.

Hodgkinson, K. M., Stein, R. S., and King, G. C., 1996, The 1954 Rainbow Mountain-Fairview Peak-Dixie Valley earthquakes: A triggered normal faulting sequence: Journal of Geophysical Research: Solid Earth (1978–2012), v. 101, no. B11, p. 25459-25471.

Hudson, M. R., and Geissman, J. W., 1991, Paleomagnetic evidence for the age and extent of middle Tertiary counterclockwise rotation, Dixie Valley region, west central Nevada: Journal of Geophysical Research: Solid Earth (1978–2012), v. 96, no. B3, p. 3979-4006.

Hudson, M. R., John, D. A., Conrad, J. E., and McKee, E. H., 2000, Style and age of late Oligocene-early Miocene deformation in the southern Stillwater Range, west central Nevada: Paleomagnetism, geochronology, and field relations: Journal of Geophysical Research: Solid Earth (1978–2012), v. 105, no. B1, p. 929-954.

John, D., Late Cenozoic volcanotectonic evolution of the southern Stillwater Range, west-central Nevada, *in* Proceedings Structure, tectonics and mineralization of the Walker Lane, a short symposium1992, p. 64-92.

John, D. A., 1995, Tilted middle Tertiary ash-flow calderas and subjacent granitic plutons, southern Stillwater Range, Nevada: Cross sections of an Oligocene igneous center: Geological Society of America Bulletin, v. 107, no. 2, p. 180-200.

John, D. A., and Silberling, N. J., 1994, Geologic map of the La Plata Canyon quadrangle, Churchill County, Nevada, US Geological Survey.

Kreemer, C., 2014, personal communication.

Kreemer, C., Blewitt, G., and Hammond, W. C., 2009, Geodetic constraints on contemporary deformation in the northern Walker Lane: 2. Velocity and strain rate tensor analysis: Geological Society of America Special Papers, v. 447, p. 17-31.

Kreemer, C., and Hammond, W. C., 2007, Geodetic constraints on areal changes in the Pacific–North America plate boundary zone: What controls Basin and Range extension?: Geology, v. 35, no. 10, p. 943-946.

Kreemer, C., Hammond, W. C., Blewitt, G., Holland, A. A., and Bennett, R. A., A geodetic strain rate model for the Pacific-North American plate boundary, western United States, *in* Proceedings EGU General Assembly Conference Abstracts2012, Volume 14, p. 6785.

Lachenbruch, A. H., and Sass, J., 1977, Heat flow in the United States and the thermal regime of the crust: The Earth's crust, p. 626-675.

Lamb, A. K., Chris; Calvin, Wendy, 2011, Geothermal Exploration Using Hyperspectral Analysis Over Dixie Valley and Fairview Valleys, Nevada: Geothermal Resource Council Transactions, v. 35, p. p. 867-871.

Lee, J., Stockli, D. F., Owen, L. A., Finkel, R. C., and Kislitsyn, R., 2009, Exhumation of the Inyo Mountains, California: Implications for the timing of extension along the western boundary of the Basin and Range Province and distribution of dextral fault slip rates across the eastern California shear zone: Tectonics, v. 28, no. 1.

Mankhemthong, N., 2008, Structure of the inter-basin transition zone between Dixie Valley and Fairview Valley, Nevada, USA: UNIVERSITY OF NEVADA, RENO.

Marrett, R., and Allmendinger, R. W., 1990, Kinematic analysis of fault-slip data: Journal of Structural Geology, v. 12, no. 8, p. 973-986.

Matek, B., 2013, 2014 Annual U.S. & Global Geothermal Power Production Report: Website: http://geoenergy.org/events/2014%20Annual%20US%20&%20Global%20Geothermal%20Power%20Production%20Report%20Final.pdf.

McQuarrie, N., and Oskin, M., 2010, Palinspastic restoration of NAVDat and implications for the origin of magmatism in southwestern North America: Journal of Geophysical Research: Solid Earth (1978–2012), v. 115, no. B10.

McQuarrie, N., and Wernicke, B. P., 2005, An animated tectonic reconstruction of southwestern North America since 36 Ma: Geosphere, v. 1, no. 3, p. 147-172.

Micklethwaite, S., and Cox, S. F., 2004, Fault-segment rupture, aftershock-zone fluid flow, and mineralization: Geology, v. 32, no. 9, p. 813-816.

Moeck, I., Kwiatek, G., and Zimmermann, G., 2009, Slip tendency analysis, fault reactivation potential and induced seismicity in a deep geothermal reservoir: Journal of Structural Geology, v. 31, no. 10, p. 1174-1182.

Morris, A., Ferrill, D. A., and Henderson, D. B., 1996, Slip-tendency analysis and fault reactivation: Geology, v. 24, no. 3, p. 275-278.

Oldow, J., Late Cenozoic displacement partitioning in the northwestern Great Basin, *in* Proceedings Structure, Tectonics and Mineralization of the Walker Lane, Stewart, J., ed., Walker Lane Symposium Proceedings Volume, Geological Society of Nevada, Reno, NV1992, p. 17-52.

Oldow, J., Aiken, C., Hare, J., Ferguson, J., and Hardyman, R., 2001, Active displacement transfer and differential block motion within the central Walker Lane, western Great Basin: Geology, v. 29, no. 1, p. 19-22.

Oldow, J., Geissman, J., and Stockli, D., 2008, Evolution and strain reorganization within late Neogene structural stepovers linking the central Walker Lane and northern Eastern California shear zone, western Great Basin: International Geology Review, v. 50, no. 3, p. 270-290.

Page, B., 1965, Preliminary geologic map of a part of the Stillwater Range, Churchill County, Nevada, Map 28, scale 1: 125,000: Nev. Bur. of Mines and Geol., Reno.

Parry, W., Hedderly-Smith, D., and Bruhn, R., 1991, Fluid inclusions and hydrothermal alteration on the Dixie Valley fault, Nevada: Journal of Geophysical Research: Solid Earth (1978–2012), v. 96, no. B12, p. 19733-19748.

Pullammanappallil, S., 2013, Technical Report: 2D Active Source Seismic REflection Data Acquisition and Processing Southern Dixie Valley, Churchill County, Nevada, Unpublished internal report delivered to Navy geothermal Program Office by CH2M Hill and prepared by OPtim software and data solutions

Pullammanappallil, S. K., and Louie, J. N., 1993, Inversion of seismic reflection traveltimes using a nonlinear optimization scheme: Geophysics, v. 58, no. 11, p. 1607-1620.

Rhodes, G. T., 2011, Structural Controls of the San Emidio Geothermal System, Northwestern Nevada, UNIVERSITY OF NEVADA, RENO.

Rowan, L. C., and Wetlaufer, P. H., 1981, Relation between regional lineament systems and structural zones in Nevada: AAPG Bulletin, v. 65, no. 8, p. 1414-1432.

Sass, J., Lachenbruch, A. H., Munroe, R. J., Greene, G. W., and Moses, T. H., 1971, Heat flow in the western United States: Journal of Geophysical Research, v. 76, no. 26, p. 6376-6413.

Sass, J. H., Lachenbruch, A.H., G. J., S.P, Morgan, P., Priest, S. S., Moses Jr., T. H., and Munroe, R. J., 1994, Thermal regime of the southern Basin and Range Province. 1. Heat flow data from Arizona and the Mojave Desert of California and Nevada: J. Geophysical Research, v. v. 99, p. p. 22093-22119.

Schaefer, D. H., 1983, Gravity survey of Dixie Valley, west-central Nevada, US Geological Survey.

Shevenell, L., and Coolbaugh, M., 2011, A New Method of Evaluation of Chemical Geothermometers for Calculating Reservoir Temperatures from Thermal Springs in Nevada: Geothermal Resource Council Transactions, v. 35, p. 657-661.

Skord, J. S., Chris; Coolbaugh, Mark; Cashman, Patricia H.,; Lazaro, Michael; Kratt, Chris, 2011, Two-Meter Temperature Surveys

for Geothermal Exploration Project at NAS Fallon: Geothermal Resource Council Transactions, v. 35, p. 1023-1027.

Slemmons, D. B., 1957, Geological effects of the Dixie valley-Fairview peak, Nevada, earthquakes of December 16, 1954: Bulletin of the Seismological Society of America, v. 47, no. 4, p. 353-375.

Stock, J., Healy, J., Hickman, S., and Zoback, M., 1985, Hydraulic fracturing stress measurements at Yucca Mountain, Nevada, and relationship to the regional stress field: Journal of Geophysical Research: Solid Earth (1978–2012), v. 90, no. B10, p. 8691-8706.

Stockli, D. F., Dumitru, T. A., McWilliams, M. O., and Farley, K. A., 2003, Cenozoic tectonic evolution of the White Mountains, California and Nevada: Geological Society of America Bulletin, v. 115, no. 7, p. 788-816.

Stockli, D. F., Surpless, B. E., Dumitru, T. A., and Farley, K. A., 2002, Thermochronological constraints on the timing and magnitude of Miocene and Pliocene extension in the central Wassuk Range, western Nevada: Tectonics, v. 21, no. 4, p. 10-11-10-19.

Trexler, J. H., Cashman, P. H., Snyder, W. S., and Davydov, V. I., 2004, Late Paleozoic tectonism in Nevada: Timing, kinematics, and tectonic significance: Geological Society of America Bulletin, v. 116, no. 5-6, p. 525-538.

Unruh, J., Pullammanappallil, S., Honjas, W., and Monastero, F., 2006, New seismic imaging of the Coso geothermal field, Eastern California: Geology, v. 2, no. 3, p. 3-4.

Waibel, A., 2011, Structural controls on the location of geothermal cells in and adjacent to Dixie Valley, Nevada: GRC Transactions, v. 35, no. 8.

Walker, J., Sabin, A., Unruh, J., Monastero, F., and Combs, J., Development of genetic occurrence models for geothermal prospecting, *in* Proceedings Geothermal Resource Council Transactions2005, Volume v. 29, p. p. 309-314.

Williams, M. A., 2012, Thermal and structural assessment of the Pirouette Mountain geothermal prospect, Southern Dixie Valley, Nevada; MS Thesis, Huffington Dept. of Earth Sciences, Southern Methodist University: ProQuest, UMI Dissertations Publishing, v. 1532148.

Wisian, K. W., Blackwell, D. D., and Richards, M., 2001, Correlation of surface heat loss and total energy production for geothermal systems: Transactions-Geothermal Resources Council, p. 331-336.

Zoback, M. L., Anderson, R., and Thompson, G., 1981, Cainozoic evolution of the state of stress and style of tectonism of the Basin and Range province of the western United States: Philosophical Transactions of the Royal Society of London. Series A, Mathematical and Physical Sciences, v. 300, no. 1454, p. 407-434.

Zoback, M. L., McKEE, E. H., Blakely, R. J., and Thompson, G. A., 1994, The northern Nevada rift: Regional tectono-magmatic relations and middle Miocene stress direction: Geological Society of America Bulletin, v. 106, no. 3, p. 371-382.

Zoback, M. L., and Zoback, M., 1980, State of stress in the conterminous United States: Journal of Geophysical Research: Solid Earth (1978–2012), v. 85, no. B11, p. 6113-6156.

8. APPENDIX A: $^{40}Ar/^{39}Ar$ GEOCRONOLOGY

Table 2: LP-4 - Palgioclase and Groundmass

OSU Argon Geochronology Lab
CEOAS Oregon State University, Corvallis, USA

Incremental Heating			36Ar(a) [fA]	37Ar(ca) [fA]	38Ar(cl) [fA]	39Ar(k) [fA]	40Ar(r) [fA]	Age ± 2σ (Ma)	40Ar(r) (%)	39Ar(k) (%)	K/Ca ± 2σ
14D10105	1.7 %	☒	0.2698446	47.3344	0.741955	0.6072	3.5897	18.74 ± 6.57	4.31	0.04	0.006 ± 0.001
14D10107	1.9 %	☒	0.0706294	54.2351	0.175287	0.4921	2.4198	15.60 ± 4.54	10.39	0.03	0.004 ± 0.001
14D10108	2.1 %	☒	0.0353466	50.0328	0.044348	0.4657	2.7745	18.88 ± 4.54	20.99	0.03	0.004 ± 0.001
14D10110	2.5 %	☒	0.0410662	75.5471	0.062119	0.6003	3.1137	16.45 ± 3.42	20.42	0.04	0.003 ± 0.000
14D10111	2.9 %	☒	0.0425295	158.4098	0.052470	1.2937	6.2983	15.45 ± 1.71	33.38	0.08	0.004 ± 0.000
14D10113	3.1 %	☒	0.0351789	228.0557	0.049935	1.8590	8.7454	14.93 ± 1.18	45.69	0.12	0.004 ± 0.000
14D10114	3.6 %	☒	0.0242946	186.9122	0.044051	1.4767	7.3964	15.89 ± 1.54	50.74	0.09	0.003 ± 0.000
14D10116	4.2 %	☒	0.0457809	423.5972	0.070462	3.4194	16.7512	15.54 ± 0.79	55.32	0.21	0.003 ± 0.000
14D10117	4.8 %	☒	0.0217973	297.0395	0.005729	2.4300	11.5099	15.03 ± 0.97	64.11	0.15	0.004 ± 0.000
14D10119	5.6 %	☒	0.0276882	386.8687	0.078756	3.3933	15.7089	14.69 ± 0.76	65.74	0.21	0.004 ± 0.000
14D10120	6.4 %	☒	0.0400132	514.9558	0.024683	4.7470	22.3754	14.96 ± 0.57	65.42	0.30	0.004 ± 0.000
14D10122	7.4 %	☒	0.0341009	400.9983	0.014389	4.0507	19.0356	14.91 ± 0.63	65.38	0.25	0.004 ± 0.000
14D10123	8.4 %	☒	0.0458977	317.3737	0.056173	3.7492	17.3543	14.69 ± 0.65	56.12	0.23	0.005 ± 0.000
14D10125	9.4 %		0.0839418	257.4730	0.000000	3.4571	18.0379	16.55 ± 0.78	42.10	0.22	0.006 ± 0.000
14D10126	10.4 %		0.1713573	206.2158	0.041770	3.1768	18.7111	18.67 ± 0.94	26.98	0.20	0.007 ± 0.000
14D10128	11.4 %		0.2874641	167.1724	0.017637	2.9134	20.1151	21.87 ± 1.25	19.15	0.18	0.007 ± 0.000
14D10129	12.7 %		0.3814625	152.2969	0.069269	2.7296	28.3601	32.81 ± 1.59	20.10	0.17	0.008 ± 0.000
14D10131	14.2 %		0.4244354	176.5144	0.046817	2.8716	34.0430	37.39 ± 1.68	21.35	0.18	0.007 ± 0.000
14D10132	16.2 %		0.4629201	200.9590	0.058609	3.0303	39.2323	40.79 ± 1.73	22.29	0.19	0.006 ± 0.000
14D10134	18.2 %		0.5136908	141.0710	0.038664	2.1982	35.0724	50.14 ± 2.57	18.77	0.14	0.007 ± 0.000
14D10135	21.2 %		0.6120045	125.1677	0.090246	1.9124	40.5419	66.32 ± 3.51	18.31	0.12	0.007 ± 0.000
14D10137	22.3 %		0.4184772	59.4514	0.094378	0.7939	28.6646	111.53 ± 10.35	18.82	0.05	0.006 ± 0.000
14D09889	1.7 %		0.8202143	18.6166	4.614500	65.5687	291.7218	14.12 ± 0.10	54.61	4.08	1.514 ± 0.037
14D09891	1.9 %		0.5562225	22.0584	4.426265	65.2372	298.3510	14.51 ± 0.08	64.47	4.06	1.272 ± 0.027
14D09892	2.1 %		0.3610432	22.3427	3.749754	56.5264	262.8690	14.76 ± 0.07	71.12	3.52	1.088 ± 0.023
14D09894	2.5 %	☒	0.3823248	49.5136	5.158045	82.9872	389.6632	14.90 ± 0.05	77.51	5.17	0.721 ± 0.008
14D09895	2.9 %	☒	0.2472552	49.5432	3.921480	67.2359	316.7367	14.95 ± 0.05	81.24	4.19	0.584 ± 0.007
14D09897	3.1 %	☒	0.1874359	57.6600	3.158262	60.4901	285.4700	14.98 ± 0.05	83.74	3.77	0.451 ± 0.005
14D09898	3.6 %	☒	0.3015754	191.9937	4.845016	123.5422	582.0096	14.95 ± 0.04	86.71	7.69	0.277 ± 0.002
14D09900	4.2 %	☒	0.2529907	285.9501	3.818480	138.2073	647.6667	14.87 ± 0.03	89.63	8.60	0.208 ± 0.001
14D09901	4.8 %		0.2064563	325.3291	2.401315	134.2251	623.7934	14.75 ± 0.03	91.07	8.36	0.177 ± 0.001
14D09903	5.6 %		0.1778149	381.7526	1.759565	149.5268	689.8104	14.64 ± 0.03	92.90	9.31	0.168 ± 0.001
14D09904	6.4 %		0.1563159	302.9561	1.116029	116.7898	536.8449	14.59 ± 0.03	92.06	7.27	0.166 ± 0.001
14D09906	7.4 %		0.0837904	189.9214	0.558411	70.4375	323.7918	14.59 ± 0.04	92.88	4.38	0.159 ± 0.001
14D09907	8.4 %		0.0980533	212.4949	0.488656	76.2580	348.8034	14.52 ± 0.04	92.31	4.75	0.154 ± 0.001
14D09909	9.4 %		0.0845285	198.3175	0.405125	68.6027	311.6992	14.42 ± 0.04	92.56	4.27	0.149 ± 0.001
14D09910	10.4 %		0.0832005	183.8782	0.345071	60.3509	271.9642	14.30 ± 0.05	91.69	3.76	0.141 ± 0.001
14D09912	11.4 %		0.0799087	169.3689	0.329628	53.2278	237.7443	14.18 ± 0.05	90.95	3.31	0.135 ± 0.001
14D09913	12.7 %		0.0869301	154.3572	0.231847	43.3115	190.3866	13.95 ± 0.06	88.09	2.70	0.121 ± 0.001
14D09915	14.2 %		0.2384518	242.3691	0.376008	55.5260	235.0547	13.44 ± 0.06	76.92	3.46	0.099 ± 0.001
14D09916	16.2 %		0.1719405	157.5203	0.164097	27.3294	116.8186	13.57 ± 0.11	69.68	1.70	0.075 ± 0.001
14D09918	18.2 %		0.4565635	162.4181	0.156005	21.6133	91.8195	13.49 ± 0.21	40.49	1.35	0.057 ± 0.000
14D09919	21.2 %		0.3075708	121.0714	0.037034	12.0781	53.1402	13.97 ± 0.30	36.89	0.75	0.043 ± 0.000
14D09921	22.3 %		0.1390156	60.9467	0.067697	5.7809	25.3110	13.90 ± 0.47	38.12	0.36	0.041 ± 0.001
		Σ	9.5695245	8188.0617	44.006035	1606.5206	7531.3216				

Information on Analysis
Sample = 4
Material = Plagioclase
Location = Nevada
Analyst = Dan Miggins
Project = NEVADA | WALKER (13-45)
Mass Discrimination Law = LIN
Irradiation = 14-OSU-01
J = 0.00176209 ± 0.00000180
FCT-NM = 28.020 ± 0.160 Ma

Results	40(r)/39(k) ± 2σ	Age ± 2σ (Ma)	MSWD	39Ar(k) (%,n)	K/Ca ± 2σ
Age Plateau	4.70211 ± 0.00780 ± 0.17%	14.92 ± 0.04 ± 0.26%	1.63 5%	31.19 18	0.004 ± 0.004
		Full External Error ± 0.38	1.69	2σ Confidence Limit	
		Analytical Error ± 0.02	1.2771	Error Magnification	
Total Fusion Age	4.68797 ± 0.00469 ± 0.10%	14.88 ± 0.03 ± 0.23%		44	0.084 ± 0.000
		Full External Error ± 0.38			
		Analytical Error ± 0.01			

004 PLG+GM.full.xls printed at 6/20/2014 (10:36 AM)
ArArCALC v2.6.2 -- Beta Version

Table 3: LP-7 – Plagioclase and Groundmass

OSU Argon Geochronology Lab
CEOAS Oregon State University, Corvallis, USA

Incremental Heating			36Ar(a) [fA]	37Ar(ca) [fA]	38Ar(cl) [fA]	39Ar(k) [fA]	40Ar(r) [fA]	Age ± 2σ (Ma)	40Ar(r) (%)	39Ar(k) (%)	K/Ca ± 2σ
14D10165	1.7 %		7.2832	4.0390	0.477616	0.7344	1.7103	7.41 ± 57.90	0.08	0.02	0.078 ± 0.013
14D10167	1.9 %		5.6343	3.0157	0.070562	0.5984	17.7206	97.02 ± 64.19	1.08	0.02	0.085 ± 0.018
14D10168	2.1 %		3.2493	1.4098	0.000000	0.2648	12.3281	154.96 ± 120.66	1.30	0.01	0.081 ± 0.038
14D10170	2.5 %		6.0007	4.9966	0.014554	0.7977	21.2431	87.01 ± 49.87	1.21	0.02	0.069 ± 0.010
14D10171	2.9 %		10.1941	11.5201	0.053279	1.7216	46.7296	88.73 ± 34.53	1.58	0.04	0.064 ± 0.004
14D10173	3.1 %		8.8613	9.9088	0.000000	1.4537	41.1287	92.58 ± 36.82	1.60	0.04	0.063 ± 0.005
14D10174	3.6 %		9.3863	12.0023	0.009066	1.7433	43.9576	82.28 ± 31.75	1.61	0.04	0.062 ± 0.004
14D10176	4.2 %		19.4893	44.7961	0.000000	6.1606	50.3114	26.24 ± 16.68	0.88	0.16	0.059 ± 0.001
14D10177	4.8 %		17.1457	35.7172	0.057932	5.0001	70.4391	45.51 ± 18.42	1.41	0.13	0.060 ± 0.001
14D10179	5.6 %		21.8613	61.9159	0.038802	8.4415	63.2880	24.08 ± 13.56	0.99	0.21	0.059 ± 0.001
14D10180	6.4 %		35.4951	131.4138	0.036018	17.6919	78.2644	14.17 ± 10.28	0.75	0.45	0.058 ± 0.001
14D10182	7.4 %		46.3931	164.8008	0.132525	21.9405	14.8339	2.16 ± 10.71	0.11	0.56	0.057 ± 0.000
14D10183	8.4 %		72.4363	225.2111	0.000000	30.2062	1524.0582	168.57 ± 13.44	7.67	0.76	0.058 ± 0.000
14D10185	9.4 %		91.9039	285.6911	0.000000	38.7063	1770.7493	152.16 ± 13.11	6.98	0.98	0.058 ± 0.000
14D10186	10.4 %		98.7430	310.7534	0.000000	42.8517	1797.3393	139.01 ± 12.58	6.56	1.08	0.059 ± 0.000
14D10188	11.4 %		116.7690	372.9356	0.000000	52.4036	1996.3291	125.80 ± 12.05	6.14	1.33	0.060 ± 0.000
14D10189	12.7 %		156.8192	511.5254	0.000000	74.9403	2532.7951	111.16 ± 11.18	5.78	1.90	0.063 ± 0.000
14D10191	14.2 %		132.7079	693.7148	0.000000	103.4671	1761.7134	55.15 ± 6.65	4.70	2.62	0.064 ± 0.000
14D10192	16.2 %		88.8153	639.0796	0.000000	94.4040	957.1885	32.64 ± 4.86	3.79	2.39	0.064 ± 0.000
14D10194	18.2 %		47.0779	436.7604	0.472399	63.1087	743.3241	37.19 ± 3.71	5.07	1.60	0.062 ± 0.000
14D10195	21.2 %		25.3732	387.2512	0.211544	55.7048	376.1619	21.41 ± 2.32	4.78	1.41	0.062 ± 0.000
14D10197	22.3 %		14.3201	161.3483	0.091115	22.4021	179.3483	25.36 ± 3.33	4.07	0.57	0.060 ± 0.000
14D09946	1.7 %		3.8707	1.0425	0.058248	4.2305	8.4884	6.39 ± 5.08	0.74	0.11	1.745 ± 0.804
14D09948	1.9 %		6.4241	2.4895	0.134697	9.0658	22.8655	8.03 ± 3.78	1.19	0.23	1.566 ± 0.304
14D09949	2.1 %		5.6286	2.2068	0.115637	7.9602	9.9997	4.00 ± 3.82	0.60	0.20	1.551 ± 0.328
14D09951	2.5 %		7.6938	4.0099	0.157647	13.4940	33.8510	7.98 ± 2.96	1.47	0.34	1.447 ± 0.172
14D09952	2.9 %		13.2148	9.2099	0.318079	31.9457	97.1818	9.68 ± 2.12	2.43	0.81	1.492 ± 0.080
14D09954	3.1 %		10.9083	8.7361	0.189579	31.4423	121.6975	12.30 ± 1.78	3.64	0.80	1.548 ± 0.085
14D09955	3.6 %		10.1103	9.1261	0.174614	32.7541	132.4336	12.85 ± 1.59	4.24	0.83	1.543 ± 0.084
14D09957	4.2 %		12.3457	14.8488	0.249826	53.3478	237.5367	14.15 ± 1.18	6.11	1.35	1.545 ± 0.050
14D09958	4.8 %		11.5488	18.0043	0.181668	66.7539	307.5906	14.64 ± 0.89	8.27	1.69	1.594 ± 0.041
14D09960	**5.6 %**	⊠	**13.4446**	**30.3053**	**0.272655**	**113.3191**	**571.9391**	**16.03 ± 0.61**	**12.58**	**2.87**	**1.608 ± 0.026**
14D09961	**6.4 %**	⊠	**11.8411**	**38.4928**	**0.270918**	**147.1007**	**745.4271**	**16.09 ± 0.41**	**17.56**	**3.72**	**1.643 ± 0.022**
14D09963	**7.4 %**	⊠	**11.6076**	**53.0197**	**0.248229**	**202.5296**	**1048.4777**	**16.44 ± 0.29**	**23.41**	**5.12**	**1.643 ± 0.018**
14D09964	**8.4 %**	⊠	**9.4622**	**51.7253**	**0.279120**	**206.2128**	**1052.2667**	**16.20 ± 0.24**	**27.34**	**5.22**	**1.714 ± 0.019**
14D09966	**9.4 %**	⊠	**9.0585**	**58.6534**	**0.263591**	**233.8386**	**1177.2663**	**15.99 ± 0.20**	**30.54**	**5.92**	**1.714 ± 0.017**
14D09967	10.4 %		7.7029	51.6155	0.255115	210.4583	1036.8829	15.65 ± 0.19	31.29	5.33	1.753 ± 0.020
14D09969	11.4 %		6.6598	47.4147	0.317821	194.6055	958.9242	15.65 ± 0.18	32.76	4.92	1.765 ± 0.021
14D09970	12.7 %		6.3322	45.6042	0.411259	188.0716	903.7781	15.26 ± 0.18	32.57	4.76	1.773 ± 0.021
14D09972	14.2 %		6.6480	48.0862	0.548239	205.1835	982.4968	15.21 ± 0.17	33.34	5.19	1.835 ± 0.022
14D09973	16.2 %		8.2019	59.0532	0.628295	257.6031	1209.7987	14.92 ± 0.17	33.29	6.52	1.876 ± 0.019
14D09975	18.2 %		10.4445	67.2364	0.953693	290.5471	1340.2872	14.66 ± 0.19	30.28	7.35	1.858 ± 0.017
14D09976	21.2 %		21.6970	106.4917	1.650228	428.4009	1945.2004	14.43 ± 0.26	23.28	10.84	1.730 ± 0.014
14D09978	22.3 %		26.1062	97.8874	1.843620	378.1897	1710.9019	14.37 ± 0.35	18.15	9.57	1.661 ± 0.013
		Σ	1266.9110	5335.0668	11.188189	3951.7985	4155.4194				

Information on Analysis
Sample = 7
Material = Plagioclase
Location = Nevada
Analyst = Dan Miggins
Project = NEVADA | WALKER (13-45)
Mass Discrimination Law = LIN
Irradiation = 14-OSU-01
J = 0.00176404 ± 0.00000243
FCT-NM = 28.020 ± 0.160 Ma

Results	40(r)/39(k) ± 2σ	Age ± 2σ (Ma)	MSWD	39Ar(k) (%,n)	K/Ca ± 2σ
Age Plateau	5.08371 ± 0.05246 ± 1.03%	16.14 ± 0.17 ± 1.06%	1.73	22.85	1.673 ± 0.041
		Full External Error ± 0.44	14%	5	
		Analytical Error ± 0.17	2.41	2σ Confidence Limit	
			1.3140	Error Magnification	
Total Fusion Age	1.05153 ± 0.12567 ± 11.95%	3.35 ± 0.40 ± 11.94%		44	0.319 ± 0.001
		Full External Error ± 0.41			
		Analytical Error ± 0.40			

007 PLG+GM.full.xls printed at 6/20/2014 (10:43 AM)
ArArCALC v2.6.2 -- Beta Version

Table 4: LP-9 – Plagioclase and Groundmass

OSU Argon Geochronology Lab
CEOAS Oregon State University, Corvallis, USA

Incremental Heating			36Ar(a) [fA]	37Ar(ca) [fA]	38Ar(cl) [fA]	39Ar(k) [fA]	40Ar(r) [fA]	Age ± 2σ (Ma)	40Ar(r) (%)	39Ar(k) (%)	K/Ca ± 2σ
14D10258	1.7 %		1.653210	27.674	0.1038364	0.4151	16.238	121.49 ± 32.44	3.22	0.01	0.006 ± 0.001
14D10260	1.9 %		0.454146	34.070	0.0422252	0.4537	4.174	29.31 ± 10.36	3.02	0.01	0.006 ± 0.001
14D10261	2.1 %		0.101380	17.207	0.0000000	0.2443	1.724	22.53 ± 12.38	5.44	0.01	0.006 ± 0.002
14D10263	2.5 %		0.221928	52.038	0.0000000	0.6945	8.199	37.53 ± 5.97	11.11	0.02	0.006 ± 0.001
14D10264	2.9 %		0.228744	161.461	0.0000000	1.9172	15.859	26.38 ± 1.97	19.00	0.04	0.005 ± 0.000
14D10266	3.1 %		0.070945	107.100	0.0000000	1.1946	8.074	21.58 ± 2.38	27.80	0.03	0.005 ± 0.000
14D10267	3.6 %	☒	0.154087	275.199	0.0010597	3.0507	20.398	21.35 ± 1.11	30.94	0.07	0.005 ± 0.000
14D10269	4.2 %	☒	0.079945	279.104	0.0000000	3.0076	20.678	21.95 ± 1.05	46.67	0.07	0.005 ± 0.000
14D10270	4.8 %	☒	0.068523	579.468	0.0281557	6.2120	37.556	19.32 ± 0.54	64.96	0.14	0.005 ± 0.000
14D10272	5.6 %	☒	0.066222	791.645	0.0235031	8.8001	56.570	20.53 ± 0.44	74.29	0.20	0.005 ± 0.000
14D10273	6.4 %	☒	0.040761	821.039	0.0000000	9.4351	54.993	18.63 ± 0.40	82.02	0.21	0.005 ± 0.000
14D10275	7.4 %	☒	0.044126	926.164	0.0658928	11.0144	66.424	19.27 ± 0.36	83.58	0.25	0.005 ± 0.000
14D10276	8.4 %	☒	0.039529	974.153	0.0530316	12.4606	79.684	20.43 ± 0.31	87.20	0.28	0.006 ± 0.000
14D10278	9.4 %		0.031484	872.545	0.0000000	12.3098	95.553	24.76 ± 0.32	91.12	0.27	0.006 ± 0.000
14D10279	10.4 %		0.032560	713.950	0.0000000	10.6548	104.798	31.32 ± 0.37	91.58	0.24	0.006 ± 0.000
14D10281	11.4 %		0.039300	520.767	0.0200676	8.1660	122.123	47.41 ± 0.54	91.31	0.18	0.007 ± 0.000
14D10282	12.7 %		0.051678	421.327	0.0506789	7.3984	252.095	106.27 ± 1.05	94.29	0.17	0.008 ± 0.000
14D10284	14.2 %		0.073274	377.518	0.0789036	8.9695	294.692	102.57 ± 0.85	93.15	0.20	0.010 ± 0.000
14D10285	16.2 %		0.099252	357.946	0.1150170	7.2814	99.546	43.39 ± 0.60	77.24	0.16	0.009 ± 0.000
14D10287	18.2 %		0.155175	725.403	0.1834525	14.4637	147.929	32.56 ± 0.29	76.33	0.32	0.009 ± 0.000
14D10288	21.2 %		0.079555	553.433	0.0451409	8.9458	79.443	28.30 ± 0.43	77.16	0.20	0.007 ± 0.000
14D10290	22.3 %		0.066229	248.081	0.0000000	3.6283	27.955	24.58 ± 0.88	58.82	0.08	0.006 ± 0.000
14D09980	1.7 %		0.633475	4.216	0.0951077	15.5412	22.943	4.74 ± 0.34	10.92	0.35	1.585 ± 0.209
14D09982	1.9 %		0.614791	5.024	0.1335401	18.7428	29.754	5.09 ± 0.29	14.07	0.42	1.604 ± 0.173
14D09983	2.1 %		0.657155	7.766	0.2241030	22.8545	42.310	5.94 ± 0.23	17.89	0.51	1.266 ± 0.094
14D09985	2.5 %		0.782411	14.289	0.2382026	31.9274	81.339	8.17 ± 0.20	26.02	0.71	0.961 ± 0.039
14D09986	2.9 %		0.708057	19.038	0.1841671	33.6304	107.439	10.23 ± 0.17	33.92	0.75	0.760 ± 0.023
14D09988	3.1 %		0.471022	12.968	0.1203152	20.9494	74.518	11.39 ± 0.22	34.87	0.47	0.695 ± 0.032
14D09989	3.6 %		0.570686	25.688	0.1291444	35.6590	143.575	12.89 ± 0.15	45.98	0.80	0.597 ± 0.014
14D09991	4.2 %		0.586529	43.022	0.2373212	54.5613	245.604	14.40 ± 0.10	58.62	1.22	0.545 ± 0.008
14D09992	4.8 %		0.650167	83.116	0.2191313	100.8064	486.494	15.44 ± 0.06	71.68	2.25	0.522 ± 0.005
14D09994	5.6 %		0.608054	135.550	0.2175484	165.8147	827.437	15.96 ± 0.04	82.15	3.70	0.526 ± 0.004
14D09995	6.4 %		0.490138	137.044	0.2467122	175.7910	876.317	15.94 ± 0.04	85.80	3.92	0.552 ± 0.004
14D09997	7.4 %		0.572012	210.752	0.1650449	280.0205	1381.234	15.78 ± 0.03	89.08	6.25	0.571 ± 0.004
14D09998	8.4 %		0.612701	256.856	0.2989367	361.5381	1754.130	15.52 ± 0.03	90.63	8.07	0.605 ± 0.004
14D10000	9.4 %		0.632148	271.251	0.2460243	405.6028	1937.318	15.28 ± 0.02	91.19	9.05	0.643 ± 0.004
14D10001	10.4 %		0.655701	263.196	0.3351983	410.2727	1934.254	15.08 ± 0.02	90.88	9.16	0.670 ± 0.004
14D10003	11.4 %		0.707116	238.569	0.4238529	380.1334	1778.199	14.96 ± 0.03	89.47	8.49	0.685 ± 0.005
14D10004	12.7 %		0.883010	240.847	0.4565646	379.2726	1762.082	14.86 ± 0.03	87.09	8.47	0.677 ± 0.005
14D10006	14.2 %	☒	1.170531	240.612	0.6362316	369.0573	1708.092	14.81 ± 0.03	83.14	8.24	0.660 ± 0.004
14D10007	16.2 %	☒	1.652030	228.910	0.8246064	344.0137	1589.269	14.78 ± 0.04	76.49	7.68	0.646 ± 0.004
14D10009	18.2 %	☒	2.471690	193.053	1.0324875	295.0096	1360.022	14.75 ± 0.05	65.05	6.59	0.657 ± 0.005
14D10010	21.2 %	☒	3.292338	178.776	1.4581076	280.7701	1299.702	14.81 ± 0.07	57.18	6.27	0.675 ± 0.005
14D10012	22.3 %	☒	2.363387	97.075	0.9122923	157.2857	732.401	14.90 ± 0.09	51.18	3.51	0.697 ± 0.006
		Σ	25.637204	12744.908	9.6456054	4479.9723	21789.137				

Information on Analysis
Sample = 9
Material = Plagioclase
Location = Nevada
Analyst = Dan Miggins
Project = NEVADA | WALKER (13-45)
Mass Discrimination Law = LIN
Irradiation = 14-OSU-01
J = 0.00177639 ± 0.00000247
FCT-NM = 28.020 ± 0.160 Ma

Results	40(r)/39(k) ± 2σ	Age ± 2σ (Ma)	MSWD	39Ar(k) (%,n)	K/Ca ± 2σ
Age Plateau	4.64542 ± 0.11032	14.86 ± 0.35	> 100	33.48	0.005 ± 0.004
Error Mean	± 2.37%	± 2.38%	0%	12	
		Full External Error ± 0.52	1.85	2σ Confidence Limit	
		Analytical Error ± 0.35	> 10	Error Magnification	
Total Fusion Age	4.86368 ± 0.00343	15.56 ± 0.04		44	0.151 ± 0.000
	± 0.07%	± 0.29%			
		Full External Error ± 0.39			
		Analytical Error ± 0.01			

009 PLG+GM.full.xls printed at 6/20/2014 (10:40 AM)
ArArCALC v2.6.2 -- Beta Version

Table 5: LP-10 – Plagioclase and Groundmass

OSU Argon Geochronology Lab
CEOAS Oregon State University, Corvallis, USA

Incremental Heating			36Ar(a) [fA]	37Ar(ca) [fA]	38Ar(cl) [fA]	39Ar(k) [fA]	40Ar(r) [fA]	Age ± 2σ (Ma)	40Ar(r) (%)	39Ar(k) (%)	K/Ca ± 2σ
14D11725	1.7 %		6.376425	53.016	0.062846	0.6669	34.511	155.81 ± 50.09	1.80	0.03	0.005 ± 0.001
14D11727	1.9 %		1.812290	49.727	0.000000	0.6128	5.663	28.83 ± 17.96	1.05	0.03	0.005 ± 0.001
14D11728	2.1 %		1.055165	49.099	0.016771	0.5840	9.065	48.16 ± 13.71	2.83	0.02	0.005 ± 0.001
14D11729	2.5 %		2.253797	116.089	0.000000	1.3401	16.460	38.22 ± 9.77	2.41	0.06	0.005 ± 0.000
14D11730	2.9 %		2.231046	186.530	0.010555	2.1402	17.754	25.90 ± 6.30	2.62	0.09	0.005 ± 0.000
14D11732	3.1 %	☒	1.075463	167.742	0.000000	1.9005	9.995	16.46 ± 4.12	3.05	0.08	0.005 ± 0.000
14D11733	3.6 %	☒	1.004834	205.607	0.014818	2.3226	12.855	17.32 ± 3.31	4.15	0.10	0.005 ± 0.000
14D11735	4.2 %	☒	2.092859	314.990	0.000000	3.4921	21.850	19.57 ± 3.62	3.41	0.15	0.005 ± 0.000
14D11736	4.8 %	☒	2.037441	439.496	0.056508	4.9762	29.257	18.39 ± 2.61	4.63	0.21	0.005 ± 0.000
14D11738	5.6 %	☒	2.224865	674.631	0.020506	7.7408	43.058	17.41 ± 1.81	6.15	0.33	0.005 ± 0.000
14D11739	6.4 %	☒	1.530824	784.278	0.047060	9.3642	48.158	16.10 ± 1.17	9.62	0.40	0.005 ± 0.000
14D11741	7.4 %	☒	1.317170	881.900	0.038754	10.8601	57.384	16.54 ± 0.91	12.85	0.46	0.005 ± 0.000
14D11742	8.4 %	☒	0.931762	935.954	0.022004	12.0475	58.044	15.09 ± 0.66	17.41	0.51	0.006 ± 0.000
14D11744	9.4 %	☒	0.450978	823.251	0.032921	10.8726	53.586	15.43 ± 0.52	28.68	0.46	0.006 ± 0.000
14D11745	10.4 %	☒	0.367230	696.046	0.014055	9.8968	49.696	15.72 ± 0.52	31.41	0.42	0.006 ± 0.000
14D11747	11.4 %	☒	0.226814	620.402	0.028202	9.3221	45.398	15.25 ± 0.47	40.38	0.40	0.006 ± 0.000
14D11748	12.7 %		0.144327	543.775	0.084297	8.9121	47.369	16.64 ± 0.45	52.62	0.38	0.007 ± 0.000
14D11750	14.2 %		0.202812	521.939	0.052578	9.2800	48.200	16.26 ± 0.43	44.57	0.40	0.008 ± 0.000
14D11751	16.2 %		0.213309	491.256	0.049944	9.1945	49.674	16.91 ± 0.46	44.07	0.39	0.008 ± 0.000
14D11753	18.2 %		0.199786	412.060	0.058101	8.3327	49.713	18.66 ± 0.50	45.71	0.35	0.009 ± 0.000
14D11754	21.2 %		0.203906	467.930	0.035169	8.6997	54.886	19.73 ± 0.48	47.67	0.37	0.008 ± 0.000
14D11756	22.3 %		0.140246	246.342	0.064404	4.9947	29.118	18.24 ± 0.70	41.26	0.21	0.009 ± 0.000
14D11625	1.7 %		0.983247	11.215	3.370620	36.9229	144.025	12.23 ± 0.18	33.14	1.57	1.416 ± 0.084
14D11627	1.9 %		0.962616	13.903	3.665430	40.9494	166.367	12.73 ± 0.17	36.90	1.74	1.267 ± 0.060
14D11628	2.1 %		0.599237	8.348	2.289993	25.7540	104.299	12.69 ± 0.20	37.06	1.10	1.327 ± 0.101
14D11630	2.5 %		1.149267	28.632	5.066451	62.1351	263.112	13.27 ± 0.13	43.65	2.65	0.933 ± 0.021
14D11631	2.9 %		1.091070	38.735	5.328529	69.2916	301.542	13.63 ± 0.11	48.32	2.95	0.769 ± 0.014
14D11633	3.1 %		0.985076	49.223	5.334347	73.6961	332.409	14.13 ± 0.10	53.31	3.14	0.644 ± 0.010
14D11634	3.6 %		0.710455	42.153	3.855673	57.7758	264.027	14.31 ± 0.10	55.70	2.46	0.589 ± 0.010
14D11636	4.2 %		0.863013	86.586	5.020377	88.2526	411.926	14.62 ± 0.08	61.75	3.76	0.438 ± 0.004
14D11637	4.8 %		0.908168	154.683	5.495248	122.7713	583.033	14.87 ± 0.06	68.47	5.23	0.341 ± 0.003
14D11639	5.6 %	☒	0.933704	268.229	5.604400	175.0383	839.234	15.01 ± 0.05	75.25	7.45	0.281 ± 0.002
14D11640	6.4 %	☒	0.650215	245.765	3.607257	148.2480	712.502	15.05 ± 0.04	78.75	6.31	0.259 ± 0.002
14D11642	7.4 %	☒	0.637881	355.427	3.363609	198.3795	949.881	15.00 ± 0.04	83.43	8.45	0.240 ± 0.002
14D11643	8.4 %		0.515943	368.731	2.351169	202.1818	962.966	14.92 ± 0.03	86.32	8.61	0.236 ± 0.002
14D11645	9.4 %		0.415936	348.966	1.676661	192.5278	913.672	14.86 ± 0.03	88.13	8.20	0.237 ± 0.002
14D11646	10.4 %		0.314481	275.701	1.142786	153.9217	726.519	14.78 ± 0.03	88.64	6.55	0.240 ± 0.002
14D11648	11.4 %		0.257173	229.936	0.824425	126.5047	594.982	14.73 ± 0.04	88.66	5.39	0.237 ± 0.002
14D11649	12.7 %		0.240898	199.106	0.719904	106.4880	498.426	14.66 ± 0.04	87.49	4.53	0.230 ± 0.002
14D11651	14.2 %		0.215381	179.768	0.546865	89.1680	414.930	14.57 ± 0.04	86.68	3.80	0.213 ± 0.002
14D11652	16.2 %		0.245995	197.174	0.524185	82.5974	380.280	14.42 ± 0.05	83.94	3.52	0.180 ± 0.001
14D11654	18.2 %		0.238479	197.413	0.426605	68.5272	312.221	14.27 ± 0.06	81.57	2.92	0.149 ± 0.001
14D11655	21.2 %		0.233083	209.151	0.394616	58.4820	265.323	14.21 ± 0.07	79.38	2.49	0.120 ± 0.001
14D11657	22.3 %		0.150909	124.745	0.133980	30.9964	142.635	14.41 ± 0.11	76.17	1.32	0.107 ± 0.001
		Σ	41.395577	13315.652	61.452623	2348.1631	11076.007				

Information on Analysis
Sample = 10
Material = Plagioclase
Location = Nevada
Analyst = Dan Miggins
Project = NEVADA | WALKER (13-45)
Mass Discrimination Law = LIN
Irradiation = 14-OSU-01
J = 0.00173902 ± 0.00000176
FCT-NM = 28.020 ± 0.160 Ma

Results	40(r)/39(k) ± 2σ		Age ± 2σ (Ma)		MSWD	39Ar(k) (%,n)	K/Ca ± 2σ
Age Plateau	4.79668	± 0.01515	15.02	± 0.06	3.97	25.74	0.006 ± 0.003
Error Mean		± 0.32%		± 0.37%	0%	14	
			Full External Error	± 0.38	1.78	2σ Confidence Limit	
			Analytical Error	± 0.05	1.9917	Error Magnification	
Total Fusion Age	4.71688	± 0.00817	14.77	± 0.04		44	0.076 ± 0.000
		± 0.17%		± 0.26%			
			Full External Error	± 0.37			
			Analytical Error	± 0.03			

010 PLG+GM.full.xls printed at 6/20/2014 (10:45 AM)
ArArCALC v2.6.2 -- Beta Version

Table 6: LP-12 – Plagioclase and Groundmass

OSU Argon Geochronology Lab
CEOAS Oregon State University, Corvallis, USA

Incremental Heating			36Ar(a) [fA]	37Ar(ca) [fA]	38Ar(cl) [fA]	39Ar(k) [fA]	40Ar(r) [fA]	Age ± 2σ (Ma)	40Ar(r) (%)	39Ar(k) (%)	K/Ca ± 2σ
14D10199	1.7 %		12.780177	46.8600	0.16302	5.5442	2.858	1.67 ± 12.03	0.08	0.08	0.051 ± 0.001
14D10201	1.9 %		0.743806	5.4304	0.00781	0.9959	2.925	9.46 ± 6.14	1.31	0.01	0.079 ± 0.009
14D10202	2.1 %		0.556575	5.8439	0.03476	0.9954	2.055	6.65 ± 5.32	1.23	0.01	0.073 ± 0.008
14D10204	2.5 %		1.605605	12.8215	0.09993	1.9951	8.006	12.91 ± 5.18	1.66	0.03	0.067 ± 0.003
14D10205	2.9 %		0.936502	26.6088	0.04891	4.0434	14.081	11.21 ± 1.67	4.84	0.06	0.065 ± 0.002
14D10207	3.1 %		0.341202	21.3111	0.02832	3.3505	14.413	13.84 ± 1.35	12.51	0.05	0.068 ± 0.002
14D10208	3.6 %		0.373336	22.0712	0.00479	3.4160	13.705	12.91 ± 1.30	11.05	0.05	0.067 ± 0.002
14D10210	4.2 %	⊠	0.350471	36.5719	0.02538	5.6412	25.143	14.33 ± 0.82	19.53	0.08	0.066 ± 0.001
14D10211	4.8 %	⊠	0.326666	61.3592	0.07443	9.5549	42.711	14.37 ± 0.49	30.67	0.14	0.067 ± 0.001
14D10213	5.6 %	⊠	0.166826	92.7212	0.05769	14.8536	65.510	14.18 ± 0.26	57.05	0.22	0.069 ± 0.001
14D10214	6.4 %	⊠	0.071300	179.7306	0.06767	28.9559	128.682	14.29 ± 0.13	85.91	0.43	0.069 ± 0.001
14D10216	7.4 %	⊠	0.040900	239.6679	0.01934	38.2169	170.956	14.39 ± 0.10	93.38	0.57	0.069 ± 0.000
14D10217	8.4 %	⊠	0.032422	365.6760	0.10151	57.6186	257.462	14.37 ± 0.07	96.39	0.86	0.068 ± 0.000
14D10219	9.4 %	⊠	0.036388	436.9609	0.09478	68.4291	306.459	14.40 ± 0.06	96.59	1.02	0.067 ± 0.000
14D10220	10.4 %	⊠	0.024928	471.4645	0.10353	74.3440	332.074	14.36 ± 0.05	97.81	1.11	0.068 ± 0.000
14D10222	11.4 %	⊠	0.018035	504.1631	0.08460	79.3564	355.349	14.40 ± 0.05	98.50	1.18	0.068 ± 0.000
14D10223	12.7 %	⊠	0.014383	549.3045	0.08047	87.0435	390.147	14.41 ± 0.05	98.90	1.30	0.068 ± 0.000
14D10225	14.2 %	⊠	0.024646	551.6532	0.17653	88.4075	396.667	14.43 ± 0.05	98.18	1.32	0.069 ± 0.000
14D10226	16.2 %	⊠	0.038468	502.3027	0.15442	79.5057	357.372	14.45 ± 0.05	96.90	1.19	0.068 ± 0.000
14D10228	18.2 %	⊠	0.029546	356.0057	0.08583	55.4164	248.826	14.44 ± 0.07	96.59	0.83	0.067 ± 0.000
14D10229	21.2 %	⊠	0.010309	280.9668	0.05401	44.2526	199.009	14.46 ± 0.08	98.47	0.66	0.068 ± 0.000
14D10231	22.3 %	⊠	0.008180	152.6084	0.04915	23.5317	105.499	14.42 ± 0.14	97.74	0.35	0.066 ± 0.001
14D10071	1.7 %		1.324482	4.2879	1.83233	61.0077	207.390	10.94 ± 0.14	34.63	0.91	6.118 ± 0.671
14D10073	1.9 %		1.244133	4.2780	2.07538	68.2112	254.859	12.02 ± 0.13	40.94	1.02	6.856 ± 0.766
14D10074	2.1 %		1.474985	6.5494	3.14210	105.8773	422.308	12.83 ± 0.10	49.20	1.58	6.951 ± 0.520
14D10076	2.5 %		1.141235	6.2806	3.10502	105.0565	437.396	13.39 ± 0.08	56.46	1.57	7.193 ± 0.553
14D10077	2.9 %		1.641060	10.8033	5.86699	195.4098	840.329	13.83 ± 0.06	63.40	2.91	7.778 ± 0.359
14D10079	3.1 %		0.858438	8.0861	4.02638	135.9297	593.419	14.04 ± 0.06	70.04	2.03	7.228 ± 0.450
14D10080	3.6 %		1.057821	10.5223	5.65737	191.2740	842.342	14.16 ± 0.05	72.92	2.85	7.816 ± 0.360
14D10082	4.2 %	⊠	1.156375	13.8525	7.15201	248.7336	1104.438	14.28 ± 0.04	76.36	3.71	7.721 ± 0.273
14D10083	4.8 %	⊠	1.330495	18.4166	8.29819	299.9693	1335.238	14.31 ± 0.04	77.24	4.47	7.004 ± 0.192
14D10085	5.6 %	⊠	1.949196	28.3950	10.85891	404.4221	1800.934	14.32 ± 0.04	75.76	6.03	6.124 ± 0.116
14D10086	6.4 %	⊠	2.830991	43.7227	12.48541	501.4700	2236.962	14.35 ± 0.04	72.77	7.48	4.932 ± 0.061
14D10088	7.4 %	⊠	3.324699	50.5773	11.12775	482.6461	2144.337	14.29 ± 0.04	68.57	7.19	4.103 ± 0.048
14D10089	8.4 %	⊠	3.898349	62.7303	10.23534	487.2839	2155.781	14.23 ± 0.05	65.16	7.26	3.340 ± 0.034
14D10091	9.4 %	⊠	4.178017	75.1003	9.23866	481.8455	2143.325	14.30 ± 0.05	63.44	7.18	2.759 ± 0.025
14D10092	10.4 %	⊠	3.895927	74.6436	7.24337	421.9928	1878.156	14.31 ± 0.06	61.99	6.29	2.431 ± 0.022
14D10094	11.4 %	⊠	3.562299	72.2875	6.14005	369.7919	1648.703	14.34 ± 0.06	61.02	5.51	2.200 ± 0.021
14D10095	12.7 %	⊠	3.210836	65.9632	5.20282	317.9141	1418.111	14.34 ± 0.06	59.91	4.74	2.072 ± 0.020
14D10097	14.2 %	⊠	2.938695	61.1770	4.62832	279.6729	1249.578	14.37 ± 0.06	58.99	4.17	1.966 ± 0.020
14D10098	16.2 %	⊠	2.651527	55.0558	4.07438	240.5276	1075.198	14.38 ± 0.07	57.84	3.59	1.879 ± 0.020
14D10100	18.2 %	⊠	2.305432	47.3154	3.29324	196.3391	876.929	14.36 ± 0.08	56.27	2.93	1.784 ± 0.022
14D10101	21.2 %	⊠	2.251757	47.8081	3.10376	188.2132	835.776	14.28 ± 0.08	55.67	2.81	1.693 ± 0.020
14D10103	22.3 %	⊠	1.935486	35.6947	2.49090	149.1861	663.048	14.29 ± 0.08	53.68	2.22	1.797 ± 0.027
		Σ	68.692906	5725.6512	132.89557	6708.2429	29598.751				

Information on Analysis
Sample = 12
Material = Plagioclase
Location = Nevada
Analyst = Dan Miggins
Project = NEVADA | WALKER (13-45)
Mass Discrimination Law = LIN
Irradiation = 14-OSU-01
J = 0.00178543 ± 0.00000248
FCT-NM = 28.020 ± 0.160 Ma

Results	40(r)/39(k) ± 2σ	Age ± 2σ (Ma)	MSWD	39Ar(k) (%,n)	K/Ca ± 2σ
Age Plateau	4.46047 ± 0.00672	14.34 ± 0.05	4.20	86.84	0.069 ± 0.015
Error Mean	± 0.15%	± 0.31%	0%	30	
		Full External Error ± 0.36	1.53	2σ Confidence Limit	
		Analytical Error ± 0.02	2.0504	Error Magnification	
Total Fusion Age	4.41230 ± 0.00474	14.19 ± 0.04		44	0.504 ± 0.001
	± 0.11%	± 0.30%			
		Full External Error ± 0.36			
		Analytical Error ± 0.02			

012 PLG+GM.full.xls printed at 6/20/2014 (10:38 AM)
ArArCALC v2.6.2 -- Beta Version

Table 7: LP-4 - Groundmass

OSU Argon Geochronology Lab
CEOAS Oregon State University, Corvallis, USA

Incremental Heating			36Ar(a) [fA]	37Ar(ca) [fA]	38Ar(cl) [fA]	39Ar(k) [fA]	40Ar(r) [fA]	Age ± 2σ (Ma)	40Ar(r) (%)	39Ar(k) (%)	K/Ca ± 2σ
14D09889	1.7 %		0.8191984	18.5171	4.590031	65.2183	292.0300	14.14 ± 0.10	54.67	4.22	1.514 ± 0.037
14D09891	1.9 %		0.5555303	21.9405	4.402742	64.8886	298.5626	14.52 ± 0.08	64.51	4.20	1.272 ± 0.027
14D09892	2.1 %		0.3605911	22.2233	3.729801	56.2244	263.0082	14.77 ± 0.07	71.16	3.64	1.088 ± 0.023
14D09894	2.5 %	⊠	0.3818376	49.2490	5.130573	82.5438	389.8147	14.91 ± 0.05	77.54	5.34	0.721 ± 0.008
14D09895	2.9 %	⊠	0.2469343	49.2785	3.900585	66.8767	316.8373	14.95 ± 0.05	81.27	4.32	0.584 ± 0.007
14D09897	3.1 %	⊠	0.1871862	57.3518	3.141432	60.1668	285.5490	14.98 ± 0.05	83.76	3.89	0.451 ± 0.005
14D09898	3.6 %	⊠	0.3011415	190.9678	4.819207	122.8820	582.1479	14.95 ± 0.04	86.72	7.95	0.277 ± 0.002
14D09900	4.2 %	⊠	0.2525864	284.4221	3.798151	137.4688	647.7971	14.87 ± 0.03	89.65	8.89	0.208 ± 0.001
14D09901	4.8 %		0.2060967	323.5907	2.388551	133.5078	623.9100	14.75 ± 0.03	91.09	8.63	0.177 ± 0.001
14D09903	5.6 %		0.1774725	379.7126	1.750227	148.7278	689.9227	14.64 ± 0.03	92.92	9.62	0.168 ± 0.001
14D09904	6.4 %		0.1560256	301.3372	1.110120	116.1657	536.9395	14.59 ± 0.03	92.07	7.51	0.166 ± 0.001
14D09906	7.4 %		0.0836259	188.9065	0.555458	70.0611	323.8456	14.59 ± 0.04	92.89	4.53	0.159 ± 0.001
14D09907	8.4 %		0.0978639	211.3594	0.486081	75.8505	348.8651	14.52 ± 0.04	92.33	4.90	0.154 ± 0.001
14D09909	9.4 %		0.0843604	197.2578	0.402991	68.2361	311.7540	14.42 ± 0.04	92.58	4.41	0.149 ± 0.001
14D09910	10.4 %		0.0830387	182.8956	0.343257	60.0284	272.0165	14.31 ± 0.05	91.71	3.88	0.141 ± 0.001
14D09912	11.4 %		0.0797556	168.4638	0.327895	52.9434	237.7935	14.18 ± 0.05	90.96	3.42	0.135 ± 0.001
14D09913	12.7 %		0.0867732	153.5323	0.230637	43.0801	190.4362	13.96 ± 0.06	88.12	2.79	0.121 ± 0.001
14D09915	14.2 %		0.2380801	241.0740	0.374068	55.2293	235.1692	13.45 ± 0.06	76.96	3.57	0.099 ± 0.001
14D09916	16.2 %		0.1716780	156.6786	0.163270	27.1834	116.8987	13.58 ± 0.11	69.72	1.76	0.075 ± 0.001
14D09918	18.2 %		0.4559492	161.5502	0.155286	21.4978	92.0044	13.51 ± 0.21	40.57	1.39	0.057 ± 0.000
14D09919	21.2 %		0.3071533	120.4244	0.036914	12.0136	53.2657	14.00 ± 0.30	36.98	0.78	0.043 ± 0.000
14D09921	22.3 %		0.1388249	60.6211	0.067370	5.7500	25.3683	13.93 ± 0.47	38.21	0.37	0.041 ± 0.001
		Σ	5.4717039	3541.3542	41.904646	1546.5442	7133.9362				

Information on Analysis
Sample = 4
Material = Groundmass
Location = Nevada
Analyst = Dan Miggins
Project = NEVADA | WALKER (13-45)
Mass Discrimination Law = LIN
Irradiation = 14-OSU-01
J = 0.00175267 ± 0.00000179
FCT-NM = 28.020 ± 0.160 Ma

Results	40(r)/39(k) ± 2σ		Age ± 2σ (Ma)		MSWD	39Ar(k) (%,n)	K/Ca ± 2σ
Age Plateau	4.72845	± 0.01280	14.92	± 0.05	4.34	30.39	0.258 ± 0.097
Error Mean		± 0.27%		± 0.34%	0%	5	
			Full External Error	± 0.38	2.41	2σ Confidence Limit	
			Analytical Error	± 0.04	2.0823	Error Magnification	
Total Fusion Age	4.61282	± 0.00374	14.56	± 0.03		22	0.188 ± 0.000
		± 0.08%		± 0.22%			
			Full External Error	± 0.37			
			Analytical Error	± 0.01			

14D09888.full.xls printed at 6/20/2014 (10:47 AM)
ArArCALC v2.6.2 -- Beta Version

Table 8: LP-7 - Groundmass

OSU Argon Geochronology Lab
CEOAS Oregon State University, Corvallis, USA

Incremental Heating			36Ar(a) [fA]	37Ar(ca) [fA]	38Ar(cl) [fA]	39Ar(k) [fA]	40Ar(r) [fA]	Age ± 2σ (Ma)	40Ar(r) (%)	39Ar(k) (%)	K/Ca ± 2σ
14D09946	1.7 %		3.86683	1.04700	0.0592210	4.2488	9.644	7.26 ± 5.07	0.84	0.13	1.74 ± 0.80
14D09948	1.9 %		6.41770	2.50026	0.1364749	9.1049	24.784	8.70 ± 3.77	1.29	0.27	1.57 ± 0.30
14D09949	2.1 %		5.62300	2.21633	0.1171843	7.9945	11.680	4.67 ± 3.81	0.70	0.24	1.55 ± 0.33
14D09951	2.5 %		7.68615	4.02722	0.1597604	13.5522	36.148	8.53 ± 2.95	1.57	0.41	1.45 ± 0.17
14D09952	2.9 %		13.20157	9.24959	0.3219131	32.0833	101.129	10.07 ± 2.12	2.53	0.97	1.49 ± 0.08
14D09954	3.1 %		10.89741	8.77371	0.1924297	31.5778	124.956	12.63 ± 1.78	3.74	0.95	1.55 ± 0.09
14D09955	3.6 %		10.10022	9.16542	0.1772514	32.8952	135.454	13.14 ± 1.58	4.34	0.99	1.54 ± 0.08
14D09957	4.2 %		12.33342	14.91278	0.2532040	53.5777	241.226	14.37 ± 1.18	6.21	1.61	1.54 ± 0.05
14D09958	4.8 %		11.53729	18.08187	0.1846045	67.0414	311.043	14.80 ± 0.88	8.36	2.02	1.59 ± 0.04
14D09960	5.6 %	⊠	13.43119	30.43584	0.2763374	113.8073	575.962	16.14 ± 0.60	12.67	3.43	1.61 ± 0.03
14D09961	6.4 %	⊠	11.82931	38.65861	0.2742943	147.7344	748.974	16.17 ± 0.41	17.64	4.45	1.64 ± 0.02
14D09963	7.4 %	⊠	11.59597	53.24813	0.2514651	203.4021	1051.960	16.49 ± 0.29	23.49	6.12	1.64 ± 0.02
14D09964	8.4 %	⊠	9.45271	51.94814	0.2820890	207.1011	1055.109	16.25 ± 0.24	27.42	6.24	1.71 ± 0.02
14D09966	9.4 %	⊠	9.04948	58.90603	0.2664178	234.8459	1179.990	16.03 ± 0.20	30.61	7.07	1.71 ± 0.02
14D09967	10.4 %		7.69518	51.83781	0.2576522	211.3649	1039.200	15.68 ± 0.19	31.36	6.36	1.75 ± 0.02
14D09969	11.4 %		6.65312	47.61896	0.3204337	195.4438	960.928	15.68 ± 0.18	32.83	5.88	1.76 ± 0.02
14D09970	12.7 %		6.32591	45.80066	0.4142135	188.8818	905.683	15.30 ± 0.18	32.64	5.69	1.77 ± 0.02
14D09972	14.2 %		6.64140	48.29338	0.5518423	206.0674	984.498	15.24 ± 0.17	33.40	6.20	1.83 ± 0.02
14D09973	16.2 %		8.19374	59.30757	0.6325339	258.7128	1212.267	14.95 ± 0.17	33.36	7.79	1.88 ± 0.02
14D09975	18.2 %		10.43410	67.52605	0.9597519	291.7987	1343.427	14.69 ± 0.19	30.35	8.79	1.86 ± 0.02
14D09976	21.2 %		21.67531	106.95048	1.6613869	430.2463	1951.710	14.47 ± 0.25	23.35	12.95	1.73 ± 0.01
14D09978	22.3 %		26.08012	98.30903	1.8564337	379.8188	1718.725	14.44 ± 0.35	18.23	11.44	1.66 ± 0.01
		Σ	230.72114	828.81486	9.6068952	3321.3009	15724.499				

Information on Analysis
Sample = 7
Material = Groundmass
Location = Nevada
Analyst = Dan Miggins
Project = NEVADA | WALKER (13-45)
Mass Discrimination Law = LIN
Irradiation = 14-OSU-01
J = 0.00177164 ± 0.00000244
FCT-NM = 28.020 ± 0.160 Ma

Results	40(r)/39(k) ± 2σ		Age ± 2σ (Ma)		MSWD	39Ar(k) (%,n)	K/Ca ± 2σ
Age Plateau	5.07731	± 0.05348	16.19	± 0.18	1.82	27.31	1.67 ± 0.04
		± 1.05%		± 1.08%	12%	5	
			Full External Error	± 0.44	2.41	2σ Confidence Limit	
			Analytical Error	± 0.17	1.3484	Error Magnification	
Total Fusion Age	4.73444	± 0.02648	15.10	± 0.09		22	1.72 ± 0.01
		± 0.56%		± 0.62%			
			Full External Error	± 0.39			
			Analytical Error	± 0.08			

14D09945.full.xls printed at 6/20/2014 (10:48 AM)
ArArCALC v2.6.2 -- Beta Version

Table 9: LP-9 - Groundmass

OSU Argon Geochronology Lab
CEOAS Oregon State University, Corvallis, USA

Incremental Heating			36Ar(a) [fA]	37Ar(ca) [fA]	38Ar(cl) [fA]	39Ar(k) [fA]	40Ar(r) [fA]	Age ± 2σ (Ma)	40Ar(r) (%)	39Ar(k) (%)	K/Ca ± 2σ
14D09980	1.7 %		0.632313	4.2296	0.0956327	15.5915	23.288	4.81 ± 0.34	11.08	0.36	1.59 ± 0.21
14D09982	1.9 %		0.613662	5.0398	0.1341830	18.8034	30.090	5.15 ± 0.29	14.23	0.43	1.60 ± 0.17
14D09983	2.1 %		0.655948	7.7907	0.2250538	22.9284	42.669	5.99 ± 0.23	18.04	0.53	1.27 ± 0.09
14D09985	2.5 %		0.780971	14.3351	0.2392424	32.0307	81.768	8.21 ± 0.20	26.16	0.74	0.96 ± 0.04
14D09986	2.9 %		0.706751	19.0998	0.1850070	33.7392	107.828	10.27 ± 0.17	34.05	0.78	0.76 ± 0.02
14D09988	3.1 %		0.470153	13.0101	0.1208668	21.0172	74.777	11.43 ± 0.22	34.99	0.48	0.69 ± 0.03
14D09989	3.6 %		0.569628	25.7711	0.1297599	35.7744	143.891	12.92 ± 0.15	46.08	0.82	0.60 ± 0.01
14D09991	4.2 %		0.585434	43.1608	0.2382937	54.7378	245.932	14.42 ± 0.10	58.70	1.26	0.55 ± 0.01
14D09992	4.8 %		0.648936	83.3846	0.2200703	101.1326	486.865	15.45 ± 0.06	71.73	2.32	0.52 ± 0.00
14D09994	5.6 %		0.606875	135.9883	0.2184727	166.3512	827.797	15.97 ± 0.04	82.18	3.82	0.53 ± 0.00
14D09995	6.4 %		0.489173	137.4870	0.2476906	176.3597	876.613	15.95 ± 0.04	85.83	4.05	0.55 ± 0.00
14D09997	7.4 %		0.570862	211.4334	0.1657938	280.9265	1381.591	15.78 ± 0.03	89.10	6.45	0.57 ± 0.00
14D09998	8.4 %		0.611454	257.6873	0.3001369	362.7079	1754.520	15.52 ± 0.03	90.65	8.33	0.61 ± 0.00
14D10000	9.4 %		0.630859	272.1284	0.2470612	406.9151	1937.723	15.28 ± 0.02	91.21	9.35	0.64 ± 0.00
14D10001	10.4 %		0.654373	264.0471	0.3365311	411.6001	1934.670	15.08 ± 0.02	90.90	9.45	0.67 ± 0.00
14D10003	11.4 %		0.705705	239.3404	0.4254879	381.3633	1778.638	14.97 ± 0.03	89.49	8.76	0.69 ± 0.00
14D10004	12.7 %		0.881276	241.6264	0.4583659	380.4997	1762.617	14.87 ± 0.03	87.11	8.74	0.68 ± 0.00
14D10006	14.2 %	⊠	1.168271	241.3904	0.6387126	370.2514	1708.783	14.81 ± 0.03	83.18	8.51	0.66 ± 0.00
14D10007	16.2 %	⊠	1.648894	229.6503	0.8278606	345.1267	1590.219	14.79 ± 0.04	76.53	7.93	0.65 ± 0.00
14D10009	18.2 %	⊠	2.467070	193.6776	1.0366917	295.9641	1361.411	14.76 ± 0.05	65.12	6.80	0.66 ± 0.00
14D10010	21.2 %	⊠	3.286222	179.3547	1.4639684	281.6785	1301.535	14.83 ± 0.07	57.26	6.47	0.68 ± 0.00
14D10012	22.3 %	⊠	2.359012	97.3886	0.9160618	157.7946	733.710	14.92 ± 0.09	51.27	3.62	0.70 ± 0.01
		Σ	21.743840	2917.0214	8.8709449	4353.2939	20186.937				

Information on Analysis
Sample = 9
Material = Groundmass
Location = Nevada
Analyst = Dan Miggins
Project = NEVADA | WALKER (13-45)
Mass Discrimination Law = LIN
Irradiation = 14-OSU-01
J = 0.00178214 ± 0.00000248
FCT-NM = 28.020 ± 0.160 Ma

Results	40(r)/39(k) ± 2σ		Age ± 2σ (Ma)		MSWD	39Ar(k) (%,n)	K/Ca ± 2σ
Age Plateau	4.61285	± 0.01003	14.80	± 0.05	2.68	33.33	0.66 ± 0.02
Error Mean		± 0.22%		± 0.35%	3%	5	
			Full External Error	± 0.38	2.41	2σ Confidence Limit	
			Analytical Error	± 0.03	1.6370	Error Magnification	
Total Fusion Age	4.63716	± 0.00321	14.88	± 0.04		22	0.64 ± 0.00
		± 0.07%		± 0.29%			
			Full External Error	± 0.38			
			Analytical Error	± 0.01			

14D09979.full.xls printed at 6/20/2014 (10:47 AM)
ArArCALC v2.6.2 -- Beta Version

Table 10: LP-4 - Plagioclase

OSU Argon Geochronology Lab
CEOAS Oregon State University, Corvallis, USA

Incremental Heating			36Ar(a) [fA]	37Ar(ca) [fA]	38Ar(cl) [fA]	39Ar(k) [fA]	40Ar(r) [fA]	Age ± 2σ (Ma)	40Ar(r) (%)	39Ar(k) (%)	K/Ca ± 2σ
14D10105	1.7 %	⊠	0.2698446	47.3344	0.7419550	0.607233	3.58974	18.74 ± 6.57	4.31	1.18	0.0055 ± 0.0007
14D10107	1.9 %	⊠	0.0706294	54.2351	0.1752871	0.492125	2.41982	15.60 ± 4.54	10.39	0.95	0.0039 ± 0.0006
14D10108	2.1 %	⊠	0.0353466	50.0328	0.0443483	0.465705	2.77445	18.88 ± 4.54	20.99	0.90	0.0040 ± 0.0006
14D10110	2.5 %	⊠	0.0410662	75.5471	0.0621187	0.600347	3.11371	16.45 ± 3.42	20.42	1.16	0.0034 ± 0.0004
14D10111	2.9 %	⊠	0.0425295	158.4098	0.0524704	1.293711	6.29834	15.45 ± 1.71	33.38	2.50	0.0035 ± 0.0002
14D10113	3.1 %	⊠	0.0351789	228.0557	0.0499346	1.859049	8.74541	14.93 ± 1.18	45.69	3.60	0.0035 ± 0.0001
14D10114	3.6 %	⊠	0.0242946	186.9122	0.0440510	1.476740	7.39635	15.89 ± 1.54	50.74	2.86	0.0034 ± 0.0002
14D10116	4.2 %	⊠	0.0457809	423.5972	0.0704623	3.419376	16.75119	15.54 ± 0.79	55.32	6.62	0.0035 ± 0.0001
14D10117	4.8 %	⊠	0.0217973	297.0395	0.0057291	2.429957	11.50990	15.03 ± 0.97	64.11	4.70	0.0035 ± 0.0001
14D10119	5.6 %	⊠	0.0276882	386.8687	0.0787561	3.393299	15.70887	14.69 ± 0.76	65.74	6.57	0.0038 ± 0.0001
14D10120	6.4 %	⊠	0.0400132	514.9558	0.0246830	4.747040	22.37541	14.96 ± 0.57	65.42	9.19	0.0040 ± 0.0001
14D10122	7.4 %	⊠	0.0341009	400.9983	0.0143889	4.050748	19.03562	14.91 ± 0.63	65.38	7.84	0.0043 ± 0.0001
14D10123	8.4 %	⊠	0.0458977	317.3737	0.0561730	3.749222	17.35430	14.69 ± 0.65	56.12	7.26	0.0051 ± 0.0001
14D10125	9.4 %		0.0839418	257.4730	0.0000000	3.457072	18.03790	16.55 ± 0.78	42.10	6.69	0.0058 ± 0.0001
14D10126	10.4 %		0.1713573	206.2158	0.0417698	3.176840	18.71115	18.67 ± 0.94	26.98	6.15	0.0066 ± 0.0002
14D10128	11.4 %		0.2874641	167.1724	0.0176371	2.913385	20.11509	21.87 ± 1.25	19.15	5.64	0.0075 ± 0.0002
14D10129	12.7 %		0.3814625	152.2969	0.0692688	2.729563	28.36014	32.81 ± 1.59	20.10	5.28	0.0077 ± 0.0002
14D10131	14.2 %		0.4244354	176.5144	0.0468173	2.871636	34.04295	37.39 ± 1.68	21.35	5.56	0.0070 ± 0.0002
14D10132	16.2 %		0.4629201	200.9590	0.0586090	3.030265	39.23228	40.79 ± 1.73	22.29	5.86	0.0065 ± 0.0001
14D10134	18.2 %		0.5136908	141.0710	0.0386637	2.198181	35.07235	50.14 ± 2.57	18.77	4.25	0.0067 ± 0.0002
14D10135	21.2 %		0.6120045	125.1677	0.0902461	1.912396	40.54191	66.32 ± 3.51	18.31	3.70	0.0066 ± 0.0003
14D10137	22.3 %		0.4184772	59.4514	0.0943778	0.793933	28.66464	111.53 ± 10.35	18.82	1.54	0.0057 ± 0.0005
		Σ	4.0899216	4627.6820	1.8777470	51.667822	399.85152				

Information on Analysis
Sample = 4
Material = Plagioclase
Location = Nevada
Analyst = Dan Miggins
Project = NEVADA | WALKER (13-45)
Mass Discrimination Law = LIN
Irradiation = 14-OSU-01
J = 0.00176209 ± 0.00000180
FCT-NM = 28.020 ± 0.160 Ma

Results	40(r)/39(k) ± 2σ		Age ± 2σ (Ma)		MSWD	39Ar(k) (%,n)	K/Ca ± 2σ
Age Plateau	4.73146	± 0.08462 ± 1.79%	15.01	± 0.27 ± 1.79%	0.85 60%	55.32 13	0.0039 ± 0.0003
			Full External Error	± 0.46	1.82	2σ Confidence Limit	
			Analytical Error	± 0.27	1.0000	Error Magnification	
Total Fusion Age	7.73889	± 0.10054 ± 1.30%	24.49	± 0.32 ± 1.31%		22	0.0048 ± 0.0000
			Full External Error	± 0.69			
			Analytical Error	± 0.32			

14D10104.full.xls printed at 6/20/2014 (10:24 AM)
ArArCALC v2.6.2 -- Beta Version

Table 11: LP-7 - Plagioclase

OSU Argon Geochronology Lab
CEOAS Oregon State University, Corvallis, USA

Incremental Heating		36Ar(a) [fA]	37Ar(ca) [fA]	38Ar(cl) [fA]	39Ar(k) [fA]	40Ar(r) [fA]	Age ± 2σ (Ma)	40Ar(r) (%)	39Ar(k) (%)	K/Ca ± 2σ
14D10165	1.7 %	7.2832	4.0390	0.4776157	0.73443	1.710	7.41 ± 57.90	0.08	0.11	0.078 ± 0.013
14D10167	1.9 %	5.6343	3.0157	0.0705617	0.59839	17.721	97.02 ± 64.19	1.08	0.09	0.085 ± 0.018
14D10168	2.1 %	3.2493	1.4098	0.0000000	0.26481	12.328	154.96 ± 120.66	1.30	0.04	0.081 ± 0.038
14D10170	2.5 %	6.0007	4.9966	0.0145539	0.79770	21.243	87.01 ± 49.87	1.21	0.12	0.069 ± 0.010
14D10171	2.9 %	10.1941	11.5201	0.0532794	1.72156	46.730	88.73 ± 34.53	1.58	0.27	0.064 ± 0.004
14D10173	3.1 %	8.8613	9.9088	0.0000000	1.45374	41.129	92.58 ± 36.82	1.60	0.23	0.063 ± 0.005
14D10174	3.6 %	9.3863	12.0023	0.0090656	1.74332	43.958	82.28 ± 31.75	1.61	0.27	0.062 ± 0.004
14D10176	4.2 %	19.4893	44.7961	0.0000000	6.16057	50.311	26.24 ± 16.68	0.88	0.96	0.059 ± 0.001
14D10177	4.8 %	17.1457	35.7172	0.0579316	5.00011	70.439	45.51 ± 18.42	1.41	0.78	0.060 ± 0.001
14D10179	5.6 %	21.8613	61.9159	0.0388016	8.44154	63.288	24.08 ± 13.56	0.99	1.31	0.059 ± 0.001
14D10180	6.4 %	35.4951	131.4138	0.0360183	17.69193	78.264	14.17 ± 10.28	0.75	2.74	0.058 ± 0.001
14D10182	7.4 %	46.3931	164.8008	0.1325250	21.94052	14.834	2.16 ± 10.71	0.11	3.40	0.057 ± 0.000
14D10183	8.4 %	72.4363	225.2111	0.0000000	30.20621	1524.058	168.57 ± 13.44	7.67	4.68	0.058 ± 0.000
14D10185	9.4 %	91.9039	285.6911	0.0000000	38.70635	1770.749	152.16 ± 13.11	6.98	6.00	0.058 ± 0.000
14D10186	10.4 %	98.7430	310.7534	0.0000000	42.85174	1797.339	139.01 ± 12.58	6.56	6.65	0.059 ± 0.000
14D10188	11.4 %	116.7690	372.9356	0.0000000	52.40362	1996.329	125.80 ± 12.05	6.14	8.13	0.060 ± 0.000
14D10189	12.7 %	156.8192	511.5254	0.0000000	74.94027	2532.795	111.16 ± 11.18	5.78	11.62	0.063 ± 0.000
14D10191	14.2 %	132.7079	693.7148	0.0000000	103.46714	1761.713	55.15 ± 6.65	4.70	16.05	0.064 ± 0.000
14D10192	16.2 %	88.8153	639.0796	0.0000000	94.40402	957.189	32.64 ± 4.86	3.79	14.64	0.064 ± 0.000
14D10194	18.2 %	47.0779	436.7604	0.4723994	63.10874	743.324	37.19 ± 3.71	5.07	9.79	0.062 ± 0.000
14D10195	21.2 %	25.3732	387.2512	0.2115440	55.70484	376.162	21.41 ± 2.32	4.78	8.64	0.062 ± 0.000
14D10197	22.3 %	14.3201	161.3483	0.0911153	22.40214	179.348	25.36 ± 3.33	4.07	3.47	0.060 ± 0.000
	Σ	1035.9593	4509.8070	1.6654115	644.74369	11499.873				

Information on Analysis
Sample = 7
Material = Plagioclase
Location = Nevada
Analyst = Dan Miggins
Project = NEVADA | WALKER (13-45)
Mass Discrimination Law = LIN
Irradiation = 14-OSU-01
J = 0.00176404 ± 0.00000243
FCT-NM = 28.020 ± 0.160 Ma

Results	40(r)/39(k) ± 2σ	Age ± 2σ (Ma)	MSWD	39Ar(k) (%,n)	K/Ca ± 2σ
Age Plateau Cannot Calculate					
Total Fusion Age	17.83635 ± 0.75821 ± 4.25%	57.81 ± 2.50 ± 4.33% Full External Error ± 2.91 Analytical Error ± 2.50		22	0.061 ± 0.000

14D10164.full.xls printed at 6/20/2014 (10:49 AM)
ArArCALC v2.6.2 -- Beta Version

Table 12: LP-12 - Plagioclase

OSU Argon Geochronology Lab
CEOAS Oregon State University, Corvallis, USA

Incremental Heating			36Ar(a) [fA]	37Ar(ca) [fA]	38Ar(cl) [fA]	39Ar(k) [fA]	40Ar(r) [fA]	Age ± 2σ (Ma)	40Ar(r) (%)	39Ar(k) (%)	K/Ca ± 2σ
14D10199	1.7 %		12.780177	46.8600	0.1630243	5.54415	2.8579	1.67 ± 12.03	0.08	0.71	0.051 ± 0.001
14D10201	1.9 %		0.743806	5.4304	0.0078089	0.99588	2.9251	9.46 ± 6.14	1.31	0.13	0.079 ± 0.009
14D10202	2.1 %		0.556575	5.8439	0.0347639	0.99537	2.0549	6.65 ± 5.32	1.23	0.13	0.073 ± 0.008
14D10204	2.5 %		1.605605	12.8215	0.0999335	1.99511	8.0064	12.91 ± 5.18	1.66	0.26	0.067 ± 0.003
14D10205	2.9 %		0.936502	26.6088	0.0489075	4.04337	14.0814	11.21 ± 1.67	4.84	0.52	0.065 ± 0.002
14D10207	3.1 %		0.341202	21.3111	0.0283229	3.35054	14.4131	13.84 ± 1.35	12.51	0.43	0.068 ± 0.002
14D10208	3.6 %		0.373336	22.0712	0.0047872	3.41596	13.7047	12.91 ± 1.30	11.05	0.44	0.067 ± 0.002
14D10210	4.2 %	⊠	0.350471	36.5719	0.0253847	5.64120	25.1430	14.33 ± 0.82	19.53	0.73	0.066 ± 0.001
14D10211	4.8 %	⊠	0.326666	61.3592	0.0744285	9.55495	42.7113	14.37 ± 0.49	30.67	1.23	0.067 ± 0.001
14D10213	5.6 %	⊠	0.166826	92.7212	0.0576898	14.85364	65.5104	14.18 ± 0.26	57.05	1.92	0.069 ± 0.001
14D10214	6.4 %	⊠	0.071300	179.7306	0.0676668	28.95586	128.6824	14.29 ± 0.13	85.91	3.73	0.069 ± 0.001
14D10216	7.4 %	⊠	0.040900	239.6679	0.0193382	38.21691	170.9560	14.39 ± 0.10	93.38	4.93	0.069 ± 0.000
14D10217	8.4 %	⊠	0.032422	365.6760	0.1015060	57.61862	257.4618	14.37 ± 0.07	96.39	7.43	0.068 ± 0.000
14D10219	9.4 %	⊠	0.036388	436.9609	0.0947770	68.42911	306.4592	14.40 ± 0.06	96.59	8.82	0.067 ± 0.000
14D10220	10.4 %	⊠	0.024928	471.4645	0.1035265	74.34397	332.0744	14.36 ± 0.05	97.81	9.59	0.068 ± 0.000
14D10222	11.4 %	⊠	0.018035	504.1631	0.0846023	79.35638	355.3488	14.40 ± 0.05	98.50	10.23	0.068 ± 0.000
14D10223	12.7 %	⊠	0.014383	549.3045	0.0804691	87.04347	390.1473	14.41 ± 0.05	98.90	11.22	0.068 ± 0.000
14D10225	14.2 %	⊠	0.024646	551.6532	0.1765322	88.40753	396.6668	14.43 ± 0.05	98.18	11.40	0.069 ± 0.000
14D10226	16.2 %	⊠	0.038468	502.3027	0.1544219	79.50574	357.3716	14.45 ± 0.05	96.90	10.25	0.068 ± 0.000
14D10228	18.2 %	⊠	0.029546	356.0057	0.0858350	55.41642	248.8263	14.44 ± 0.07	96.59	7.15	0.067 ± 0.000
14D10229	21.2 %	⊠	0.010309	280.9668	0.0540118	44.25264	199.0094	14.46 ± 0.08	98.47	5.71	0.068 ± 0.000
14D10231	22.3 %	⊠	0.008180	152.6084	0.0491463	23.53167	105.4988	14.42 ± 0.14	97.74	3.03	0.066 ± 0.001
		Σ	18.530671	4922.1034	1.6168841	775.46850	3434.1951				

Information on Analysis
Sample = 12
Material = Plagioclase
Location = Nevada
Analyst = Dan Miggins
Project = NEVADA | WALKER (13-45)
Mass Discrimination Law = LIN
Irradiation = 14-OSU-01
J = 0.00178543 ± 0.00000248
FCT-NM = 28.020 ± 0.160 Ma

Results	40(r)/39(k) ± 2σ		Age ± 2σ (Ma)		MSWD	39Ar(k) (%,n)	K/Ca ± 2σ
Age Plateau	4.48043	± 0.00627	14.41	± 0.04	1.22	97.38	0.068 ± 0.000
		± 0.14%		± 0.31%	25%	15	
			Full External Error	± 0.37	1.76	2σ Confidence Limit	
			Analytical Error	± 0.02	1.1028	Error Magnification	
Total Fusion Age	4.42854	± 0.02810	14.24	± 0.10		22	0.068 ± 0.000
		± 0.63%		± 0.69%			
			Full External Error	± 0.37			
			Analytical Error	± 0.09			

14D10198.full.xls printed at 6/20/2014 (10:27 AM)
ArArCALC v2.6.2 -- Beta Version

Table 13: LP-9 - Plagioclase

OSU Argon Geochronology Lab
CEOAS Oregon State University, Corvallis, USA

Incremental Heating			36Ar(a) [fA]	37Ar(ca) [fA]	38Ar(cl) [fA]	39Ar(k) [fA]	40Ar(r) [fA]	Age ± 2σ (Ma)	40Ar(r) (%)	39Ar(k) (%)	K/Ca ± 2σ
14D10258	1.7 %		1.6532100	27.6737	0.1038364	0.41509	16.2380	121.49 ± 32.44	3.22	0.29	0.0064 ± 0.0012
14D10260	1.9 %		0.4541460	34.0700	0.0422252	0.45373	4.1741	29.31 ± 10.36	3.02	0.32	0.0057 ± 0.0009
14D10261	2.1 %		0.1013803	17.2074	0.0000000	0.24428	1.7244	22.53 ± 12.38	5.44	0.17	0.0061 ± 0.0018
14D10263	2.5 %		0.2219281	52.0382	0.0000000	0.69449	8.1990	37.53 ± 5.97	11.11	0.49	0.0057 ± 0.0006
14D10264	2.9 %		0.2287440	161.4609	0.0000000	1.91718	15.8591	26.38 ± 1.97	19.00	1.36	0.0051 ± 0.0002
14D10266	3.1 %		0.0709451	107.1002	0.0000000	1.19463	8.0745	21.58 ± 2.38	27.80	0.85	0.0048 ± 0.0003
14D10267	3.6 %	⊠	0.1540868	275.1994	0.0010597	3.05068	20.3979	21.35 ± 1.11	30.94	2.17	0.0048 ± 0.0001
14D10269	4.2 %	⊠	0.0799452	279.1036	0.0000000	3.00757	20.6779	21.95 ± 1.05	46.67	2.14	0.0046 ± 0.0001
14D10270	4.8 %	⊠	0.0685231	579.4684	0.0281557	6.21204	37.5560	19.32 ± 0.54	64.96	4.41	0.0046 ± 0.0001
14D10272	5.6 %	⊠	0.0662222	791.6446	0.0235031	8.80011	56.5698	20.53 ± 0.44	74.29	6.25	0.0048 ± 0.0000
14D10273	6.4 %	⊠	0.0407615	821.0393	0.0000000	9.43509	54.9929	18.63 ± 0.40	82.02	6.70	0.0049 ± 0.0000
14D10275	7.4 %	⊠	0.0441256	926.1643	0.0658928	11.01444	66.4241	19.27 ± 0.36	83.58	7.83	0.0051 ± 0.0000
14D10276	8.4 %	⊠	0.0395291	974.1533	0.0530316	12.46061	79.6838	20.43 ± 0.31	87.20	8.86	0.0055 ± 0.0000
14D10278	9.4 %		0.0314835	872.5451	0.0000000	12.30977	95.5528	24.76 ± 0.32	91.12	8.75	0.0061 ± 0.0001
14D10279	10.4 %		0.0325599	713.9503	0.0000000	10.65485	104.7981	31.32 ± 0.37	91.58	7.57	0.0064 ± 0.0001
14D10281	11.4 %		0.0392999	520.7672	0.0200676	8.16599	122.1232	47.41 ± 0.54	91.31	5.80	0.0067 ± 0.0001
14D10282	12.7 %		0.0516785	421.3265	0.0506789	7.39844	252.0951	106.27 ± 1.05	94.29	5.26	0.0076 ± 0.0001
14D10284	14.2 %		0.0732735	377.5175	0.0789036	8.96949	294.6920	102.57 ± 0.85	93.15	6.37	0.0102 ± 0.0001
14D10285	16.2 %		0.0992525	357.9460	0.1150170	7.28139	99.5455	43.39 ± 0.60	77.24	5.17	0.0087 ± 0.0001
14D10287	18.2 %		0.1551750	725.4029	0.1834525	14.46373	147.9288	32.56 ± 0.29	76.33	10.28	0.0086 ± 0.0001
14D10288	21.2 %		0.0795551	553.4333	0.0451409	8.94584	79.4426	28.30 ± 0.43	77.16	6.36	0.0070 ± 0.0001
14D10290	22.3 %		0.0662294	248.0813	0.0000000	3.62830	27.9554	24.58 ± 0.88	58.82	2.58	0.0063 ± 0.0001
		Σ	3.8520543	9837.2934	0.8109650	140.71774	1614.7051				

Information on Analysis
Sample = 9
Material = Plagioclase
Location = Nevada
Analyst = Dan Miggins
Project = NEVADA | WALKER (13-45)
Mass Discrimination Law = LIN
Irradiation = 14-OSU-01
J = 0.00177639 ± 0.00000247
FCT-NM = 28.020 ± 0.160 Ma

Results	40(r)/39(k) ± 2σ	Age ± 2σ (Ma)	MSWD	39Ar(k) (%,n)	K/Ca ± 2σ
Age Plateau	6.20269 ± 0.21611	19.82 ± 0.69	16.48	38.36	0.0050 ± 0.0002
Error Mean	± 3.48%	± 3.48%	0%	7	
		Full External Error ± 0.85	2.15	2σ Confidence Limit	
		Analytical Error ± 0.69	4.0599	Error Magnification	
Total Fusion Age	11.47478 ± 0.04914	36.49 ± 0.18		22	0.0062 ± 0.0000
	± 0.43%	± 0.51%			
		Full External Error ± 0.94			
		Analytical Error ± 0.15			

14D10257.full.xls printed at 6/20/2014 (10:28 AM)
ArArCALC v2.6.2 -- Beta Version

Table 14: LP-10 - Groundmass

OSU Argon Geochronology Lab
CEOAS Oregon State University, Corvallis, USA

Incremental Heating			36Ar(a) [fA]	37Ar(ca) [fA]	38Ar(cl) [fA]	39Ar(k) [fA]	40Ar(r) [fA]	Age ± 2σ (Ma)	40Ar(r) (%)	39Ar(k) (%)	K/Ca ± 2σ
14D11625	1.7 %		0.981289	11.1541	3.352578	36.7212	144.601	12.27 ± 0.18	33.27	1.67	1.416 ± 0.084
14D11627	1.9 %		0.960697	13.8269	3.645770	40.7258	166.931	12.77 ± 0.17	37.03	1.85	1.267 ± 0.060
14D11628	2.1 %		0.598043	8.3027	2.277710	25.6134	104.650	12.73 ± 0.20	37.19	1.17	1.327 ± 0.101
14D11630	2.5 %		1.146970	28.4760	5.039211	61.7958	263.787	13.30 ± 0.13	43.76	2.81	0.933 ± 0.021
14D11631	2.9 %		1.088882	38.5237	5.299837	68.9131	302.184	13.66 ± 0.11	48.43	3.13	0.769 ± 0.014
14D11633	3.1 %		0.983093	48.9544	5.305585	73.2936	332.991	14.15 ± 0.10	53.40	3.33	0.644 ± 0.010
14D11634	3.6 %		0.709021	41.9225	3.834884	57.4602	264.447	14.34 ± 0.10	55.79	2.61	0.589 ± 0.010
14D11636	4.2 %		0.861254	86.1134	4.993288	87.7706	412.441	14.64 ± 0.08	61.83	3.99	0.438 ± 0.004
14D11637	4.8 %		0.906283	153.8380	5.465589	122.1008	583.585	14.89 ± 0.06	68.53	5.55	0.341 ± 0.003
14D11639	5.6 %	⊠	0.931710	266.7639	5.574165	174.0824	839.816	15.03 ± 0.05	75.30	7.92	0.281 ± 0.002
14D11640	6.4 %	⊠	0.648796	244.4230	3.587822	147.4384	712.915	15.06 ± 0.05	78.79	6.71	0.259 ± 0.002
14D11642	7.4 %	⊠	0.636429	353.4861	3.345510	197.2961	950.303	15.00 ± 0.04	83.46	8.97	0.240 ± 0.002
14D11643	8.4 %		0.514726	366.7171	2.338556	201.0777	963.318	14.92 ± 0.03	86.35	9.15	0.236 ± 0.002
14D11645	9.4 %		0.414928	347.0599	1.667692	191.4763	913.963	14.87 ± 0.03	88.16	8.71	0.237 ± 0.002
14D11646	10.4 %		0.313712	274.1953	1.136688	153.0811	726.740	14.79 ± 0.03	88.67	6.96	0.240 ± 0.002
14D11648	11.4 %		0.256542	228.6805	0.820041	125.8138	595.163	14.73 ± 0.04	88.68	5.72	0.237 ± 0.002
14D11649	12.7 %		0.240316	198.0191	0.716081	105.9064	498.594	14.66 ± 0.04	87.52	4.82	0.230 ± 0.002
14D11651	14.2 %		0.214860	178.7862	0.543976	88.6810	415.081	14.58 ± 0.04	86.72	4.03	0.213 ± 0.002
14D11652	16.2 %		0.245404	196.0970	0.521433	82.1463	380.452	14.43 ± 0.05	83.98	3.74	0.180 ± 0.001
14D11654	18.2 %		0.237903	196.3346	0.424383	68.1530	312.389	14.28 ± 0.06	81.62	3.10	0.149 ± 0.001
14D11655	21.2 %		0.232512	208.0092	0.392568	58.1626	265.490	14.22 ± 0.07	79.43	2.65	0.120 ± 0.001
14D11657	22.3 %		0.150544	124.0639	0.133317	30.8271	142.741	14.42 ± 0.11	76.23	1.40	0.107 ± 0.001
		Σ	13.273914	3613.7473	60.416683	2198.5368	10292.581				

Information on Analysis
Sample = 10
Material = Groundmass
Location = Nevada
Analyst = Dan Miggins
Project = NEVADA | WALKER (13-45)
Mass Discrimination Law = LIN
Irradiation = 14-OSU-01
J = 0.00172952 ± 0.00000175
FCT-NM = 28.020 ± 0.160 Ma

Results	40(r)/39(k) ± 2σ		Age ± 2σ (Ma)		MSWD	39Ar(k) (%,n)	K/Ca ± 2σ
Age Plateau	4.82387	± 0.01106	15.02	± 0.05	2.06	23.60	0.258 ± 0.023
		± 0.23%		± 0.30%	13%	3	
			Full External Error	± 0.38	3.00	2σ Confidence Limit	
			Analytical Error	± 0.03	1.4353	Error Magnification	
Total Fusion Age	4.68156	± 0.00416	14.58	± 0.03		22	0.262 ± 0.001
		± 0.09%		± 0.22%			
			Full External Error	± 0.37			
			Analytical Error	± 0.01			

14D11624.full.xls printed at 6/20/2014 (10:29 AM)
ArArCALC v2.6.2 -- Beta Version

Table 15: LP-13 - Groundmass

OSU Argon Geochronology Lab
CEOAS Oregon State University, Corvallis, USA

Incremental Heating			36Ar(a) [fA]	37Ar(ca) [fA]	38Ar(cl) [fA]	39Ar(k) [fA]	40Ar(r) [fA]	Age ± 2σ (Ma)	40Ar(r) (%)	39Ar(k) (%)	K/Ca ± 2σ
14D11691	1.7 %		1.541095	28.8150	3.238813	93.3516	391.6346	13.01 ± 0.10	46.23	4.64	1.393 ± 0.039
14D11693	1.9 %		1.496530	36.7225	3.722106	112.0200	496.7154	13.75 ± 0.09	52.90	5.57	1.312 ± 0.028
14D11694	2.1 %		0.937122	28.5522	2.667944	81.2690	374.6027	14.29 ± 0.08	57.49	4.04	1.224 ± 0.033
14D11696	2.5 %		1.269273	53.1006	4.134483	130.9555	622.0295	14.72 ± 0.06	62.38	6.51	1.060 ± 0.017
14D11697	2.9 %	⊠	0.949862	51.0935	3.499560	115.1247	564.3667	15.19 ± 0.06	66.78	5.72	0.969 ± 0.016
14D11699	3.1 %	⊠	0.950221	68.3675	3.803750	127.0792	625.8668	15.26 ± 0.06	69.02	6.31	0.799 ± 0.010
14D11700	3.6 %	⊠	1.058954	109.3324	4.547384	160.0746	790.3949	15.30 ± 0.05	71.63	7.95	0.630 ± 0.006
14D11702	4.2 %	⊠	1.016933	153.6009	4.665781	174.0581	856.1710	15.24 ± 0.05	74.01	8.65	0.487 ± 0.004
14D11703	4.8 %		0.824115	159.6241	3.693954	146.0586	712.6485	15.12 ± 0.05	74.52	7.26	0.393 ± 0.003
14D11705	5.6 %		0.765614	194.5266	3.249572	141.2425	683.4513	15.00 ± 0.05	75.12	7.02	0.312 ± 0.003
14D11706	6.4 %		0.860042	314.0236	3.677885	174.6411	818.9064	14.53 ± 0.04	76.30	8.68	0.239 ± 0.002
14D11708	7.4 %		0.681970	311.9947	2.794095	140.1136	648.1700	14.34 ± 0.05	76.27	6.96	0.193 ± 0.001
14D11709	8.4 %		0.613511	293.0495	2.264629	115.9111	522.1458	13.96 ± 0.05	74.22	5.76	0.170 ± 0.001
14D11711	9.4 %		0.484621	238.5334	1.810363	84.3487	370.0493	13.60 ± 0.06	72.09	4.19	0.152 ± 0.001
14D11712	10.4 %		0.395585	179.9143	1.397384	59.2403	256.3272	13.41 ± 0.07	68.67	2.94	0.142 ± 0.001
14D11714	11.4 %		0.328957	139.9816	1.122675	44.0395	186.2267	13.11 ± 0.09	65.69	2.19	0.135 ± 0.001
14D11715	12.7 %		0.254804	105.9736	0.729553	30.6909	125.9469	12.73 ± 0.11	62.58	1.53	0.125 ± 0.001
14D11717	14.2 %		0.284447	106.2789	0.655498	26.8584	108.3939	12.52 ± 0.13	56.32	1.33	0.109 ± 0.001
14D11718	16.2 %		0.198152	97.5474	0.501271	21.0476	84.7569	12.49 ± 0.15	59.13	1.05	0.093 ± 0.001
14D11720	18.2 %		0.145003	85.2493	0.311079	14.6088	60.0757	12.75 ± 0.20	58.36	0.73	0.074 ± 0.001
14D11721	21.2 %		0.131894	94.7344	0.388990	13.0936	54.2811	12.85 ± 0.21	58.20	0.65	0.059 ± 0.001
14D11723	22.3 %		0.069605	36.6757	0.113198	6.5211	28.3470	13.48 ± 0.39	57.94	0.32	0.076 ± 0.002
	Σ		15.258308	2887.6916	52.989967	2012.3487	9381.5083				

Information on Analysis
Sample = 13
Material = Groundmass
Location = Nevada
Analyst = Dan Miggins
Project = NEVADA | WALKER (13-45)
Mass Discrimination Law = LIN
Irradiation = 14-OSU-01
J = 0.00172082 ± 0.00000172
FCT-NM = 28.020 ± 0.160 Ma

Results	40(r)/39(k) ± 2σ		Age ± 2σ (Ma)		MSWD	39Ar(k) (%,n)	K/Ca ± 2σ
Age Plateau	4.92252	± 0.01366	15.25	± 0.05	2.57	28.64	0.577 ± 0.150
		± 0.28%		± 0.34%	5%	4	
			Full External Error	± 0.39	2.63	2σ Confidence Limit	
			Analytical Error	± 0.04	1.6023	Error Magnification	
Total Fusion Age	4.66197	± 0.00477	14.45	± 0.03		22	0.300 ± 0.001
		± 0.10%		± 0.22%			
			Full External Error	± 0.37			
			Analytical Error	± 0.01			

14D11689.full.xls printed at 6/20/2014 (10:30 AM)
ArArCALC v2.6.2 -- Beta Version

Table 16: LP-10 – Plagioclase

OSU Argon Geochronology Lab
CEOAS Oregon State University, Corvallis, USA

Incremental Heating			36Ar(a) [fA]	37Ar(ca) [fA]	38Ar(cl) [fA]	39Ar(k) [fA]	40Ar(r) [fA]	Age ± 2σ (Ma)	40Ar(r) (%)	39Ar(k) (%)	K/Ca ± 2σ
14D11725	1.7 %		6.376425	53.0156	0.0628460	0.66695	34.51121	155.81 ± 50.09	1.80	0.48	0.0054 ± 0.0006
14D11727	1.9 %		1.812290	49.7274	0.0000000	0.61280	5.66290	28.83 ± 17.96	1.05	0.45	0.0053 ± 0.0007
14D11728	2.1 %		1.055165	49.0992	0.0167706	0.58404	9.06545	48.16 ± 13.71	2.83	0.42	0.0051 ± 0.0007
14D11729	2.5 %		2.253797	116.0891	0.0000000	1.34013	16.46031	38.22 ± 9.77	2.41	0.97	0.0050 ± 0.0003
14D11730	2.9 %		2.231046	186.5302	0.0105549	2.14019	17.75393	25.90 ± 6.30	2.62	1.56	0.0049 ± 0.0002
14D11732	3.1 %	⊠	1.075463	167.7416	0.0000000	1.90047	9.99509	16.46 ± 4.12	3.05	1.38	0.0049 ± 0.0002
14D11733	3.6 %	⊠	1.004834	205.6068	0.0148179	2.32257	12.85519	17.32 ± 3.31	4.15	1.69	0.0049 ± 0.0002
14D11735	4.2 %	⊠	2.092859	314.9905	0.0000000	3.49215	21.85037	19.57 ± 3.62	3.41	2.54	0.0048 ± 0.0001
14D11736	4.8 %	⊠	2.037441	439.4961	0.0565079	4.97623	29.25708	18.39 ± 2.61	4.63	3.62	0.0049 ± 0.0001
14D11738	5.6 %	⊠	2.224865	674.6315	0.0205063	7.74079	43.05807	17.41 ± 1.81	6.15	5.63	0.0049 ± 0.0001
14D11739	6.4 %	⊠	1.530824	784.2781	0.0470597	9.36419	48.15798	16.10 ± 1.17	9.62	6.81	0.0051 ± 0.0001
14D11741	7.4 %	⊠	1.317170	881.9001	0.0387540	10.86011	57.38418	16.54 ± 0.91	12.85	7.90	0.0053 ± 0.0001
14D11742	8.4 %	⊠	0.931762	935.9537	0.0220043	12.04753	58.04442	15.09 ± 0.66	17.41	8.76	0.0055 ± 0.0001
14D11744	9.4 %	⊠	0.450978	823.2513	0.0329208	10.87259	53.58603	15.43 ± 0.52	28.68	7.90	0.0057 ± 0.0001
14D11745	10.4 %	⊠	0.367230	696.0455	0.0140553	9.89681	49.69640	15.72 ± 0.52	31.41	7.19	0.0061 ± 0.0001
14D11747	11.4 %	⊠	0.226814	620.4017	0.0282022	9.32214	45.39783	15.25 ± 0.47	40.38	6.78	0.0065 ± 0.0001
14D11748	12.7 %		0.144327	543.7746	0.0842973	8.91214	47.36864	16.64 ± 0.45	52.62	6.48	0.0070 ± 0.0001
14D11750	14.2 %		0.202812	521.9393	0.0525784	9.28001	48.20045	16.26 ± 0.43	44.57	6.75	0.0076 ± 0.0001
14D11751	16.2 %		0.213309	491.2563	0.0499436	9.19454	49.67379	16.91 ± 0.46	44.07	6.68	0.0080 ± 0.0001
14D11753	18.2 %		0.199786	412.0605	0.0581013	8.33270	49.71341	18.66 ± 0.50	45.71	6.06	0.0087 ± 0.0001
14D11754	21.2 %		0.203906	467.9301	0.0351691	8.69968	54.88647	19.73 ± 0.48	47.67	6.32	0.0080 ± 0.0001
14D11756	22.3 %		0.140246	246.3417	0.0644044	4.99473	29.11832	18.24 ± 0.70	41.26	3.63	0.0087 ± 0.0002
		Σ	28.093349	9682.0609	0.7094937	137.55346	791.69752				

Information on Analysis
Sample = 10
Material = Plagioclase
Location = Nevada
Analyst = Dan Miggins
Project = NEVADA | WALKER (13-45)
Mass Discrimination Law = LIN
Irradiation = 14-OSU-01
J = 0.00173902 ± 0.00000176
FCT-NM = 28.020 ± 0.160 Ma

Results	40(r)/39(k) ± 2σ		Age ± 2σ (Ma)		MSWD	39Ar(k) (%,n)	K/Ca ± 2σ
Age Plateau	4.98197	± 0.12301	15.60	± 0.38	2.49	60.19	0.0055 ± 0.0003
Error Mean		± 2.47%		± 2.47%	1%	11	
			Full External Error	± 0.55	1.89	2σ Confidence Limit	
			Analytical Error	± 0.38	1.5780	Error Magnification	
Total Fusion Age	5.75556	± 0.12293	18.01	± 0.38		22	0.0061 ± 0.0000
		± 2.14%		± 2.13%			
			Full External Error	± 0.59			
			Analytical Error	± 0.38			

14D11724.full.xls printed at 6/20/2014 (10:31 AM)
ArArCALC v2.6.2 -- Beta Version

9. APPENDIX B: 2D-SEICMIC IMAGES

Plate 1: Seismic Line 1

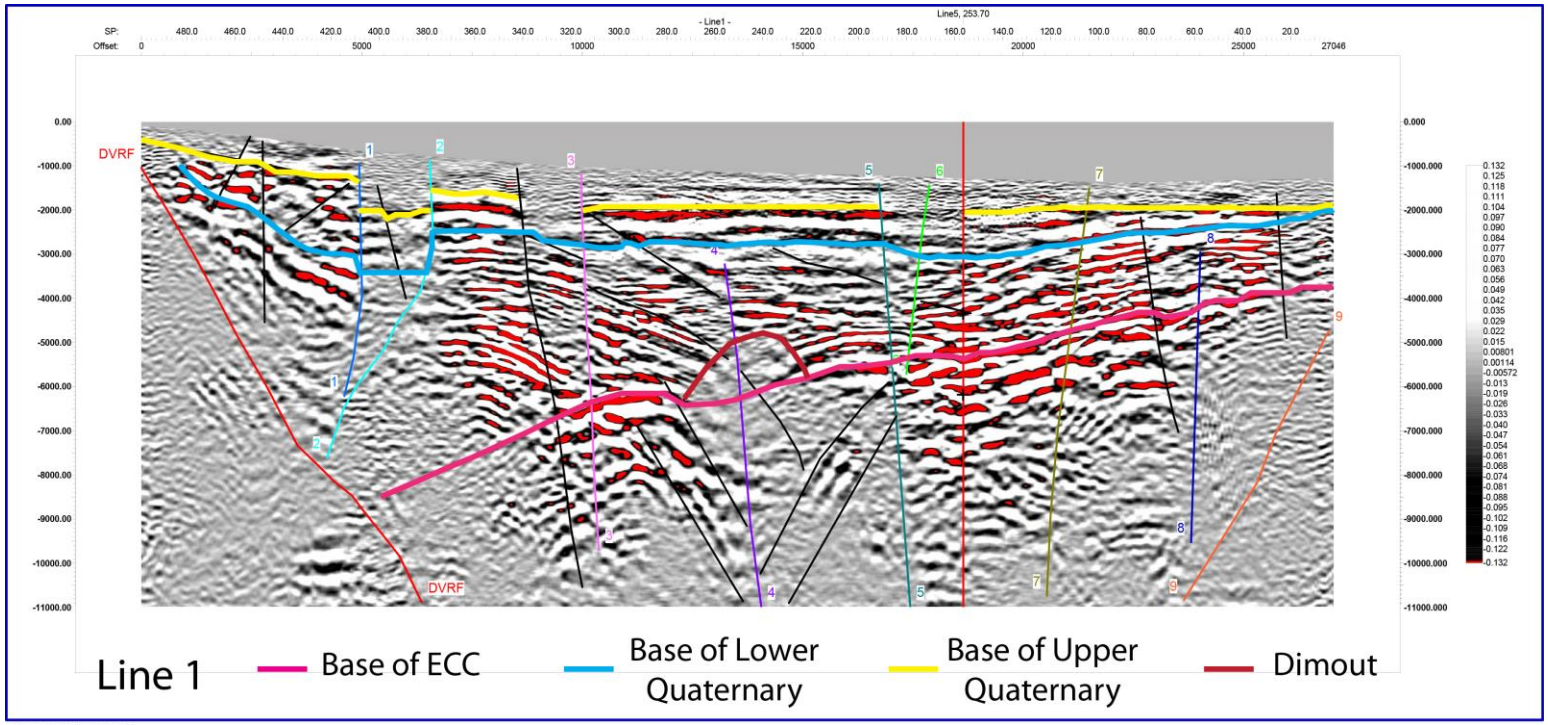

s482a651@LIN-GEO-03214
05/14/15 09:21:13

Plate 2: Seismic Line 1 With Velocity

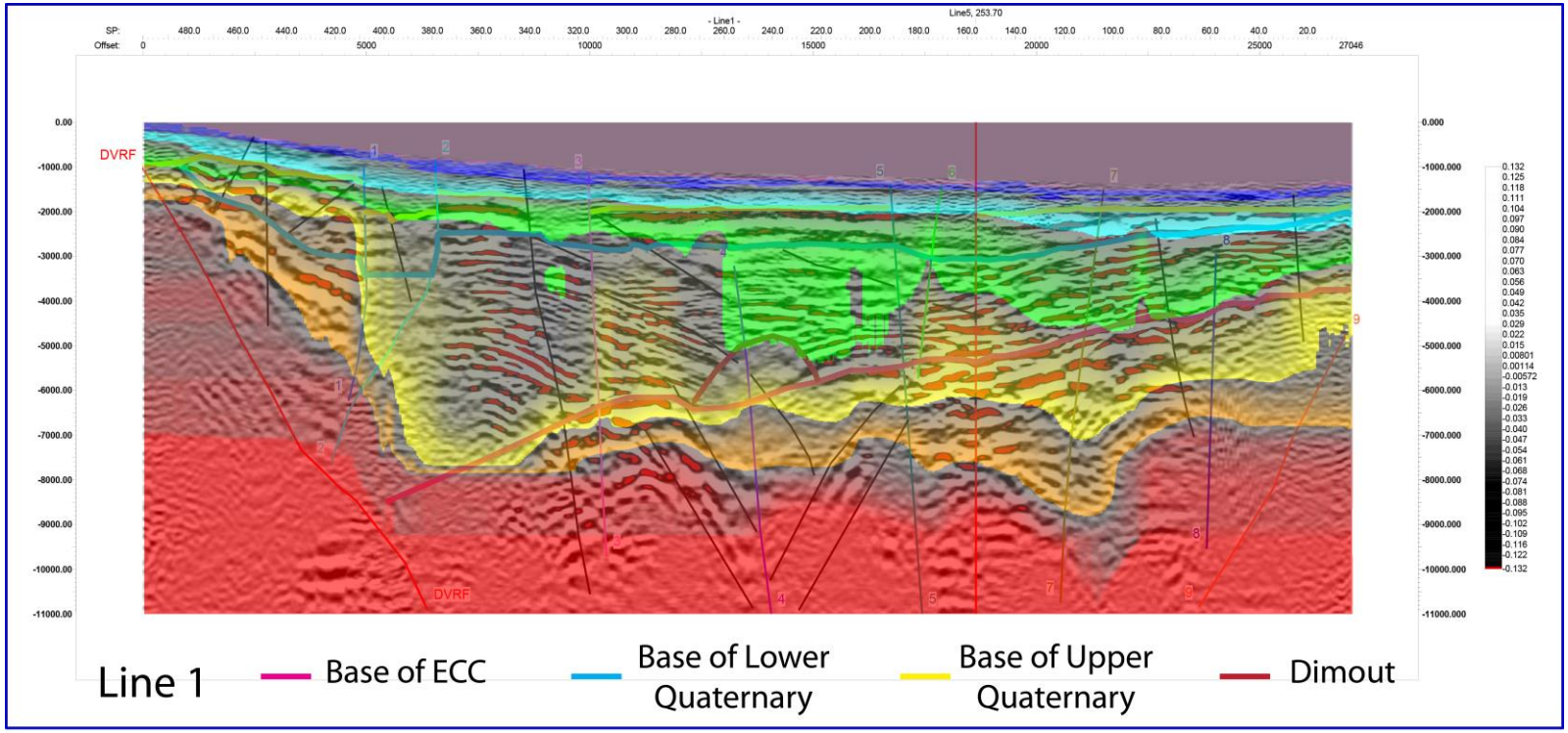

Plate 3: Seismic Line 2

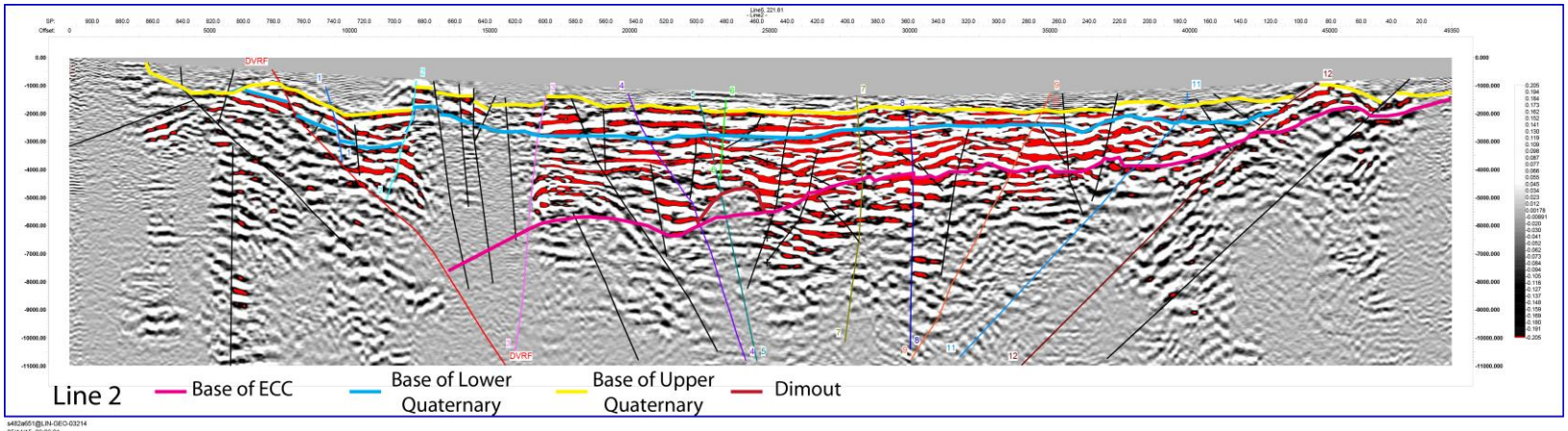

Plate 4: Seismic Line 2 With Velocity

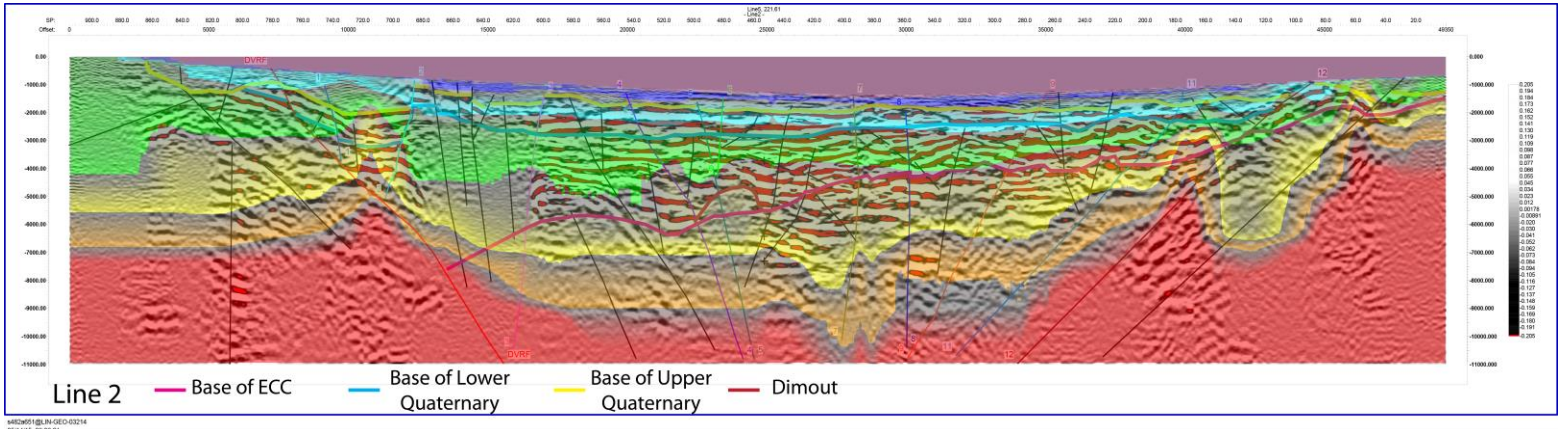

Plate 5: Seismic Line 3

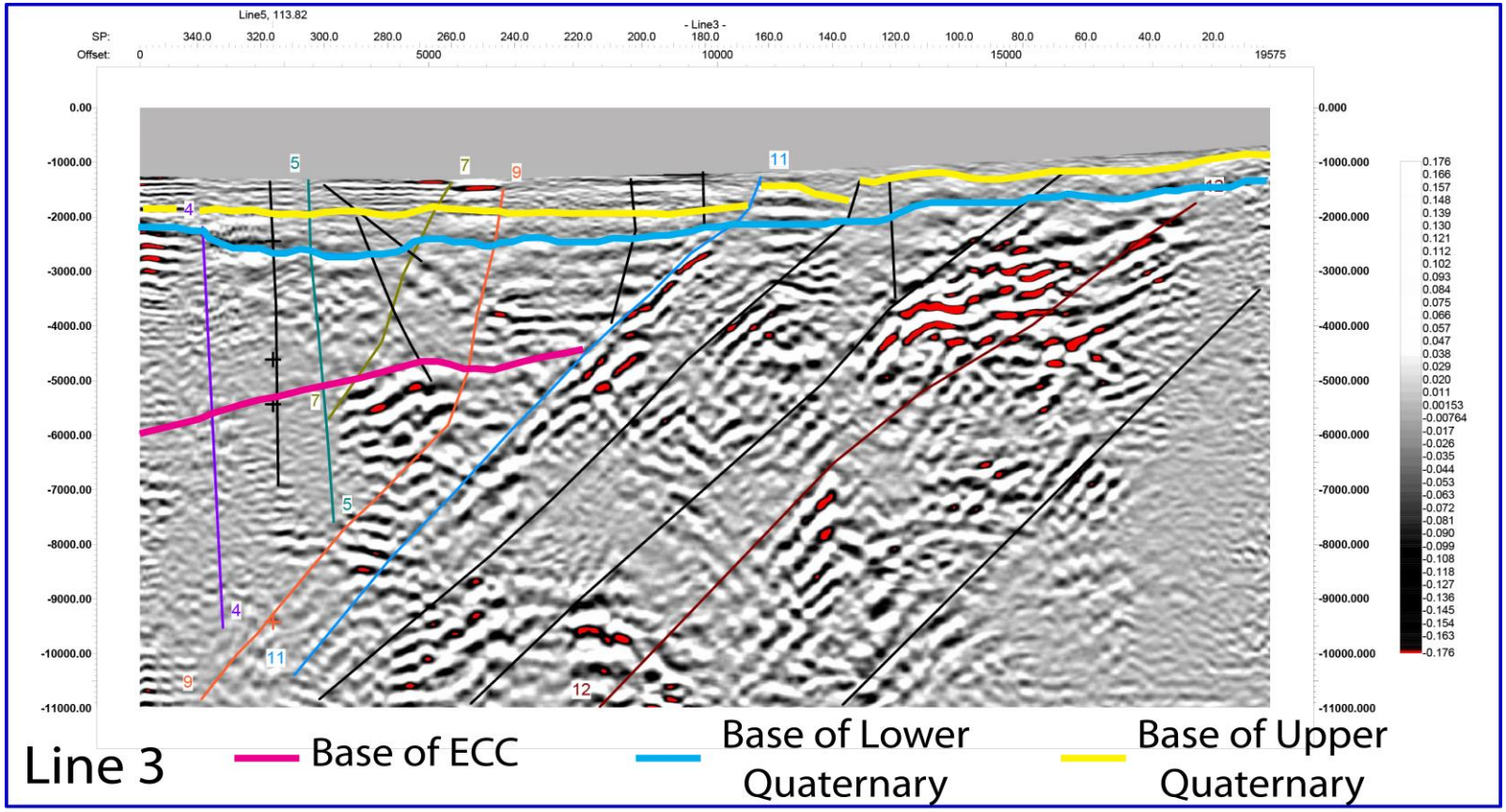

Plate 6: Seismic Line 3 With Velocity

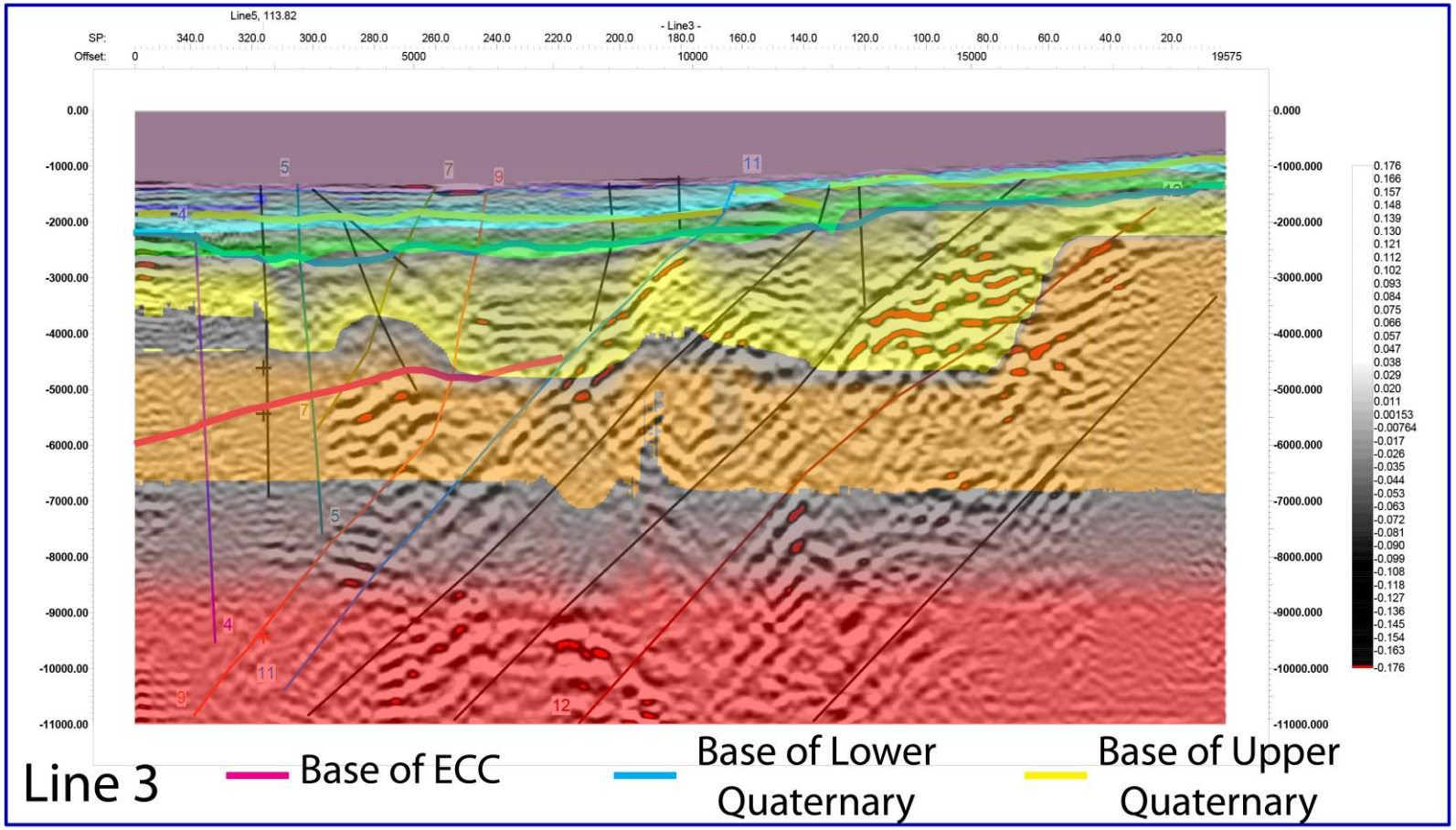

Plate 7: Seismic Line 4

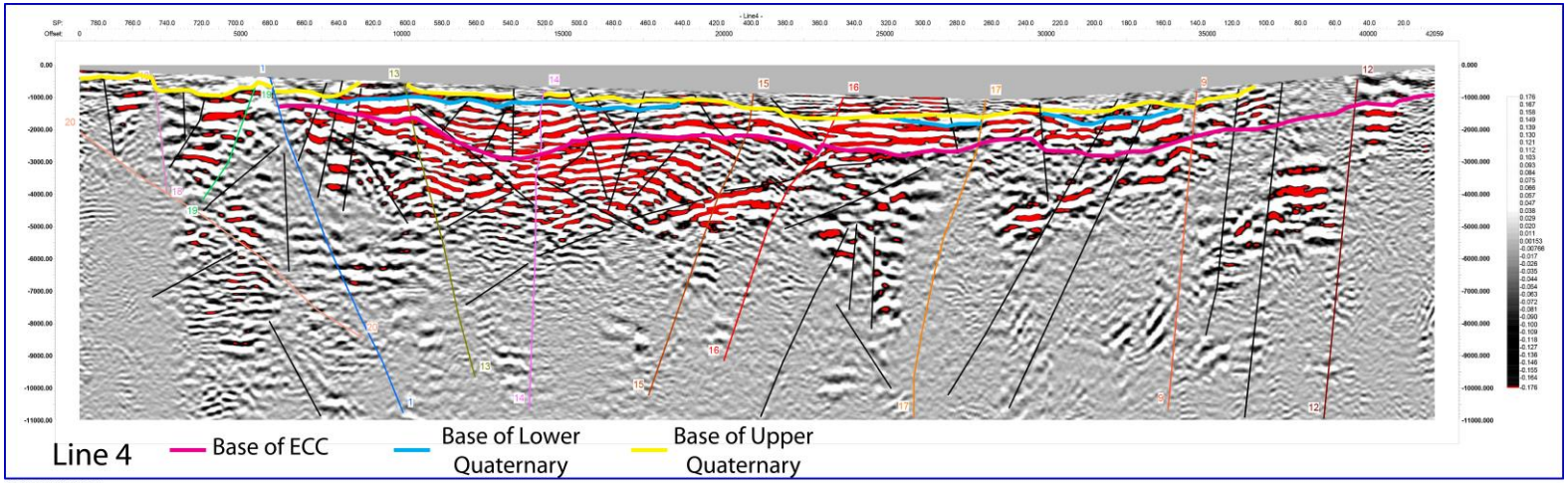

Plate 8: Seismic Line 4 with Velocity

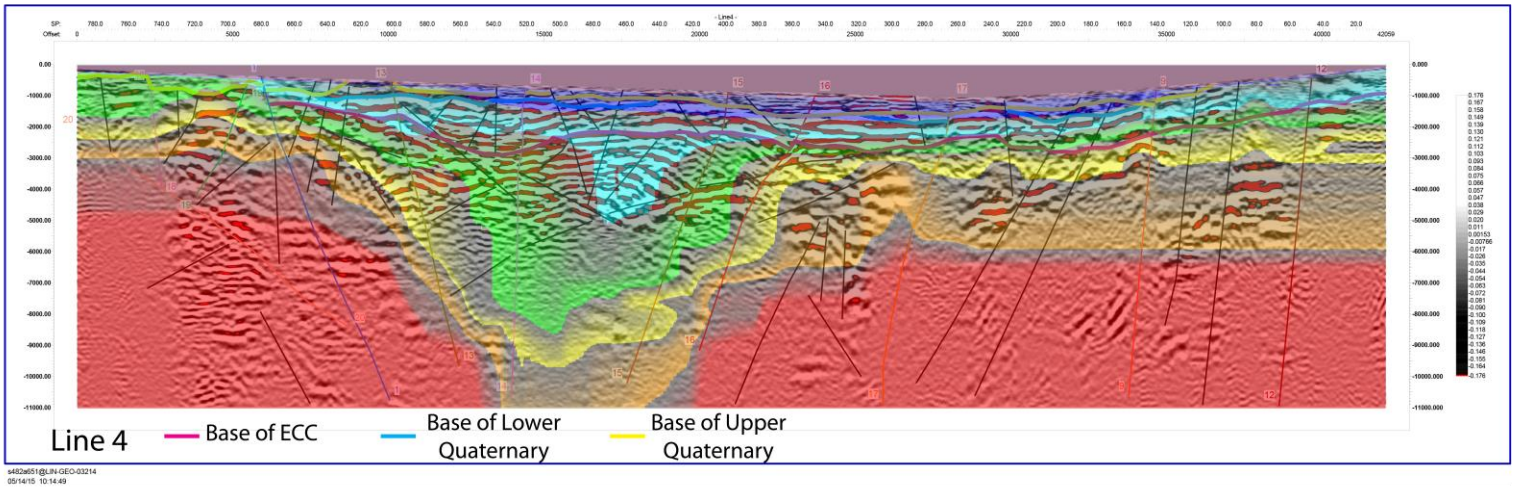

Plate 9: Seismic Line 5

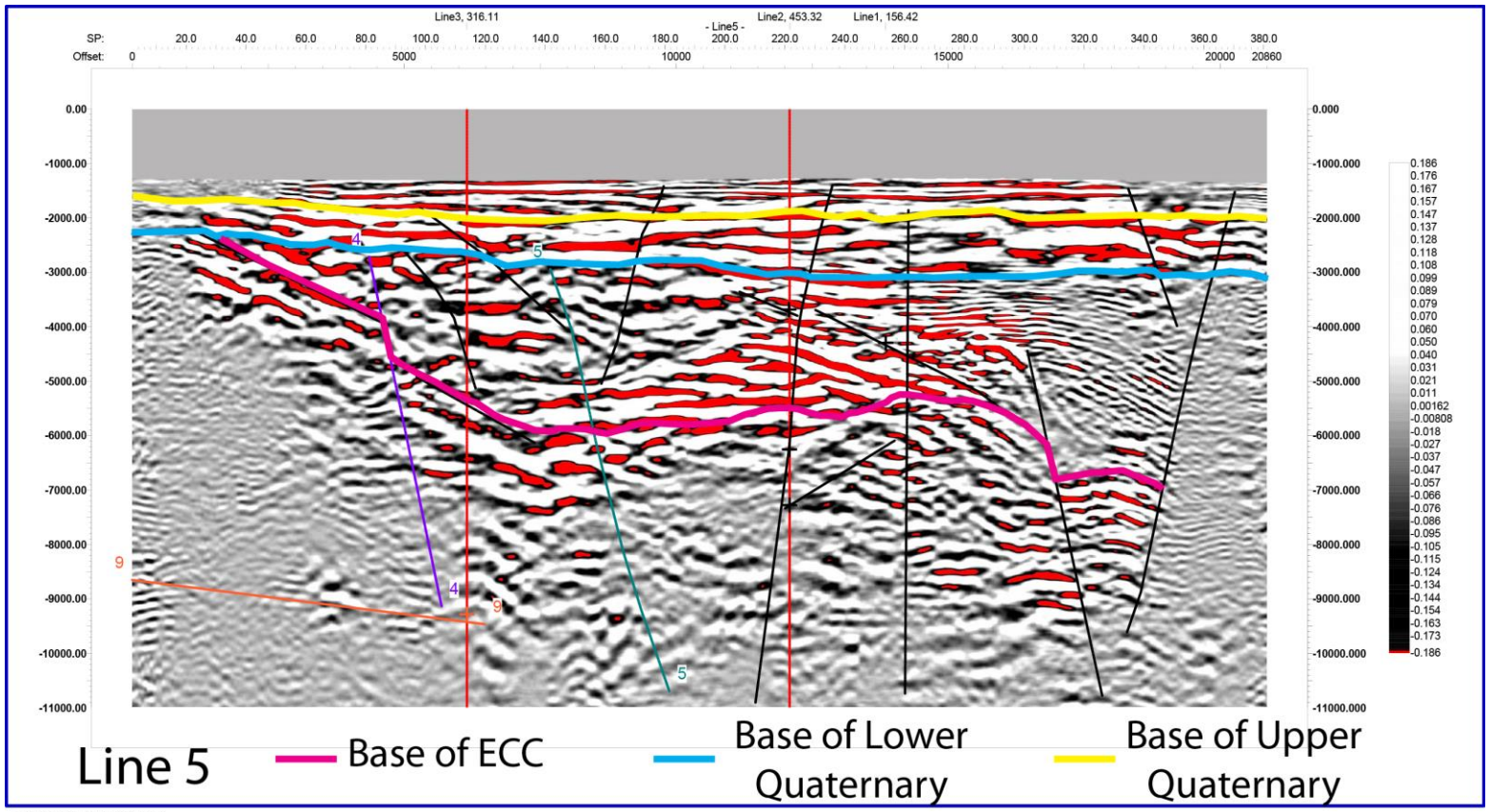

s482a651@LIN-GEO-03214
05/14/15 09:23:05

Plate 10: Seismic Line 5 With Velocity

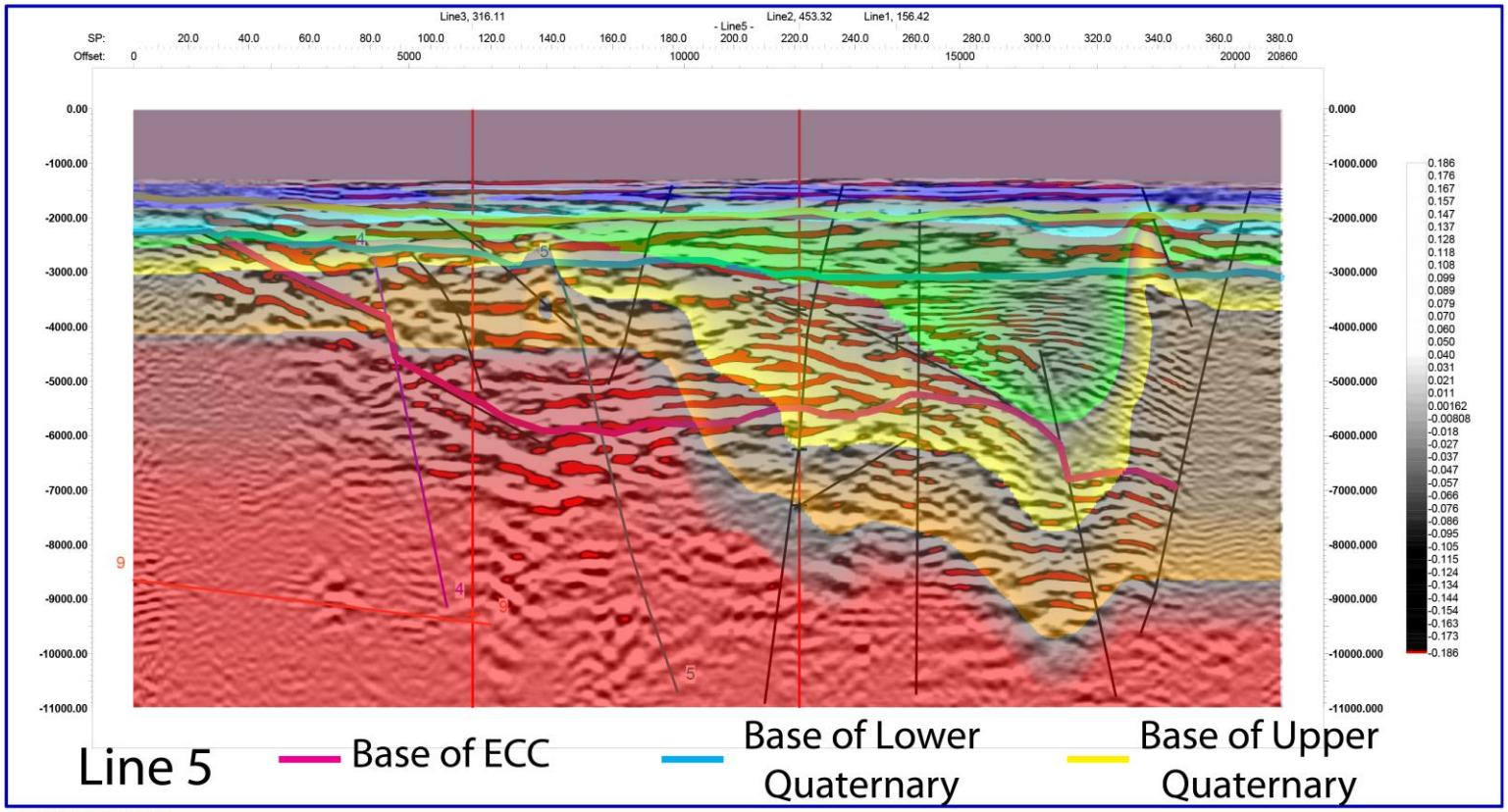

Plate 11: Full Geologic Interpretation of Seismic Lines 2 (TOP) and 4 (BOTTOM)

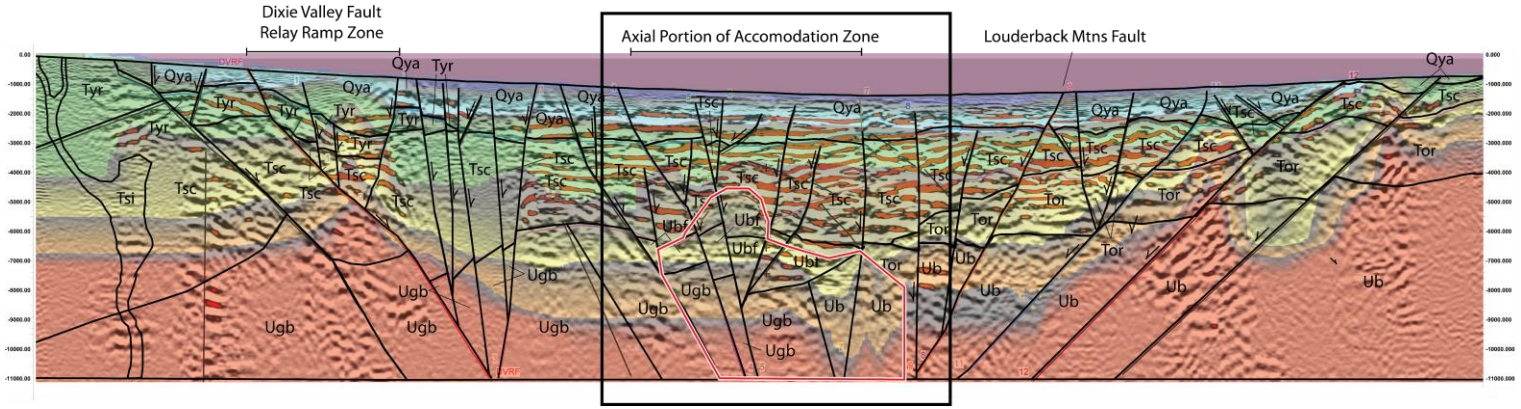

Figure 6.1 (RIGHT)

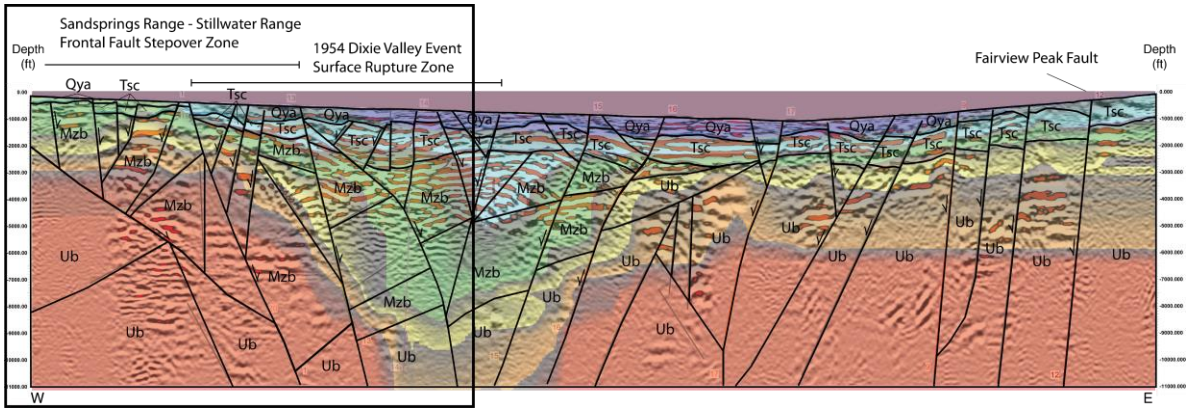

Figure 6.1 (LEFT)

10. APPENDIX C: GEOLOGIC MAP OF LA PLATA CANYON AREA CHURCHILL COUNTY, NEVADA

Plate 11: Geologic Map

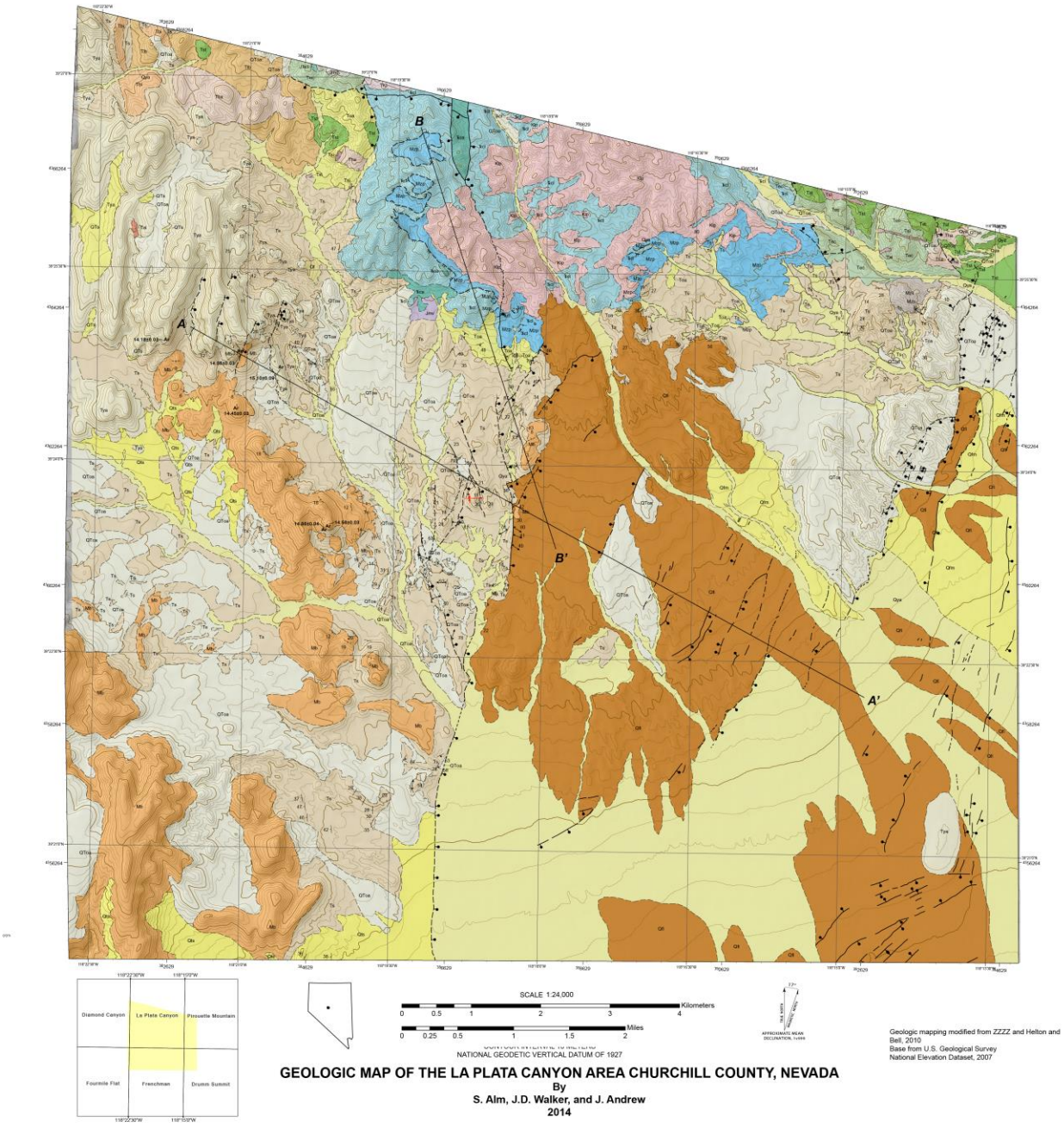

Plate 12: Description of Units

DESCRIPTION OF UNITS TAKEN FROM JOHN AND SILBERING, 1994 WITH SLIGHT MODIFICATION

Qya — Active alluvium (Quaternary) - Unconsolidated alluvium, talus, and other surficial deposits

Qfm — Alluvium (Late Pleistocene to Early Holocene) - Unconsolidated alluvium, talus, and other surficial deposits. Deposition is no longer active and is actively incised by modern erosion

Qfi — Alluvium (Mid- to late Pleistocene) - Unconsolidated alluvium, talus, and other surficial deposits

QToa — Older alluvium (Quaternary and (or) Tertiary - Unconsolidated to poorly consolidated alluvium that forms (locally) the highest terrace level. Includes locally derived Tertiary sediments of Ts

QTs — Sand (Quaternary and (or) Tertiary) - Unconsolidated, fine grain, well-sorted sand. Mostly eolian, dune forming in places. Likely derived from Lake Lahontan or Lake Dixie, but also may include sediment of Ts

Tb — Basalt (Miocene) - Basalt lava flows and flow breccias. Drak-gray to black, aphyric to sparsely porphyritic rocks containing fine-grained phenocrysts of plagioclase, clinopyroxene, and locally olivine. Locally vesicular.

Tbi — Basalt intrusions (Miocence) - Dikes, plugs, and dikes that fed the basalt lava flows (Tb). Intrudes Tertiary sedimentary rock and landslide breccia deposits (units Ts and Tb, respectively).

Tya — Younger andesite (Miocene) - Dark-gray to black, generally coarsely porphyritic hornblende or pyroxene-plagioclase andesite and dacite lava flows, flow breccia, and lahars. Locally includes shallow intrusive rocks

Tha — Hornblende andesite (Miocene) - Gray to reddish-brown, fine- to medium-grained porphyritic hornblende andesite lava flows. Contains about 10-15 percent medium-grained hornblende phenocrysts in dark-gray aphanitic groundmass.

Tai — Andesite intrusions (Miocene) - Small plug or neck of coarse-grained porphyritic, flow-banded plagioclase-clinopyroxene andesite intruding andesitic lahars near west edge of the map area. Also includes several small bodies of pyroxene andesite that intrude(?) the tuff of Elevenmile canyon and sedimentary rocs and tuff unit (Tst) in Elevenmile Canyon

Ts — Sedimentary Rocks (Miocene) - Generally well indurated, white, tan, and yellowish-brown, fine to coarse-grained fluvial and lacustrine sedimentary rock, which unconformably underlie the basalt, younger andesite, and hornblende andesite (units Tb, Tya, and Tha, respectively).

Tlb — Landslide breccis (Miocene) - Coarse deposits consisting of unsorted blocks of tuff and rhyolite set in coarse grained sandstone to pebble conglomerate matrix. Contains blocks of the tuff of Elevenmile Canyon and silicic intrusive rocks (units Tec and Tsi, repectively) as as 10 meters in

Tsi — Silicic intrusive rocks (Miocene and Oligocene?) - Numerous texturally and compositionally distinct silicic dikes and dome and minor pyroclastic aprons. Includes aphyric felsite, sparsely porphyritic biotite rhyolite and quartz rhyolite, coarsely porphyritic bitotite-quartz-plagioclase-K-feldspar

Tst — Sedimentary rocks and tuff (Miocene or Oligocene) - White to light-green, crystal-poor, pumice-rich, water-laid(?) rhyolite tuff and fine-grained tuffaceous sedimentary rocks. Tuff commonly contains distinctive clasts of dark-gray to black, silicified, very finely laminated, hot spring(?) deposits as much as 50 cm long.

Tec — Tuff of Elevenmile Canyon (Miocene or Oligocene) - Black, greenish-gray, and white, crystal-rich rhyolite to dacite ash-flow tuff. Contains 30-60 perscent phenocrysts of medium-grained plagioclase, lesser sanidine and quartz and 1-5 percent biotite. Generally densely welded. Commonly contains abundant drak-green, chloritizzed, crystal rich, flattened pumice clasts as long as 6 cm and abundant fragments of pre-Tertiary rocks and the older andesite unit (Toa). Horizons containing coarse blocks consisting of internally shattered marble and older andesite as large as 100m are common in Elevenmile Canyon. Generally strongly propylitized, argillized, or bleached.

Toa — Older andesite (Oligocene) - Mostly dark green to black, aphyric to medium grained, porphyritic andesite, dacite, and basalt(?) lava flows. Phenocrysts consist of tabular plagioclase, hornblende, and pyroxene. Generally altered to propylitic or argillic mineral assemblages. Cut by numerous quartz/calcite veins east of mountain well. Generally equivalent to the Pliocene(?) bsaslt unit of Page (1965, unit Tb)

Tkf — Felsite (Tertiary or Cretaceous) - Light colored felsite containing sparse, 1-2 mm phenocryts of resorbed quartz and altered feldspars in a fine-grained, allotriomorhic granular groundmass of quartz, plagioclase, K-feldspar(?), sericite, and ghosts of tabular mafic minerals outlined by ragged aggregates of epidote

Klp — La Plata Canyon Pluton (Cretaceous) - Composite, light-colored granitic intrusion consisting of fine- to medium-grained, equigranular biotite granite, quartz monzonite, and associated leucocratic dike rocks (Butler, 1979). Potassium-argon alteration age of 84 Ma from muscovite in vein within wall rocks at fluorite prospect near

Jmv — Andesitic metavolcanic rocks - Foliated dense greenstone, greenstone breccia exhibiting stretched clasts, and dacitic welded tuff and tuff breccia

Jmd — Dacitic volcanic-felsite flows and sedimentary breccia - White to dark gray, mostly weathered light brown. Massive felsite completely aphanitic and featureless in hand specimen; in thin section, composed entirely of more or less flow-alligned laths of altered plagioclase in altered, probably originally glassy, groundmass. Tectonically flattened, crudely bedded sedimentary breccia of felsite clasts interstratified in upper part of unit, and upper part of unit interfingers with unit Jms. Stratigraphic base of unit Jmd everywhere faulted

TRcl — Limestone (Upper Triassic) - Regularly thin-bedded to medium-bedded black lime mudstone. Lightly metamorphosed except where conspicuously flattened, foliated, and lineated near La Plata Fault and where thermally altered to marble near contact with La Plata Canyon pluton. Lime mudstone beds commonly have internal planar lamination and locally have laminae or quartz silt or subordinate interbeds of black argillite. Interpretted as slope, and possibly partly basinal, deposit. Conspicuous white alteration lenses, several millimeters thick ans as long as 20 cm, and composed of neomorphosed calcite, are locally abundant within lime mudstone beds. Similar in lithic character, age, and depositional setting to, and is regarded as a lateral equivalent of the hoyt Canyon Formation of Speed (1978), which forms part of the Clan Alpine sequence of the Clan Alpine Mountains

TRca — Argillite (Upper Triassic) - Predominantly planar laminated argillite with subordinate quartzose siltstone and fine-grained sandstone as laminae or thin, locally graded beds. Light brown, olive gray, or gray where horndfelsed near La Plata Canyon pluton. Weakly developed slaty foliation away from areas of thermal metamorphism. Minor intercalations of limestone. Interpreted as laterally equivalent to the slope or basinal siliciclastic rocks that are either interstratified with limesotne strata of the Hoyt Canyon Formation of Speed (1978) in the typical Clan Alpine sequence of the Clan Alpine Mountains.

Mzp — Phyllite (lower Mesozoic?) - Strongly foliated phyllite, commonly spotted by intrafohliation porphyroblasts of andaluit which locally are aligned, forming a pro-

SYMBOLOGY

Contacts - Solid where location is accurate; long-dashed where location is approximate; short-dashed where location is inferred; dotted where location is concealed. Queries added where identity or existence may be questionable

Fault - Solid where location is accurate; long-dashed where location is approximate; short-dashed where location is inferred; dotted where location is concealed. Queries added where identity or existence may be questionable

Normal Fault - Ball and bar on apparent downthrown side

Detachment Fault - Hachures on upper plate

Folds - Solid where location is accurate; long-dashed where location is approximate; short-dashed where location is inferred; dotted where location is concealed. Queries added where identity or existence may be questionable

Anticline - Large arrowhead indicates plunge direction

Syncline - Large arrowhead indicates plunge direction

Inclined bedding - Showing strike and dip

Fault plane - Showing strike and dip

Fault plane w/lineation - Showing strike, dip, and trend of slickenline

Foliation - Showing strike and dip

Inclined contact - Showing estimated strike and dip, measured on aerial imagery

Ar — **Sample** - $^{40}Ar/^{39}Ar$ age Ma (millions of years ago) with uncertainty; see table x

Plate 13: Correlation of Map Units

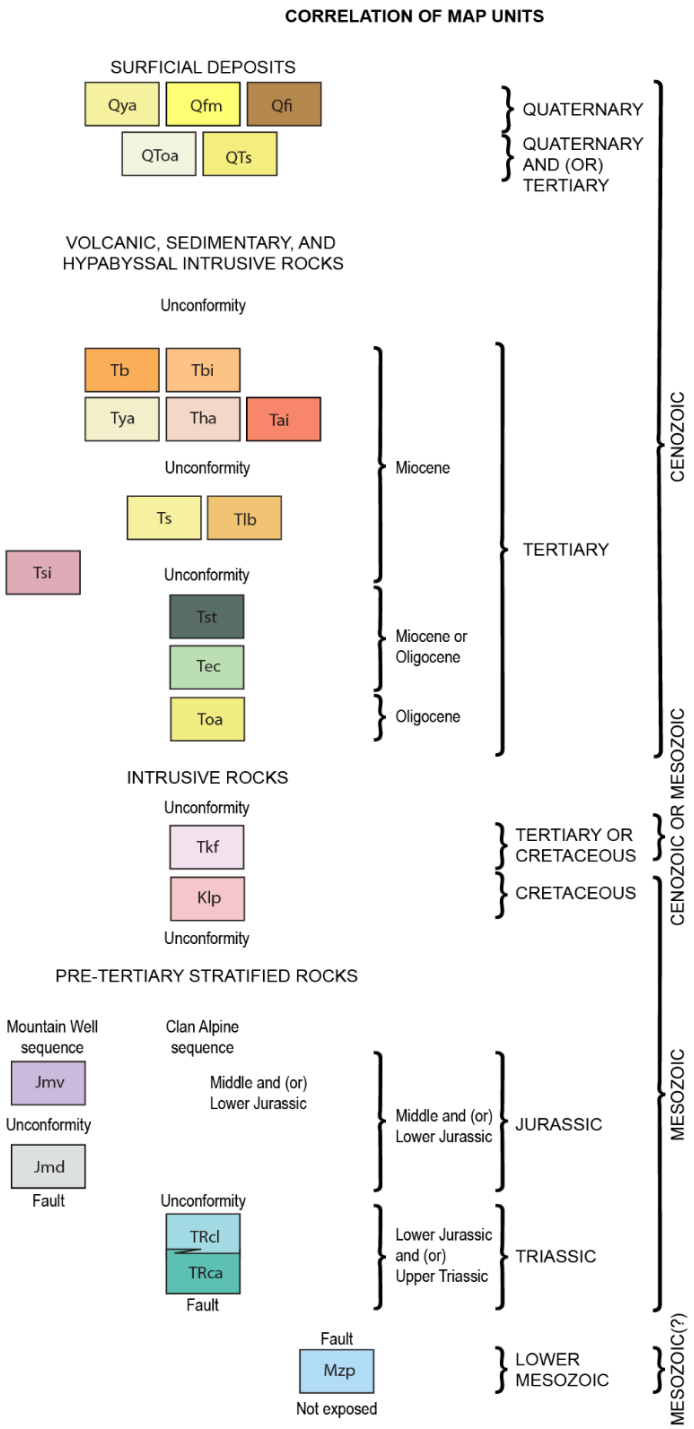

Plate 14: Cross Section B-B’ and A-A’

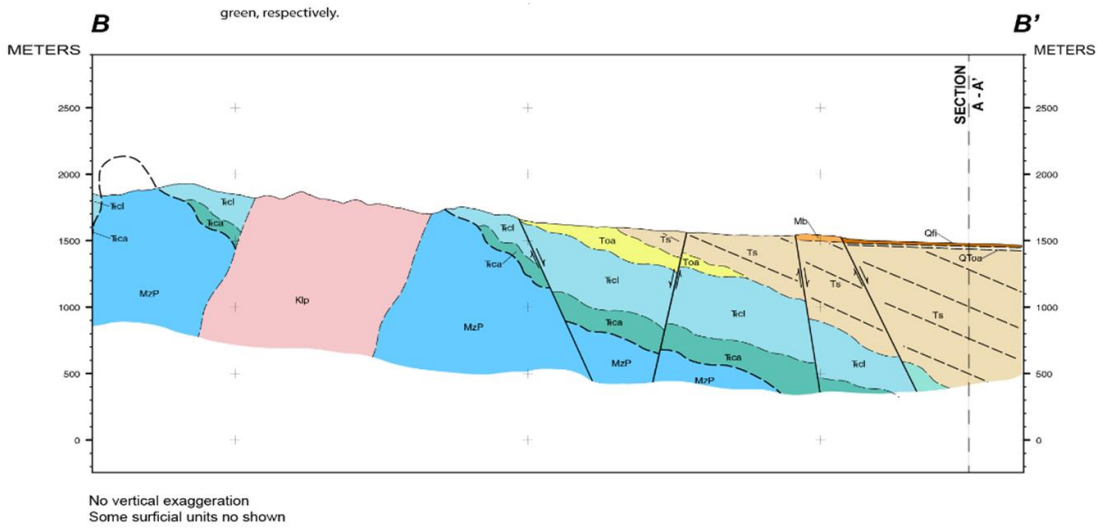

No vertical exaggeration
Some surficial units no shown

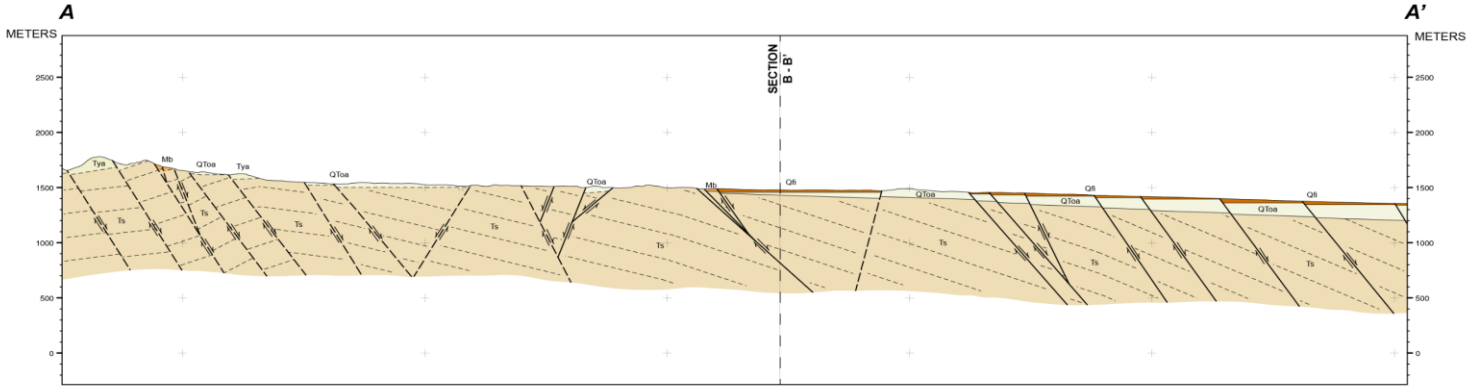

No vertical exaggeration
Some surficial units no shown

Plate 15: LANDSAT 8 Image of Dixie Valley

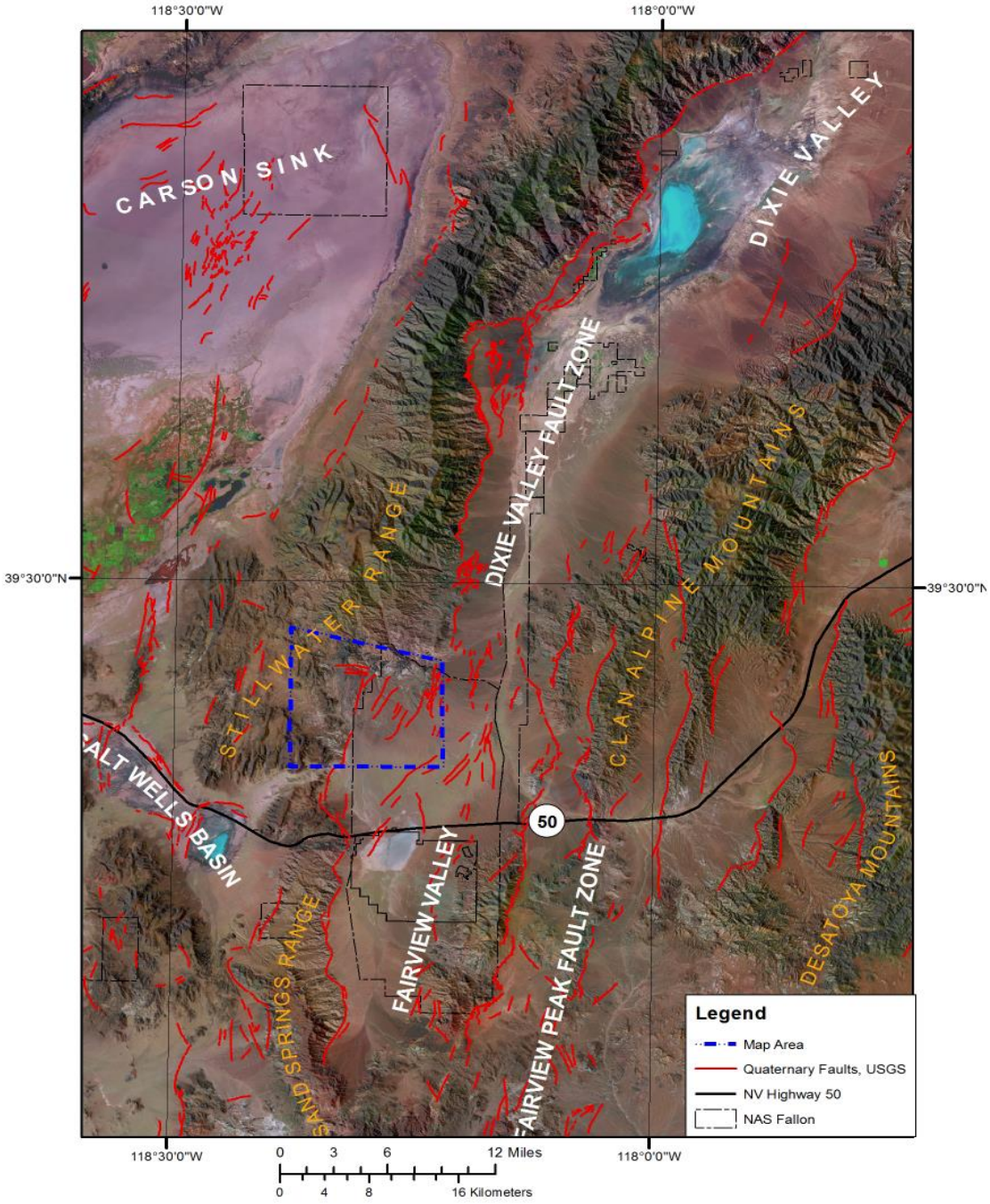

Figure 1. Lansat 8 image of Dixie Valley area. Nevada, showing location of map area, major physiographic features, and structures. This image is a false-color composite image that combines bands 7 (SWIR 2 2.11-2.29), 5 (NIR 0.85-0.88), and 3 (green 0.53-0.59) and displays them as red, blue, green, respectively.